Light matter interaction in chaotic resonators

Thesis by

Changxu Liu

In Partial Fulfillment of the Requirements

For the Degree of

Doctor of Philosophy

King Abdullah University of Science and Technology, Thuwal,

Kingdom of Saudi Arabia

The thesis of Changxu Liu is approved by the examination committee

Committee Chairperson: Andrea Fratalocchi

Committee Member: Boon S Ooi

Committee Member: Yu Han

Committee Member: Marco Peccianti

ABSTRACT

Light matter interaction in chaotic resonators

Changxu Liu

Chaos is a complex dynamics with exponential sensitivity to the initial conditions. Since the study of three-body problem by Henri Poincare, chaos has been extensively studied in many systems, ranging from electronics to fluids, brains and more recently photonics. Chaos is a ubiquitous phenomenon in Nature, from the gigantic oceanic waves to the disordered scales of white beetles at nanoscale. The presence of chaos is often unwanted in applications, as it introduces unpredictability, which makes it difficult to predict or explain experimental results. Inspired by how chaos permeates the natural world, this thesis investigates on how the interaction between light and chaotic structure can enhance the performance of photonics devices. With a proper design of the lighter-mater interaction in chaotic resonators, I illustrate how chaos can be used to enhance the ability of an optical cavity to store electromagnetic energy, realize a blackbody system composed of gold nanoparticles, localize light beyond the diffraction limit and control the phase transition of superradiance.

ACKNOWLEDGEMENTS

First and for the most, I would like to express my special gratitude to my advisor, Prof. Andrea Fratalocchi for his supervision during the past four years. It is a great honor for me to be his first PhD student. I really enjoyed the period working with him, with his support both academically and emotionally. Together we finished several very interesting projects and published them on peer-reviewed journals. There is no doubt that without Andrea, I would not have such a productive PhD career. What is more, Andrea sets an excellent example of how to be a successful scientist, and the working experience here will certainly provide benefits to my career development.

My genuine thanks also goes to all our collaborators both inside and outside KAUST, including Prof. Boon S. Ooi, Prof Yu Han, Prof Andrea Di Falco, Prof Thomas F. Krauss, Prof. Kubos Kuipers and the people in their groups, who provide the indispensable contributions to my projects described in this thesis..

Also, I want give my gratitude to Prof. Boon S. Ooi, Prof Yu Han and Prof. Marco Peccianti for severing as the committee members.

Besides, I want thanks all the colleagues in our group, for the their kind support and useful discussions. We really had a great time work together.

Last but not least, I want to show my great thanks to my family, including my grandparents, my parents and my wife. Thanks so much for the understanding and unconditional support all through my way.

TABLE OF CONTENTS

LIST OF ABBREVIATIONS

4-MP	4-mercaptophenol
BEC	Bose-Einstein Condensation
FDTD	Finite-Difference Time-Domain
FFT	Fast Fourier Fransform
FWHM	Full Width at Half Maximum
HRTEM	High Resolution Transmission Electron Microscopy
NSOM	Near-Field Scanning optical Microscope
PDS	Power Density Spectrum
PhC	Photonic Crystal
RMT	Random Matrix Theory
RWs	Rogue Waves
SEM	Scanning Electron Microscope
SOI	Silicon On Insulator
SPP	Surface Plasmon Polariton
SWH	Significant Wave Height
TDCMT	Time-Dependent Coupled Mode Theory
TEM	Transmission Electron Microscopy

LIST OF FIGURES

LIST OF TABLES

Chapter 1

INTRODUCTION AND SUMMARY OF EXPERIMENTAL AND THEORETICAL RESULTS

1.1 Evolutionary photonics inspired by nature

Through millions of years of evolution, Nature has made unparalleled optimizations onto the animals and plants. In spite of limited range of component materials in the ambient environmental, the Nature Selection developed amazing strategies to optimize the structure of the creating, providing a cornucopia to inspire scientists and engineers to development new technologies [1, 2, 3, 4].

Figure.1.1 illustrates several typical examples how the Nature selection helps the animals to develop elegant architectures for the optimization of optical properties. Cataglyphis bombycina, a silver ant living in Sahara can survive in the scorching environment with the help of dense arrays of triangular hairs (shown in Fig. 1.1a to c) [5]. Such structures not only generate the silver color, but also enhance both the

solar reflection in visible and near-infrared and infrared thermal radiation to the environment, leading to the development of passive radiative cooling of objects [6]. Callophrys gryneus, a butterfly native to North America is demonstrated with brilliant colorful wings [7] (Fig. 1.1 d to f,). Through nature selection, the butterfly developed the microstructures with ordered periodicity. Such structures form a photonics crystal that perfectly reflects the light within a certain bandgap and generates the vivid color that can protect them away from the predators.

Figure 1.1 g demonstrates scarlet macaw, a larger colorful South American parrot. The sponge in the blue feather barbs forms a amorphous photonic structures with short-range order and long-range disorder (Fig. 1.1i), an natural optimization to maximize diffuse coloration[8].

The last example is the Cyphochilus, a white beetle in southeast Asia. The insect developed the ultra-brilliant color through evolution, providing a perfect camouflage in the fungi where it lives (see Fig. 1.1 j and k). Quite interestingly, the brilliant white color of the insect is not due to the white pigment, but due to the diffusion and broadband reflection of light from the disordered thin scales. The thin scales with only 5μm form a dense scattering media resulted from the structural chaos, generating ultra-white color [9].

Following the examples mentioned above (especially the last one with disordered structure), we may propose a question, can we harness the chaos with the assistance of the inspiration from Nature? The presence of chaos is often unwanted, as it introduces unpredictability, which makes it difficult to predict or explain experimental results. On the other hand, chaos is a ubiquitous phenomenon in Nature, such as the macroscopic oceanic hydrodynamics and the disordered scales of white beetles with micrometer size. With proper design, we may take advantages of the chaos that can ameliorate the performance of photonics devices. Specifically Considering the light-matter interaction in a resonator, chaos can be used to enhance

the capability of an optical cavity to store energy (Chapter2), realize a blackbody at nanoscale (Chapter3), localize light beyond the diffraction limit (Chapter4) and control the phase transition of superradiance (Chapter5).

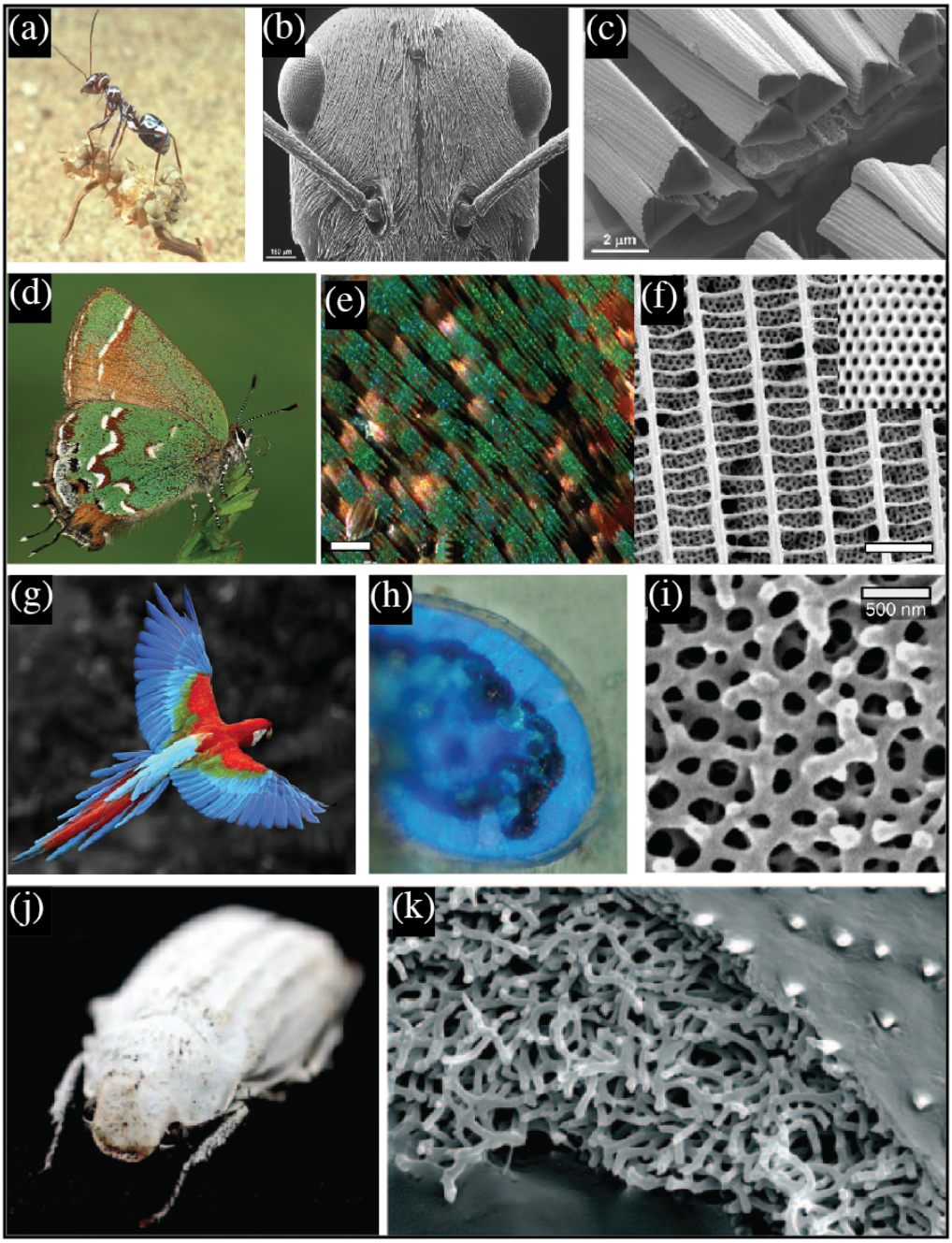

Figure 1.1: (a) Cataglyphis bombycina, a silver ant living in Sahara, Africa. (b)SEM images of the head of the ant covered by the triangular hairs. (c) The cross-section of the hairs of by focused ion beam. [5]. (d) Callophrys gryneus, a butterfly native to North America. (e) the ventral wing cover scales of the butterfly. (f) SEM image of the dorsal surface of the scale with periodic structures. [7] (g) Scarlet macaw, a larger colorful South America parrot. (h) Image of cross-section of a blue barb (i) cross-sectional SEM picture of the spongy keratin structure. [8] (j) A picture of Cyphochilus, a white beetle in south-east Asia. (k) SEM picture of internal scale of the beetle. [9]

1.2 Broadband light harvesting based on chaotic resonator

Harvesting broadband light efficiently into an optical resonator is of substantial interest for many practical applications, ranging from photovoltaics to nonlinear optics [10, 11]. Always there is a trade-off between the bandwidth and the coupling efficiency. For a monochromatic light, the energy can be effectively coupled into the cavity with the resonance matching the wavelength. But the coupling efficiency drops drastically as the wavelength goes outside the resonance.

The maximum power that can be transferred depends on the coupling coefficient and loss (lifetime) of each given mode [12]. The maximum efficiency reaches 50% when the coupling strength is equal to the loss. However, the lifetimes of the modes supported by resonators with classical geometries vary across the spectrum, making the effective energy transfer at few modes inside the band and thus limit the average coupling efficiency for a broadband applications.

Inspired by the nonclassical shape of chloroplasts in the photosynthesis, we overcome this intrinsic limitation by exploiting specific shape deformations to the resonators. The chaos introduced to the geometry randomizes the trajectories for light rays, manipulating all lifetimes of the modes towards a single value. The convergence makes the energy available in the spectrum equally distributed to each degree of freedom (the mode in the cavity), which is similar to the well-known Brownian motion. Such energy equipartition dramatically enhance the energy storage capability for a broad band light source.

Our analytical, numerical and experimental results validate the increment of the energy trapped inside the cavity, 600% in 2D FDTD simulation and 12% in 3D experiment separately. With the assist of chaos, the energy trapped in the cavity is considerable enhanced without introducing extra material, opening a cost-effective

avenue for the broadband energy harvesting.

1.3 Bio-inspired Structural darkness created from disordered gold nanostructures

Blackbody is a theoretical material that absorbs radiation at all angles, wavelengths and polarizations without any transmission and reflection. Blackbody emits as much energy as, or more energy than, any other body at the same temperature according to the second law of thermodynamics, behaving like a perfect absorber and emitter. As an ideal source for energy absorption and emission, black material is of paramount importance in a variety of fields ranging from solar energy harvesting to thermal light emitting sources and sensors. Significant efforts have been devoted towards the ideal material, and vertically-aligned single-walled carbon nanotube array is of one candidate to achieve the high broadband absorption [13]. However, such structures suffer from a comparatively large thickness (hundreds of microns) and lose of flexibility in practical applications.

Inspired by the specific kind of beetles, Cyphochilus, we developed the blackbody system from gold nanoparticles. The brilliant white color of these beetles is not due to a white pigment, but stems from a disordered network of thin scales that scatter incident light at all wavelengths. After reversing the effect and applying a conformal optical mapping, a blackbody system can be realized from a random distribution of gold nanoparticles. The material has extremely high broadband absorption (>98%) between 400-1200nm, with a tiny filling factor ($1.5 \cdot 10^{-5}$) . The thin film made from such nanoparticles shows a high absorption (98% averaged over the spectrum with 10 μm thick) nearly independent of incident angle.

Based on the nano-absorber, we are managed to generate mono-color emission through light condensation process without the need of any resonance. The light condensation process can select all the available spectral energy and build up it to the band edge with exponential efficiency.

1.4 Subwavelength rogue waves generated through chaos on a photonic chip

Rogue waves, also known as freak waves, are extreme events characterized by the appearance of localized waveform with exceptional high amplitude. The historical record of rogue waves is dated back to 1861, where an oceanic wave with 40 meters has been observed near Eagle Island, Mayo, Ireland. More recently, the existence of rogue waves was confirmed by the radar images from two European Space Agency satellites, showing ten giant waves with height over 25m. Since then, freak waves have been extensively studied in various scientific fields, ranging from oceanography to acoustics, capillary waves, microwaves, and beyond [14]. In Optics, rogue waves have been reported in microstructure optical fibers, lasers operating in both mode locking and continuous regime, and oscillators realized in liquid crystals media [15]. There is a tremendous amount of energy embedded inside the rogue waves, providing a possibility to the extreme localization of waves. However, the probabilistic fashion makes them difficult to predict and hard to generate on demand. Using chaotic optical resonators with engineered losses, we can trigger the onset of rare events akin to rogue waves controllably. Gigantic optical pulses are formed in both space and time inside the cavity, coherently building up all the energy available in the spectrum. Through near-field imaging experiments, we record confined rogue waves characterized by a spatial localization of 206 nm and with an ultrashort duration of 163 fs at a wavelength of 1.55 μm. Without using any complexed metallic nanostructures or sophisticated wavefront shaping techniques, chaos helps the formation of the subwavelength localization in a homogenous media, opening a new path for the nano-fusing in linear regime.

1.5 Observation of superradiant phase transition in quantum chaos

Superradiance is process of enhanced spontaneous radiation resulting from the coherent cooperation between atoms through a common radiation field. An atomic system is composed of N two-level atoms, with only one at the excited state. When the atoms are closely located, the decay rate of the system is enhanced by N times compared to the intrinsic decay rate of a single atom. Such effect was firstly predicted by Robert Dicke in 1954 [16, 17] and experimentally observed in 1973 [18]. Since then, such phenomena has been reported extensively in different systems, both in classical an quantum regime [19].

Despite a large body of theoretical results, however, many questions about superradiance are still debated; this lack of experimental evidence originates, in part, from the difficulties in replicating the original setup investigated by Dicke. We introduce an engineered chaotic optical cavity with controllable losses that mimics the dynamics of a quantum system, and we conduct a detailed study of superradiant states. We modulate the cavity losses and investigate both how superradiance is dynamically approached and the universal hallmarks of this effect.

Our experimental setup takes advantage of the technology of two-dimensional photonics crystals, which makes it possible to fabricate micro-sized, transparent cavities with no absorption losses and completely controllable properties. When light enters a chaotic resonator, it bounces against the resonator walls in a random fashion and excites cavity resonances. When the cavity losses are sufficiently small, the cavity resonances do not interact. Above a specific loss threshold, however, resonances cooperate and superradiant states are formed, with the system entering into a new self-organized phase. We use experimental results, analytical predictions, and numerical modeling to demonstrate that multiple superradiant states are gener-

ated. We employ random-matrix theory to determine the nonlinear dynamics of the Dicke transition.

Chapter 2

ENHANCED ENERGY STORAGE IN CHAOTIC OPTICAL RESONATORS

2.1 Energy storage inside a cavity

The enhanced interaction between light and matter in optical cavity resonators is an interdisciplinary subject of a great interest as it affects many areas of condensed matter physics, including cavity electrodynamics [20], quantum and nonlinear optics, but also more applied aspects such as optical signal processing [21, 22, 23] and resonantly enhanced optical absorption [24]. All these applications are enabled by highly optimized optical resonators that can efficiently trap electromagnetic energy in narrow frequency bands. In conventional cavities, there is a simple tradeoff between bandwidth and the enhancement of trapped energy: the higher the enhancement, the narrower the bandwidth. A great challenge in the field is therefore to develop a new generation of cavities that are able to break this fixed relationship and store more energy in a given bandwidth window than conventional cavities would allow. These are expected to provide new breakthroughs in the field, thus accessing

a novel series of applications ranging from sensing to lasers, energy harvesting and cavity quantum electrodynamics.

The maximum power that can be transferred into a conventional resonator depends on the coupling coefficient and loss of each given mode, and tends to vary across the mode spectrum, especially when broadband operation ($\Delta\lambda$ on the scale of hundreds of nanometres) is considered. In addition, classical two- and three-dimensional geometries tend to accommodate modes with very different lifetimes in the same spectral region, a good example being the widely used photonic crystal L3 type cavity that features modes of very different Q-factor closely spaced in frequency [25]. Therefore, the use of classical resonators for broadband energy storage is limited. Here, we overcome this intrinsic limitation by exploiting specific shape deformations that support chaotic trajectories for light rays. Surprisingly, we note that in a chaotic cavity regardless of any regime of coupling the lifetimes of all modes tend towards a common value, thus significantly improving the transfer of energy into the cavity and increasing the energy-storage capability of the cavity. Such chaotic resonators [26] have been well exploited in the field of laser devices [27, 28, 29, 30, 31, 32, 33, 34]. We also note that the mode spectrum of deformed microsphere resonators has been studied recently, with remarkable changes in Q-factors being observed [35]. However, despite this large body of literature, nothing is known about the capacity of such resonators to store and collect light energy over a broad spectral range.

The increased energy storage capacity of a chaotic resonator when compared to a classical one can be explained intuitively by adopting a ray optics approach and considering that a suitable shape deformation is accompanied by the breaking of symmetry in the structure. As a consequence, the deformed resonator cannot support any cyclic motion of light, so the trajectory of light rays changes from regular to random, statistically resulting in a larger lifetime of the photons in the cavity

[26]. To clarify this result, we start our analysis from a symmetric (classical) resonator and observe its capacity to trap energy as it is deformed. We define a deformation parameter α, which we will use in the following description as a handle to deform any given geometry, where $\alpha = 0$ indicates the original, undeformed structure and $\alpha > 0$ indicates a proportionally deformed geometry. For example, a circle would be described by $\alpha = 0$, and a deformed circle by $\alpha > 0$, with a describing the degree of deformation. And the value of α depends on a specific geometry. This parameter is generic and can be used to describe the deformation of any type of resonator, for example, square or disk in two dimensions or cube or sphere in three dimensions. In general, the larger a is, the larger the degree of chaos, until a saturation value is reached.

2.2 A single ab initio experiment

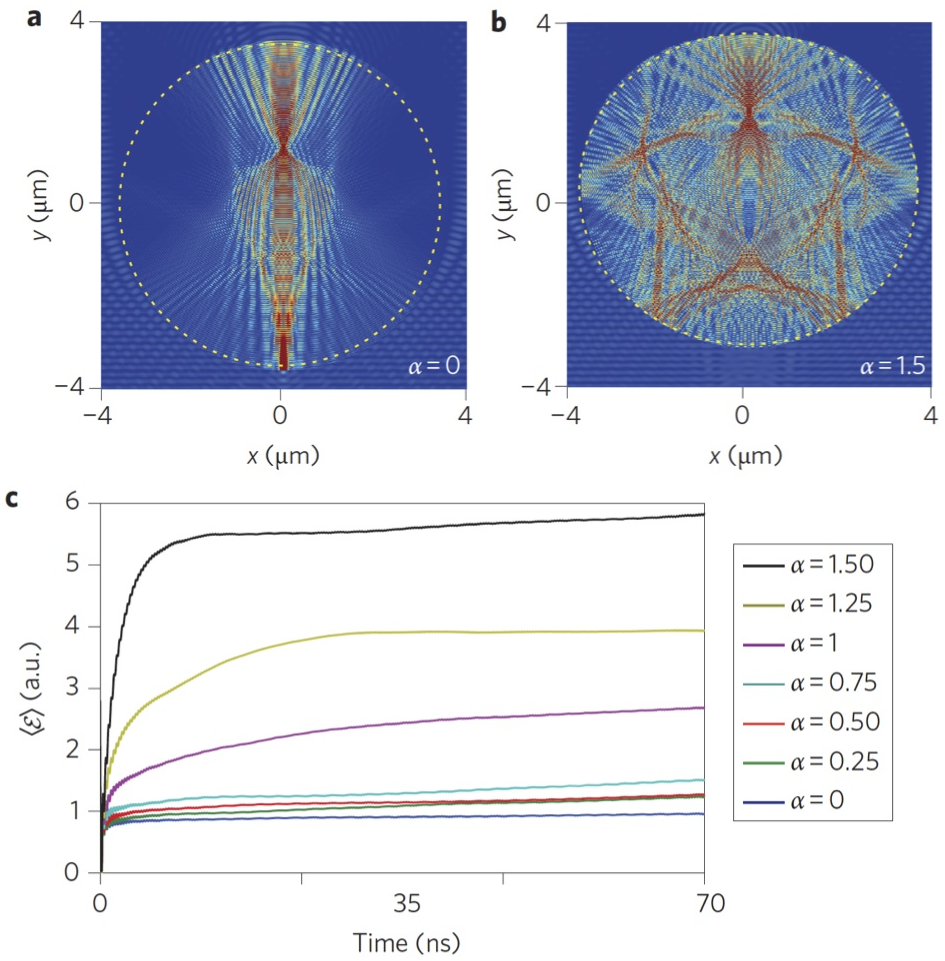

Figure 2.1: Ab initio results of chaotic energy storage with a super-continuum light source from 300 to 1000 nm. (a) Snapshot of the electromagnetic energy density $\mathcal{H}$ distribution after $t = 45$fs in a resonator (dashed line) with A=30 μm^2 for $\alpha = 0$ (a) and $\alpha = 1.5$ (b). (c) Time evolution of the average electromagnetic energy $\langle \mathcal{E} \rangle$ for different α.

The theory is more easily developed in two dimensions, starting from a circular resonator. Our set-up consists of a silicon dielectric resonator with air holes, the shape of which is defined by the following function in polar coordinates (ρ_c, θ_c):

$$\rho_c = \sqrt{\frac{A}{\pi} - \frac{\alpha^2}{2}} + \alpha \cos\theta_c, \quad 0 \leq \theta \leq 2\pi \tag{2.1}$$

where A is the resonator area and $\alpha \geq 0$ is the single parameter that controls the resonator shape. Equation 2.1 belongs to the family of analytic curves investigated by Robnik: for $\alpha > 0$, equation 2.1 supports chaos in the trajectory of light rays, which randomly bounce inside the resonator [36]. From a physical perspective, the shape defined by equation 2.1 is equivalent to an asymmetric deformation of a disk, and can be realized experimentally with conventional nanofabrication tools.

In our simulations, we fixed the resonator area to $A = 30\mu m^2$ and numerically calculated the electromagnetic energy E stored inside the resonator for varying values of α. Although the value of α in equation 2.1 is not bound to an upper value, we note that the system reaches saturation for a maximum degree of chaos described by $\alpha = 1.5$ (see Section 2.7 for more details). We therefore restrict our numerical analysis to $\alpha \in [0\ 1.5]$. The calculation of the electromagnetic $E(t) = \int_D H d\mathbf{r}$ is performed by a numerical integration of the energy density $\mathcal{H}(\rho; t) = \frac{1}{2}(\mathbf{E}\cdot\mathbf{D}+\mathbf{E}\cdot\mathbf{D})$ in the volume D encompassed by the resonator and defined by $\rho \leq \rho_c$ and $0 \leq \theta \leq 2\pi$. We simulated the input from a supercontinuum source centered at $z = 0$ and propagating along z for wavelengths between $\lambda = 300$ nm and $\lambda = 1300$ nm, which simulates a broadband source such as sunlight. Figure 2.1 a,b shows a time snapshot of the spatial distribution of $\mathcal{H}$ after $t = 45$ fs, and illustrates how the geometry of the resonator changes with a (Fig. 2.1 a,b, dashed line). As seen, even a small deformation in shape (at a constant volume) yields a radically different behavior in the distribution of light energy inside the resonator. Figure 2.1c, conversely, displays the time-averaged energy $\langle\mathcal{E}\rangle = \frac{1}{t}\int_0^t E(t')dt'$ evolution with increasing parameter α. Remarkably, the introduction of chaos into the motion of light is accompanied by a dramatic change in the energy stored inside the resonator; indeed, the steady-state regime (when the insertion of energy balances radiation losses) shows an approximately sixfold increase even for $\alpha = 1.5$ (Fig. 2.1b). This energy accumulation grows with the deformation, and rises monotonically as α in-

creases from 0 to 1.5.

We use time-dependent coupled mode theory (TDCMT) [12] to develop a simple and reliable model for the lightresonator interaction. The system can be modelled as a side-coupled resonator, the dynamical equations of which can be easily solved to obtain energy $\mathcal{E}_k$ and power $\mathcal{P}_k$ stored in the the kth mode (Section 2.6):

$$\mathcal{E}_k = \frac{{\tau_k}^2}{\tau_e}(1 - e^{\frac{t}{\tau_k}})^2, \mathcal{P}_k = \frac{2\frac{\tau_e}{\tau_{k0}}}{(1 + \frac{\tau_e}{\tau_k 0})^2}|S|^2 \tag{2.2}$$

where $|S|$ is the input source power and $1/\tau_k = 1/\tau_{k0} + 1/\tau_e$ is the mode decay rate (τ_{k0} is the intrinsic cavity decay rate of the kth mode and $1/\tau_e$ is the escape rate due to coupling with the environment). The power $\mathcal{P}_k$ strongly depends on the ratio between the radiation and the coupling loss through the parameter τ_{k0}/τ_e, achieving the maximum value of $\mathcal{P}_k = 0.5|S|^2$ when $\tau_e = \tau_{k0}$. Outside this matching condition, the power coupled into the structure decreases very quickly. To study how the dynamics of the decay rates can be affected by chaos, we began by calculating the evolution of the decay rates τ_{k0} for different a in the resonator defined by equation 2.1. In a series of finite-difference time domain (FDTD) simulations, we first excited the resonator with a source and then monitored the energy evolution $\mathcal{E}(t)$ when the source was switched off. The decay constants τ_{k0} are extracted from the time energy evolution $\mathcal{E}(t) = \sum_k |A_k|^2 e^{-2t/\tau_{k0}}$ by applying the Prony method [37].

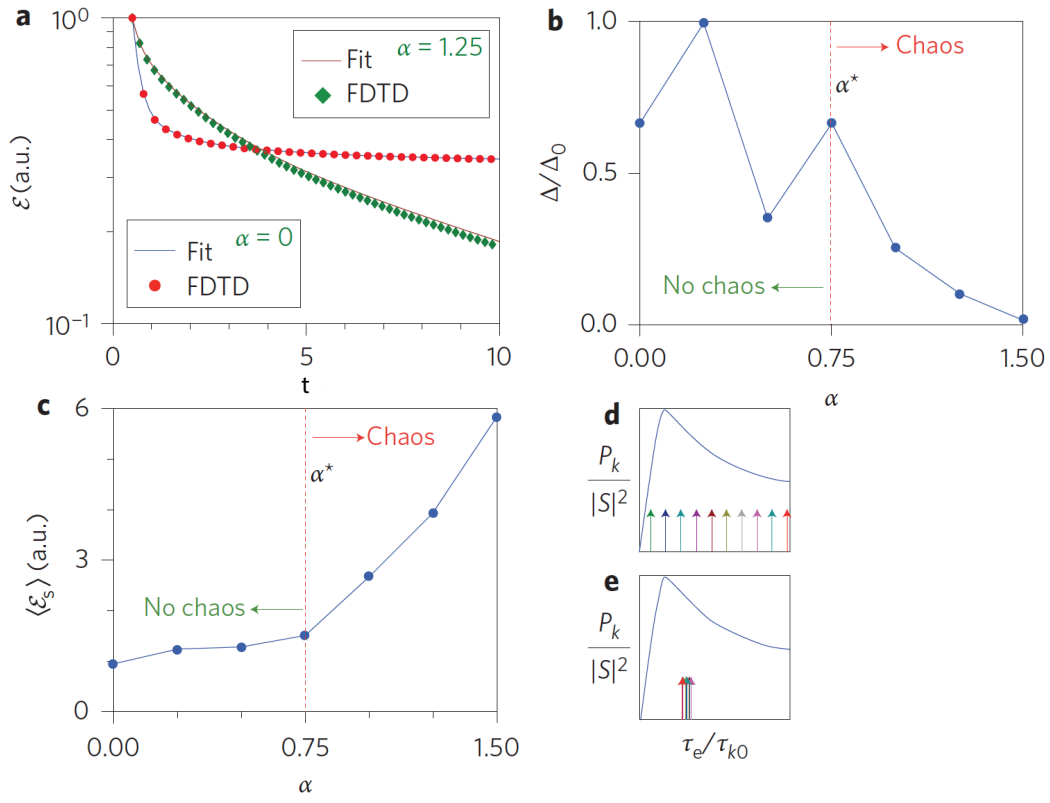

Figure 2.2: Chaos-induced modal collapse. (a) Log-plot of the energy E relaxation dynamics for $\alpha = 0$ and $\alpha = 1.25$, showing FDTD results (symbols) and Prony exponential fits (solid lines). (b) Normalized distribution of the difference between the maximum and minimum decay constants $\Delta(\alpha)/\Delta(0) = \Delta/\Delta_0$ versus α. (c) Steady-state energy distribution $\langle \mathcal{E}_s \rangle = \langle \mathcal{E} \rangle$ ($t = 45$ fs) for varying values of α. (d) to (e) Effects of convergence of the decay constants τ_k on the power $\mathcal{P}_k$ transferred into the structure. This behavior is plotted versus τ_e/τ_{k0} as a solid line. In the non-chaotic situation (d) the distribution of τ_e/τ_{k0} (coloured arrows) is broad and only a few frequencies efficiently transfer power. In the strongly chaotic case (e), conversely, a condensed distribution of τ_e/τ_{k0} yields the same contribution for all wavelengths and a much larger number of frequencies contribute to store energy.

Figure 2.2a shows two typical examples of numerical simulations (markers) and a fit (continuous line) for two different values of a. In general, modes of different frequency exhibit different decay rates $1/\tau_{k0}$. However, when strong chaos is generated in the structure, the distribution of τ_{k0} converges towards a frequency-independent delta function. In fact, calculations that start from initial conditions already belonging to the chaotic region of phase space will always be distributed according

to the same probability distribution, which defines the so-called natural invariant measures of the system20. As a result, when the entire phase space is dominated by chaos, we observe the same evolution of the decay rates, for all possible initial conditions, towards a frequency-independent decay rate $\tau_{k0} = \tau_0$. A convenient way of highlighting this dynamics is to plot the difference between the maximum and the minimum decay constant, $\Delta(\alpha) = max(\tau_{k0}) - min(\tau_{k0})$, for different values of a (Fig. 2.2b). We clearly observe a transition scenario. Below the chaos threshold, $\alpha \leq \alpha^*$, the dynamics simply shows an oscillation of $\Delta(\alpha)$ around the same average value, while above it ($\alpha \geq \alpha^*$), a clear convergence of $\Delta \to 0$ is observed. The value α^* depends on the specific geometry of the chaotic resonator, and can be assessed by calculating the relative area of the system phase space that encompasses chaos (Section 2.7). The effect of this convergence towards a single lifetime of all the modes on the energy collected by the resonator can be readily evaluated from equation 2.2 . The total power transferred into the structure, in particular, then becomes frequency-independent ($\mathcal{P}_k = \mathcal{P}_0 = 2|S|^2 \frac{\tau_e}{\tau_{k0}}(1 + \frac{\tau_e}{\tau_{k0}})^{-2}$), and every mode contributes to the same extent to storing energy inside the resonator. When many modes are present in the resonator, their large number results in a coherent buildup process that leads to a significant accumulation of energy (Figs 2.1b, 2.2c). In the non-chaotic case, conversely, much fewer modes are able to efficiently transfer energy into the resonator due to the mismatch between τ_{k0} and τ_e (Figs 2.1b, 2.2d). The chaos-assisted energy buildup process observed when ($\alpha \geq \alpha^*$ originates from the fundamental thermodynamic principle of equipartition, which can be highlighted using equation 2.2. By substituting$\tau_{k0} = \tau_0$ into the left-hand side of equation 2.2, and assuming a dense distribution of modes, with wavelength separation $\lambda_{k+1} - \lambda_k = d\lambda = \lambda$, we obtain

$$\frac{\partial \mathcal{E}}{\partial \lambda} = \text{const.} = \mathcal{E}_0, \tag{2.3}$$

which can be regarded as an equipartition theorem, with the energy equally distributed among all degrees of freedom (that is, the spectral wavelengths) due to the strongly chaotic nature of the system. Equipartition is at the foundation of classical statistical mechanics, and forms the basis for thermodynamic ensembles and the observation of different phases of matter [38]. Applied to photonics, we have the remarkable opportunity of exploiting this principle for enhancing the energy confinement properties of photonic structures. As already discussed above, this opportunity was confirmed by calculating the energy stored for a broadband source in the two limiting conditions of a fully chaotic geometry. (Fig. 2.3, squares) and a non-chaotic geometry (Fig. 2.3, circles), finding a sixfold enhancement in the chaotic case.

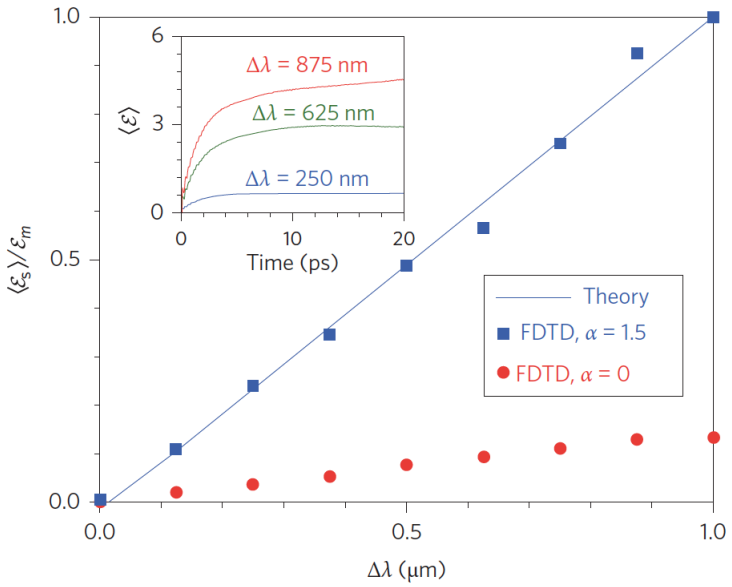

Figure 2.3: Results for a variable-bandwidth source. FDTD calculated average energy $\langle \mathcal{E} \rangle$ versus time for $\alpha = 1.5$ and different normalized bandwidth $\Delta\lambda$ symmetrically centered at 800 nm. Inset: FDTD computed steady-state average energy $\langle \mathcal{E}_s \rangle$ versus bandwidth $\Delta\lambda$ for $\alpha = 0$ (circle markers) and $\alpha = 1.5$ (square markers). The solid line indicates the behaviour predicted by equation 2.3. The energy $\langle \mathcal{E}_s \rangle$ is normalized to the maximum value $\langle \mathcal{E}_m \rangle$ attained for $\alpha = 1.5$ and $\Delta\lambda = 1\mu$m.

2.3 Two-dimensional experiments in photonic-crystal cavities

Energy equipartition and chaotic energy harvesting occur because of the convergence of the modal lifetimes towards a single value τ_{k0}. We therefore begin our experiments by investigating the occurrence of this phenomenon in real structures with controllable chaoticity. We designed and experimentally realized a series of planar two-dimensional stadium-shaped resonators in planar photonic crystals fabricated in Silicon On Insulator (SOI). The substrate consists of a 220-nm-thick silicon layer on a 2-mm-thick insulator buried oxide. The patterns were written into ZEP resist on a modified LEO/RAITH system with 2 nm step size and etched with a 50:50 mixture of SF_6 and CHF_3 gases in a reactive ion etching machine. After stripping the residual resist, the sample was cleaved for end-fire coupling.

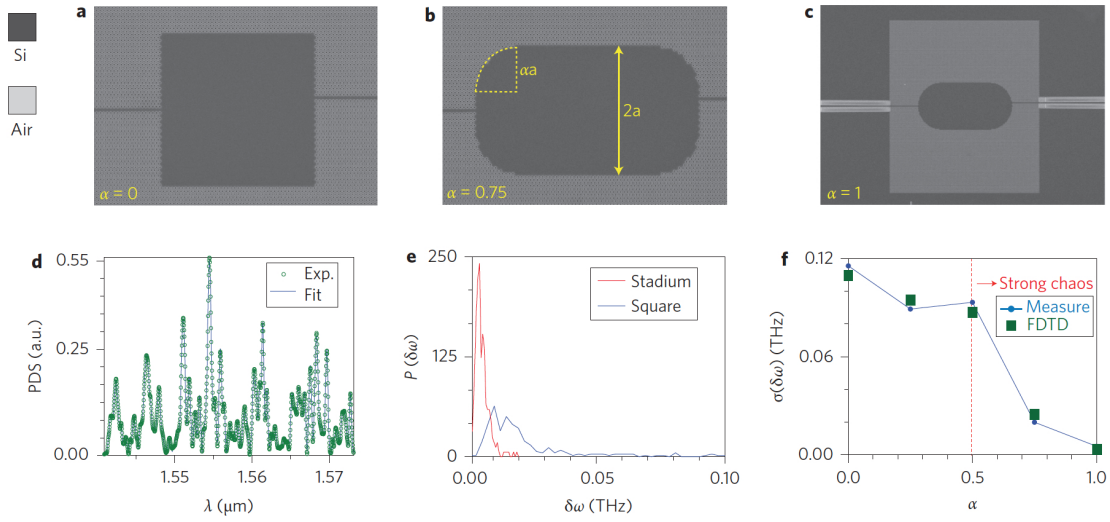

Figure 2.4: Summary of two-dimensional experimental results. (a) to (c) SEM images of the sample geometry for $\alpha = 0$ (a), $\alpha = 0.75$ (b) and $\alpha = 1$ (c). (d) Experimental spectrum (circles) and theoretical reconstruction via wavelet multiscale analysis (solid line) for $A = 400\mu m^2$ and $\alpha = 1$; PDS, power density spectrum. (e) Probability distribution $P(\delta\omega)$ of the resonance widths $\delta\omega$ calculated for the fully chaotic resonator ($\alpha = 1$). (f) Standard deviation $\sigma(\delta\omega)$of the resonance widths versus α.

Figure 2.4 a-c presents a set of scanning electron microscopy (SEM) images that illustrates how the shape of the resonator evolves with a change in the deformation parameter α. The shape starts as a regular square (Fig. 2.4,a) for $\alpha = 0$ and becomes a fully chaotic stadium-shaped resonator (Fig. 2.4c) for $\alpha = 1$, with strong chaos already developed for $\alpha \geq \alpha^* = 0.5$. Since the α is an geometric dependent parameter, the value goes from 0 to 1 in this case, which is different from the previous Robnik billiard with $0 \leqslant \alpha \leqslant 1.5$. The parameter $a = \sqrt{A/(4+\pi\alpha^2)}$ guarantees a constant resonator area A as α is varied (Fig. 2.4b). As the photonic-crystal lattice was designed to exhibit a bandgap around $1.5\mu m$ with a bandwidth of $\sim$ 400 nm, any electromagnetic wave in this range is perfectly reflected at the photonic-crystal boundaries, and can only escape via the input/output waveguides of the structure or by scattering at imperfections. The system can therefore be described as a two-dimensional resonator with measurable losses, and the modal decay constants τ_k can be extracted from the transmitted spectrum. We used the multiscale analysis described in ref. [39], which provides an excellent reconstruction technique even when the resonances overlap. The method fits the spectrum by means of a sum of suitable wavelet functions, allowing the wavelength position λ_0 and the width$\delta\lambda$ of each mode to be computed. The resonance widths $\delta\lambda$ are then inversely proportional to the modal decay rates $1/\tau_k = \delta\omega = c\delta\lambda/n\lambda_0^2$ (ref. [12]). To collect statistically relevant data, we fabricated several samples with different areas A (400 μm^2, 800 μm^2 and 1200 μm^2), and for each area we considered five different degrees of chaos, expressed through the deformation parameters $\alpha = 0$, 0.25, 0.5, 0.75 and 1. To characterize the samples, we used polarized light in the wavelength range 1520-1620 nm. Figure 2.4d shows a portion of one of the measured spectra, together with its reconstruction via multiscale analysis [39], which shows a perfect reproduction of the experimental results. All spectra (not shown here) have been reconstructed with the same level of accuracy. We are able to ex-

tract $\sim$ 2000 resonances for each a, which allows us to extract statistically relevant trends. Figure 2.4e displays the resonance linewidth probability distribution $P(\delta\omega)$ for $\alpha = 1$ (stadium) and $\alpha = 0$ (square). We note that for $\alpha = 1$, the resonances are strongly converging towards a value of $\delta\omega \simeq 5 \times 10^{23}$ THz with only negligible contributions arising from the short-lived modes that are characterized by a larger $\delta\lambda$. Conversely, in the non-chaotic regime, we observed the presence of many short-lived resonances, indicated by the presence of data points up to, and even beyond 0.1 THz, as well as the wider probability distribution observed at low frequencies. To study the convergence of the lifetimes towards a single value, we group the data for different A and the same a together, and calculate the standard deviation $\sigma(\delta\omega)$ of the resonance widths $\delta\omega$. Figure 2.4f illustrates the results of this analysis. In perfect agreement with our theoretical predictions and ab initio simulations (Fig. 2.4f, FDTD symbols), we observed a significant narrowing of the linewidth distribution above the threshold for chaos. It is worth highlighting that this convergence of the linewidth towards a single value does not depend on A, but only on a, which is a clear experimental demonstration that the phenomenon relies entirely on the chaotic properties of the motion of light. The consequences of such an experimentally demonstrated collapse are shown in Fig. 2.5, where we have calculated, by ab initio simulations, the energy trapped in the structure with same area. As seen, the energy increases by a factor of 207% in the chaotic structure. Considering the small bandwidth of the signal ($\sim$100nm), this is a remarkable result demonstrating the superior energy storage ability of the chaotic cavity compared to the regular counterpart.

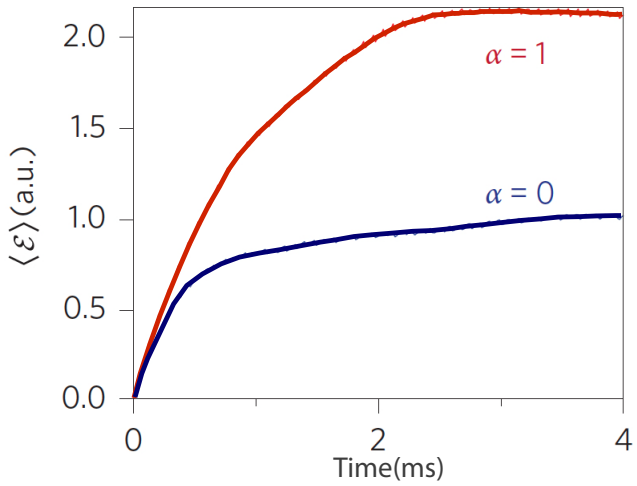

Figure 2.5: Energy trapping in two-dimensional resonators. FDTD calculated averaged energy $\langle \mathcal{E} \rangle$ evolution in the two-dimensional photonic-crystal structure in fully chaotic ($\alpha = 0$) and non-chaotic ($\alpha = 1$) conditions.

2.4 Three-dimensional experiments with deformed microspheres

An ubiquitous technology should not rely on complicated optimization processes, but should instead be reliable and simple to develop. In the previous section, we tuned the chaoticity of the structure to reach full chaos, thus obtaining a 207% increase in energy. However, even when chaos is not fully developed in phase space, the presence of chaos increases the similarity of the lifetimes and leads to broadband energy storage (Figs 1c, 2b,c). We can therefore exploit chaotic harvesting even for very simple conditions, where fine-tuning of chaos is not provided.We accomplished this final step in a three-dimensional system, which incidentally also proves how the physics of chaotic resonators is independent of the dimensionality of the problem. In particular, we used polystyrene microspheres and studied the absorption when their spherical shape is deformed and the symmetry of the system is broken, thus providing chaotic light motion.

Our sample consists of a low-density monolayer of microspheres (Fig. 2.6a) that are deformed by mechanical compression (Fig. 2.6b) in order to obtain an asymmetric shape such as that shown in Fig. 2.1b. Monolayer fabrication was performed using convective assembly [40, 41], where the microspheres are self-assembled on a substrate using a deposition blade (Fig. 2.6a). The blade height was set at 12 μm from the substrate (sphere size of $\sim$10μm) to ensure the formation of a single layer. Following deposition, a glass slide was placed on top of the microspheres for heating and applying mechanical pressure. Deformation was realized by heating the system slightly beyond the glass transition temperature T_g of polystyrene ($T_g = 25^oC$; ref. [42]), which softens the microspheres sufficiently to deform their shape (Fig. 2.6b,c). Compression and heating were performed with an Instron 5960 dual column tabletop universal testing system. The pressure force was ramped to 500 N

over 2.5 min. Figure 2.6d,e presents optical micrographs of a microsphere before (Fig. 2.6d) and after (Fig. 2.6e) compression, highlighting the asymmetric deformation.

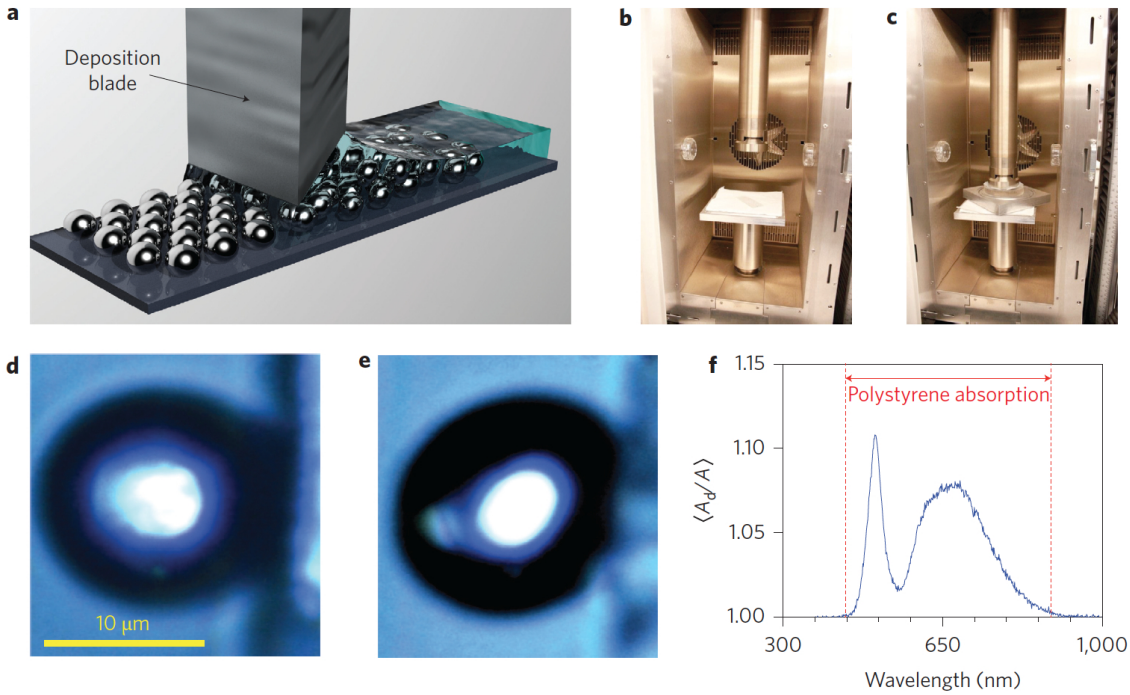

Figure 2.6: Summary of the three-dimensional experimental results with deformed microspheres. (a) Sketch of monolayer sample fabrication by convective self-assembly. (b) and (c) Furnace for sample heating and deformation with mechanical pressure. (d) and (e) SEM images of a microsphere in the original (d) and deformed (e) case. (f) Average normalized absorption of the deformed microsphere $\langle A_d/A \rangle$, measured for different wavelengths and normalized with respect to the undeformed case $\langle A \rangle$.

We evaluated the energy harvesting capacity of this system by performing absorption measurements on a single sphere in both deformed and undeformed conditions. To acquire sufficiently large statistics from different input conditions, we placed our sample on a goniometric stage and, through a series of pump-and-probe measurements, calculated the absorption of the sphere at various illumination angles in the range of $\pm 30^o$. During each measurement, we illuminated the sphere with a broadband source (consisting of a halogen lamp with bandwidth of $\sim$1 μm centered at

700 nm) and measured the absorption A from the relation $A = 1 - T - R$, where T and R are the transmittance and reflectance of the microsphere, respectively. To properly collect the scattered light, transmission and reflection spectra were measured in the near field with a lens with a high numerical aperture. The data were acquired with an Ocean Optics QE65000-FL spectrometer.

Figure 2.6f shows the average absorption $\langle A_d/A \rangle$ of the deformed system, where A_d and A are the absorption measured in the deformed and undeformed case, respectively. For every angle we obtained an increased absorption due to deformation, with a variance of less than one percent (¡0.2%). This originates from the larger electromagnetic energy stored by the microsphere in the deformed case, which led to a higher absorption in the entire absorption window of polystyrene (Fig. 2.6f). Near the wavelength λ=450nm, in particular, the average absorption increases by ∼12%, whereas in the region where the optical spectrum contains the maximum power (∼600 nm), the absorption shows a broadband increase of ∼68%. The chaotic enhancement of the absorption is greater in the spectral region where A is larger and the energy trapped is higher. Outside the absorption frequency window of polystyrene (Fig. 2.6f, dashed lines), as expected, the chaotic energy accumulation does not induce any measurable variation of the absorption. It is worth noting that an absorption increase of ∼12% over a large bandwidth of 400 nm in a transparent material such as polystyrene is quite a remarkable result. Since the deformation in three diminutional cannot not be precisely controlled experimentally, the increment is not as large as the results from simulations.

2.5 Discussion

Our results have addressed the problem of light trapping in chaotically deformed resonators and demonstrate the possibility of exploiting equipartition and chaos as a new avenue for energy harvesting. Equipartition, in our case, is manifested by the uniform distribution of energy among all degrees of freedom of the chaotic resonator, that is, the cavity modes. The process is equivalent to the Brownian motion of particles in a liquid, where each particle carries the same amount of energy. In a liquid, the particles always achieve a uniform distribution regardless of the shape of the vessel in which they are contained. In our optical analogue, the steady state of chaotic modes also does not depend on the particular realization of the resonator, but only on its macroscopic geometry, for which the only requirement is to support chaotic trajectories for the trapped light. Besides the obvious implications at the fundamental level, where we demonstrated the existence of a fundamental principle of thermodynamics in the framework of photonics, our results also have real-world practical implications. The cost of many semiconductor devices, for example, light-emitting diodes and solar cells, is determined to a significant extent by the cost of the material. We show that the functionality of a given geometry can be enhanced up to sixfold by changing the shape alone, that is, without increasing the amount of material and without increasing the material costs. Furthermore, a chaotic system is easier to fabricate as the tolerances are relaxed. Our results can also be extended beyond microresonators, as the phenomenon of chaotic scattering is ubiquitous and also occurs at the nanoscale, that is, when light diffuses into random aggregates of scatterers [43]. We therefore envisage that our ideas will stimulate new research in the assembly of new random nanostructures for efficient energy harvesting.

2.6 Time dependent coupled mode theory

Figure 2.7 a shows a TDCMT model of the light-resonator system. In this scheme, the environment is represented as a waveguide side coupled to the resonator. The input signal S(t) interacts with the resonator through the coupling coefficient γ and transfers energy to the modes of the cavity $a_k(t) = A_k e^{i\omega_k t - t/\tau_k}$ ($k \in [1, N]$), being ω_k the frequency, $1/\tau_k$ the lifetime, A_k the amplitude and $\mathcal{E}_k = |a_k|^2$ the energy carried by the k?th mode. The total energy stored in the resonator is $\mathcal{E} = \sum_k \mathcal{E}_k$. Decay rates $1/\tau_k$ can be further decomposed as follows $1/\tau_k = 1/\tau_{k0} + 1/\tau_e$, with $1/\tau_{k0}$ the intrinsic decay constant of the mode and $1/\tau_e$ the decay constant due to coupling with the source. Cavity modes obey the following evolution equations [12]:

$$\frac{da_k}{dt} = \big[i\omega_k - (1/\tau_k)\big]a_k + \gamma \cdot S(t), \quad k \in [1, ..., n] \tag{2.4}$$

with $\gamma = \sqrt{1/\tau_e}$, while reflection $R = \sum_k R_k$ and transmission $T = \sum_k T_k$ are given by the following expresions:

$$R_k = -\sqrt{1/\tau_e}a_k, \quad R_k = -\sqrt{1/\tau_e} + S \tag{2.5}$$

with R_k and T_k the reflection and transmission oft he k?th mode,respectively. In the presence of a single frequency excitation $S = e^{i\omega t}\Theta(t)$ switched on at t=0, with ?$\Theta(t)$ being the Heaviside function, Eq. 2.4 are readily solved for each a_k and read:

$$a_k = \sqrt{\frac{1}{\tau_e}}\frac{e^{i\omega t} - e^{i\omega t - t/\tau_k}}{(\omega - \omega_k)^2 + 1/\tau_k^2} \tag{2.6}$$

For a broad bandsource, $S = \int e^{i\omega t}\Theta(t)d\omega$, the total electromagnetic energy $\mathcal{E} = \sum_k |a_k|^2$ stored in the cavity is readily found to be:

$$\mathcal{H} = \int \frac{d\omega}{\tau_e}\sum_k \frac{1 + e^{-2t/\tau_k} - 2e^{-t/\tau_k}\cos[(\omega - \omega_k)t]}{i(\omega - \omega_k) + 1/\tau_k} \tag{2.7}$$

Equation 2.7 can be further simplified as the integral yields significant contributions only for $\omega \approx \omega_k$, and we obtain:

$$\mathcal{H}\tau_e = \sum_k \tau_k^2 (1 - e^{-t/\tau_k})^2 \tag{2.8}$$

The power $\mathcal{P}_k$ transferred into the k?th mode is conversely evaluated from the energy balance equation:

$$\frac{\partial |a_k|^2}{\partial t} = \mathcal{P}_k = |S|^2 - |\mathcal{R}_k|^2 - |\mathcal{T}_k|^2 \tag{2.9}$$

that,in conjunction with Eqs 2.5 and 2.6, yields:

$$\mathcal{P}_k = \frac{2\frac{\tau_e}{\tau_{k0}}}{(1 + \frac{\tau_e}{\tau_k 0})^2} |S|^2 \tag{2.10}$$

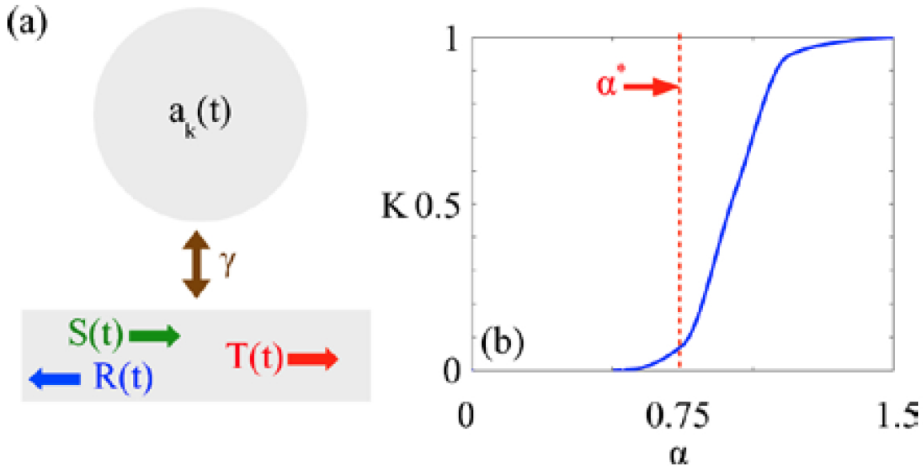

Figure 2.7: Coupled mode theory modelling and characterisation of chaos. (a) light-cavity interaction TDCMT scheme: S(t) is the input source, R(t),T(t) are reflection and transmission signals, respectively, a_k is the k-th mode in the resonator and γ is the coupling coefficient between the resonator and the external environment; (b) normalized entropy K versus chaotic degree for the Robnik billiard expressed by Eq. 2.1.

2.7 Characterization of chaos

We quantitatively describe the chaoticity of light motion by evaluating the relative area of the resonators phase space that encompasses chaos. This is achieved by first calculating the distribution of the Lyapunov exponent [43] in phase space,and then performing a weighted summation by assigning 1 if the Lyapunov exponent is positive,and 0 otherwise.The resulting quantity K can be regarded as a normalised version of the Kolmogorov Sinai entropy [43, 44]. In particular, When K=0, the resonator dynamics exhibits no chaos and the resulting motion is totally reversible, while for $K = 1$ the phase space is totally chaotic and all input conditions lead to chaos. Values of K between these two limiting conditions indicate a phase space partially chaotic, with K measuring the relative area of the chaotic sea with respect to the reversible portion of the dynamics. Figure 2.7 displays the behaviour of K for the billiard expressed by Eq 2.1. For α lower than the threshold value $\alpha^* = 0.75$, no chaos is observed in the structure,while for $\alpha > \alpha^*$, strong chaos is generated through the shape deformation. At $\alpha = 1.5$, the structure is fully chaotic and the phase space is totally dominated by a single chaotic sea.

Chapter 3

HARNESSING STRUCTURAL DARKNESS IN THE VISIBLE AND INFRARED WAVELENGTHS FOR A NEW SOURCE OF LIGHT

3.1 Introduction for blackbody

A black body is an ideal dark material, the practical realization of which can enable efficient technologies in many fields [45, 46, 47, 48, 49, 50, 51, 52, 53]. A black body can emit the same amount of energy as it absorbs [54], which makes it not only the perfect absorber, but also an ideal thermal source [55, 56]. To date, the best blackbody realizations have been reported with carbon nanotubes, which achieve 99.95% absorption with thickness of 800 μm, and broadband absorption between 98 and 99% for thicknesses of 300-500 μm under normal incidence [13, 57]. The design of these media is typically guided by the principle of optimizing lightmatter

interactions in a suitable resonant system of finite size, which represents the absorber [50, 13, 57, 58, 59, 60, 61, 62]. In this Article we wish to explore a different approach, which takes inspiration from natural structures that show an incredible whiteness, and thanks to the idea of chaotic energy harvesting [63], reverses the effect in a biomimetic material that is completely dark. The material is based on the random assembly of specific nanoparticles, which show an extremely strong darkness even in microscopic concentrations. We have developed a wetchemistry synthesis that can fabricate these nanostructures on large scales with minimal costs. Traditionally, the concept of a blackbody is usually associated either with strong absorption or the incoherent emission of energy [54]. When energy is emitted incoherently, each frequency in the spectrum behaves independently from the others, and they do not interact constructively. Pioneering investigations in resonant systems show that constructive wave phenomena, if properly exploited, can have a dramatic impact on energy emission [64, 65, 66, 67, 68]. Our nanomaterial does not possess any resonance, as it appears totally black. However, in the presence of an optical amplifier, it sustains surprising emission dynamics. In a series of experiments performed with an optical dye, we show that the light-matter interaction generates a process of light condensation, where all available energy is constructively transferred on a single spectral frequency and spontaneously emitted as monochromatic light. This opens up the possibility of the use of dark nanomaterials as new types of coherent energy sources.

3.2 Sample design

Figure 3.1 illustrates, on very simple physical grounds, the idea for the design of our material. A full wave analysis of the system is presented in Section 3.7 and illustrated in Fig. 3.17. The starting point of our discussion stems from the camouflage of a specific species of beetle, the Cyphochilus. After millions of years, this little animal has developed a unique ability for the generation of ultra-brilliant shells [69]. This color is the result of disordered thin scales, which scatter light chaotically in all directions. To reverse this effect we developed a complex porous system (Fig. 3.1a), which is composed of a region of space (Fig. 3.1a, gradient blue area) to which is attached a random network of pores made of infinitely long, metallic waveguides. Light propagating in the space bounces continuously within the system (Fig. 3.1a, solid green line) until it reaches one of the pores. The left panel of Fig. 1b presents a two-dimensional projection of the dynamics along the $x' - y'$ plane. When impinging on a generic pore, some light is coupled into the waveguide channel, and the remaining energy is scattered back. Light entering into the waveguide (Fig. 3.1a,b, darker areas) never returns (due to the infinite length of the channel) and is fully absorbed into the pore (Fig. 3.1b, left panel, darker area). The disordered distribution of pores completely randomizes the reflections of light, providing a source of chaotic light scattering. In these conditions the system dynamics is equivalent to a Brownian motion, whereby equivalent light particles diffuse, generating an electromagnetic response that becomes almost independent of the input conditions [63]. In the porous system of Fig. 3.1a, the equivalent diffusion forces light to explore the distribution of pores with the same probability irrespective of the input conditions (frequency, angle of incidence and polarization), triggering a process of broadband absorption that creates a completely dark material.

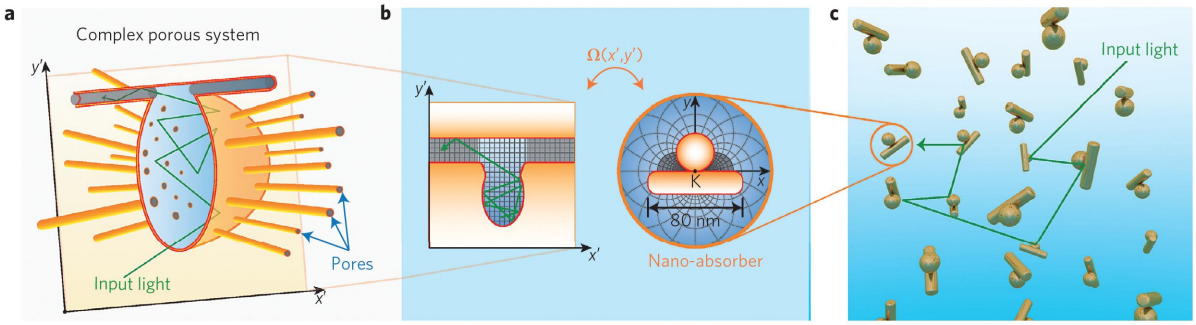

Figure 3.1: From a complex porous system to a nanostructured blackbody for light. (a) Sketch of a porous material composed of a metallic cavity and a random network of pores, each comprising an infinitely long waveguide. (b) Left: section along the $x' - y'$ plane of the porous structure of a, and associated light dynamics. Right: transformed structure obtained by applying a conformal mapping described by the transformation $(x, y) = \Omega(x', y')$ (see Methods for more details). In b (left), the shaded area describing the pore is mapped into the curved area near kissing point K. (c) Illustration of the blackbody structure, composed of a collection of random scatterers, each represented by the nanostructure in b (left). The structure in (c) is fully equivalent to the porous material of (a).

To transform the ideal design of Fig. 3.1a into a realistic structure, we created a suitable illusion by mapping the single pore element of Fig. 3.1 b(left) into the finite nanostructure of Fig. 3.1b (right). This was performed with transformation optics [70, 71] using the coordinate transformation $(x, y) = (x', y')$, which stretches the space so as to emulate an infinitely long material (see Methods for additional details). The two structures shown in Fig. 3.1b display the same electromagnetic behavior. The nano-absorber in Fig. 3.1b (right) comprises a nanorod attached to a nanosphere, which mirrors the pores of the space (x', y') leading into the darker shaded area around kissing point K. Light entering the pores in the transformed space (x, y) has the illusion of propagating into an infinitely long channel, which never terminates. The last ingredient to replicate the structure of Fig. 1a is a disordered distribution of pores, which is accomplished by creating a random collection of nano-absorbers (Fig. 3.1c), each with the structure shown in Fig. 3.1b (right). The two systems in Fig. 3.1a,c, despite their different appearances, are completely

equivalent. It is worth emphasizing that there is no theoretical limit to the absorption power of the waveguide pores, as they represent channels of infinite length. However, non-idealities in the design of Fig. 3.1b (right), such as surface roughness in the nanosphere, lead to the appearance in space(x', y') of scattering objects inside the channel pores that produce unwanted reflections.

3.3 Sample fabrication

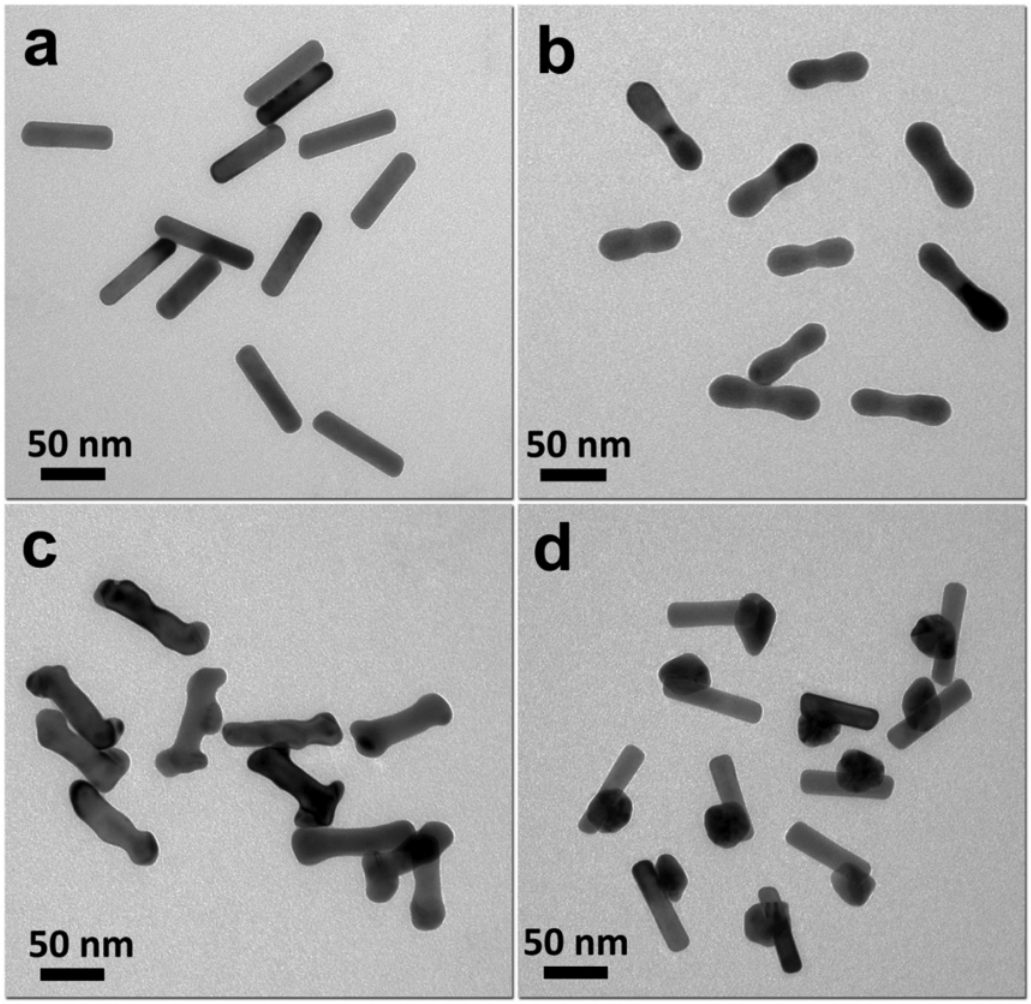

Figure 3.2: TEM images of (a) the gold nanorod seeds and (various nanostructures after seeded growth with different concentrations of 4-MP: (b) $C_{4-MP} = 0mM$, (c) $C_{4-MP} = 1mM$, (d) $C_{4-MP} = 10mM$

We used seed-mediated method to synthesize to designed particle [72, 73]. We started with single crystalline gold nano rod with the length 75.3±7.4 nm and radius 9.2±0.8 nm as shown in Fig. 3.2 a. We first incubated nanorods in thiol ligand 4-mercaptophenol (4-MP) with gold precursor $HAuCl_4$ and reducing agent ascorbic acid. The connection of 4-MP plays an detrimental role in the final shape of the nanoparticles. When the concentration of 4-MP C_{4-MP}=0, the gold ions continuously accumu-

lated to the nanorod, and formed a peanut-like structure as shown in Fig. 3.2b. When the concentration C_{4-MP} increased to 1mM, the gold can grow on the seed crystal, but with irregular shape as shown in Fig. 3.2c. Quite interestingly, when properly set to C_{4-MP} =10mM, we successfully synthesized the design dimer structure with a remarkable high yield beyond 90%, with a single nanosphere settling on the nanorod seed, as illustrated in Fig. 3.2d. The metallic bonding between the sphere and rod differs out dimer from the one connected with surface ligands, providing excellent stability. The variation of the shape demonstrates the impact of the concentration C_{4-MP}: the high concentration enhances the asymmetric growth and suppresses the epitaxial growth of the gold layer on the seed. When we further increased the concentration C_{4-MP} beyond 15mM, we did not observe any secondary growth, indicating that the high concentration of 4-MP ligands may reduce the gold ions.

Thanks to the mediate growth speed, we can track the dynamics of the formation of the dimer by quenching the reaction at the intermediate states under Transmission Electron Microscopy (TEM). Figure 3.3 summarized the TEM images at different reaction time t when ascorbic acid is added to stop the reaction. When $t = 3s$, we observed the initial emergence of nanosphere on the nanorod. The High Resolution Transmission Electron Microscopy (HRTEM) in Fig.3.3f clearly demonstrates a small particle around 3nm is formed on the nanorod seed long [111] direction. Fast Fourier Fransform (FFT) diffractogram in Fig. 3.3g and h demonstrates the stacking faults existing in the budding rods while the sphere is defect-free. During the period 3s$\leq$ t $\leq$ 20s, the tiny buds gradually grow int to larger irregular agglomerates, as seen from Fig. 3.3b and c. For the final step when t$\geq$60s, the agglomerates re-crystallized to fuse into a large gain, eliminating the boundaries. Despite the different geometries of the agglomerates, it finally developed into a single sphere as shown in Fig .3.3e. The longer the reaction time, the smoother the surfaces.

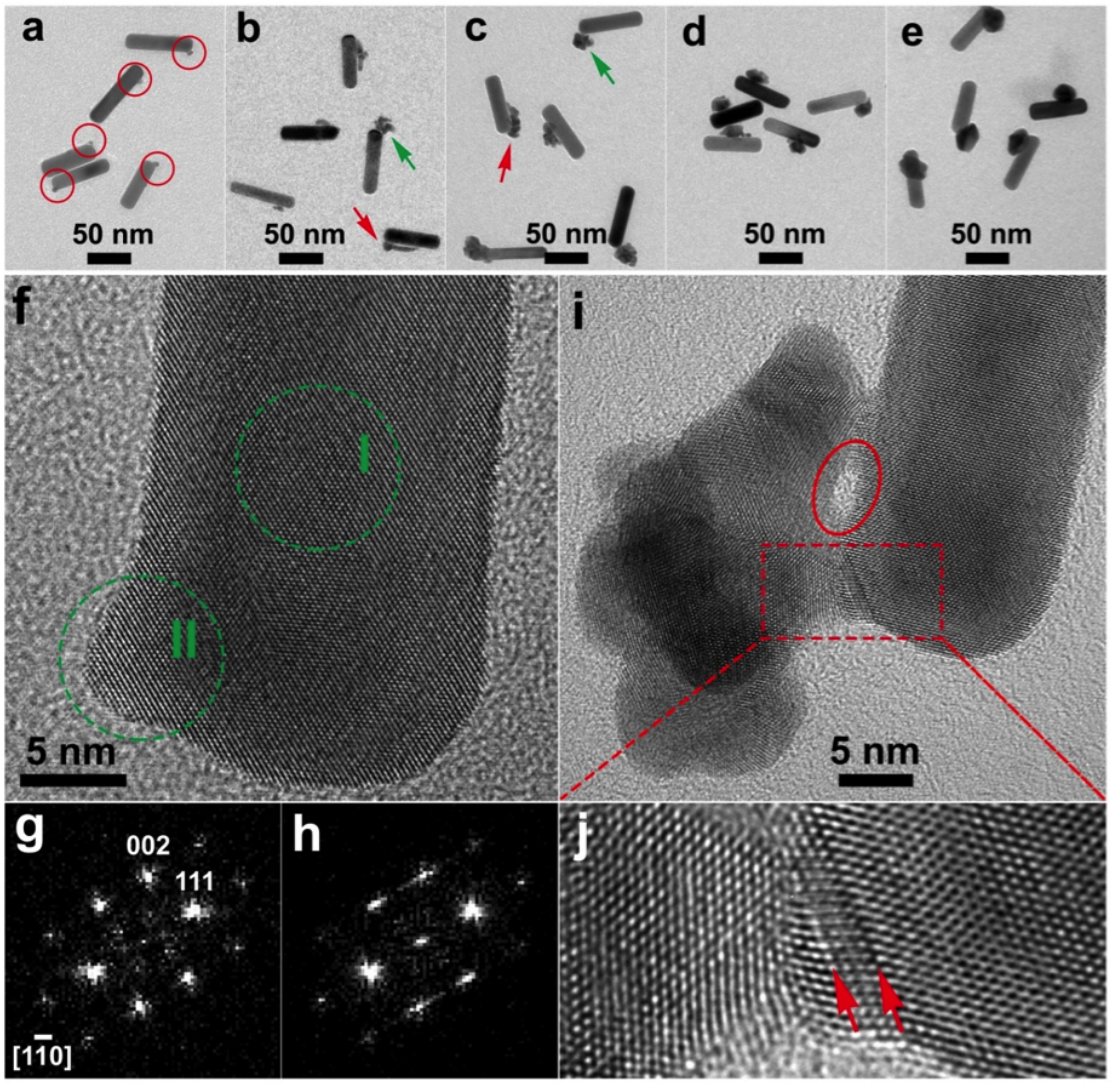

Figure 3.3: TEM images of intermediate states of the dimer at different seeded growth stages, which were obtained by quenching the reaction at (a) 3, (b) 10, (c) 20, (d) 60, and (e) 180 s. The circles in (a) encircle the tiny budding particles. The arrows in (b and c) indicate worm-like agglomerates (red arrows) and cauliflower-like agglomerates (green arrows). (f) HRTEM image of the intermediate at 3 s taken along the [1$\bar{1}$0] axis of the gold nano rod, showing a small particle protruding falong the [111] direction. (g, h) FFT diffractograms of (g) region I and (h) region II marked in (f). The diffuse reflections in (h) are indicative of the presence of stacking faults. (i) HRTEM image of the intermediate at 20 s taken along the [11$\bar{0}$] axis of the nanorod. The ellipse indicates a gap formed by the cauliflower-like agglomerate and the nanorod. (j) Enlarged HRTEM image of the interface region marked in (i), in which two arrows point to nanotwin boundaries.

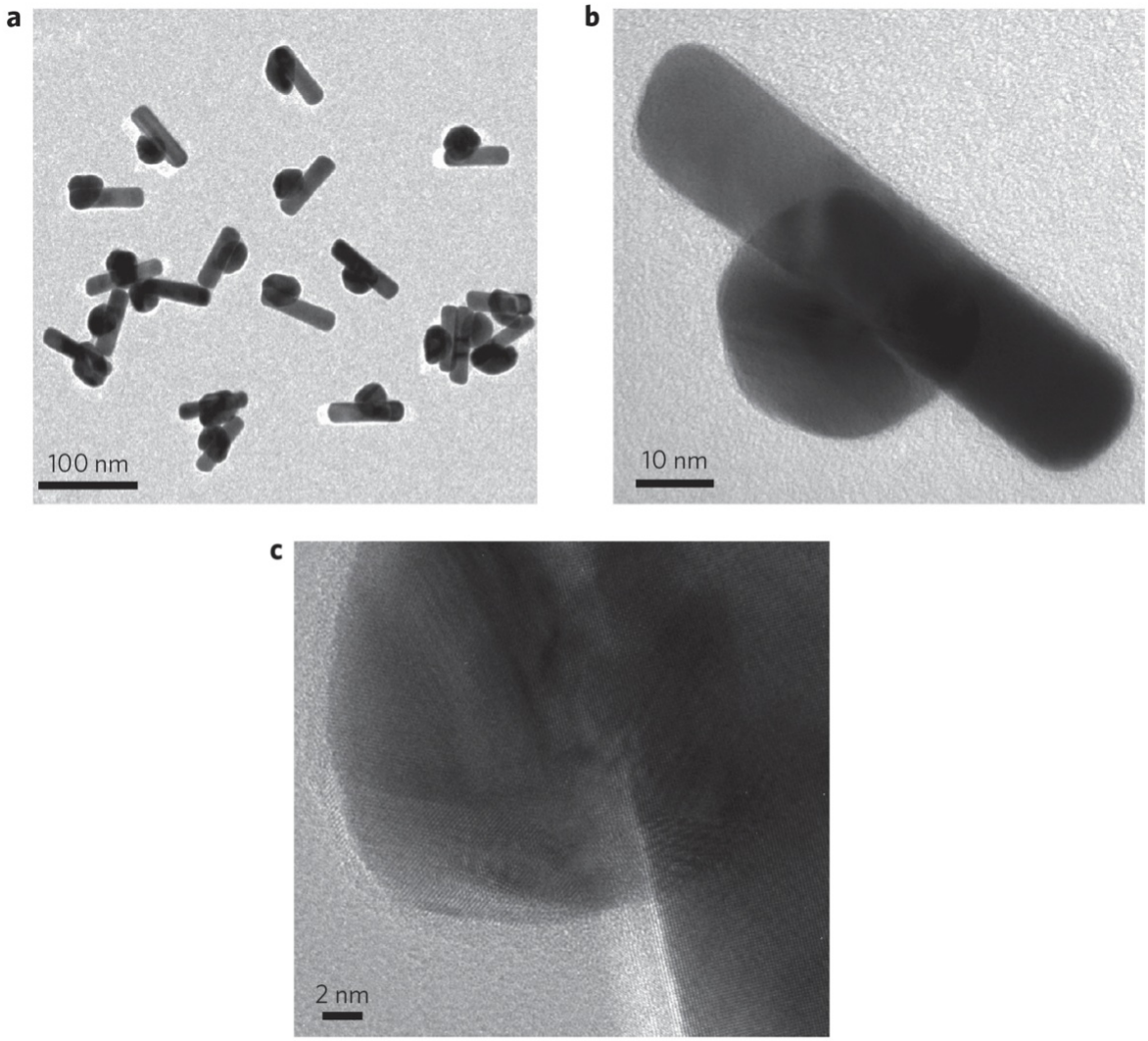

Figure 3.4: Optical blackbody, the fabrication of which occurs via seeded growth of Au nanospheres from Au nanorods. (a) Low-magnification TEM image of a realized sample. (b) TEM image of a single nanostructure. (c) HRTEM image near the kissing point between the nanosphere and the nanorod.

Figure 3.4a presents a TEM image of a representative sample, and Fig. 3.4b shows a detail of a single absorber. Each nano-absorber is composed of a nanorod of length 75 ± 7 nm and diameter 18 ± 2 nm and a nanosphere with a diameter of 30 ±3 nm. Figure 3.4c presents a HRTEM image of the crystal structure near the kissing point K between the nanosphere and the nanorod, showing the clear sharp corner

formed by metallic bonding of the differently curved surfaces of the rod and the sphere, which have the same crystalline structure. This structure provides excellent thermal stability properties, as shown in Section 3.8 with Fig. 3.7 to Fig. 3.15.

3.4 Tuning structural darkness

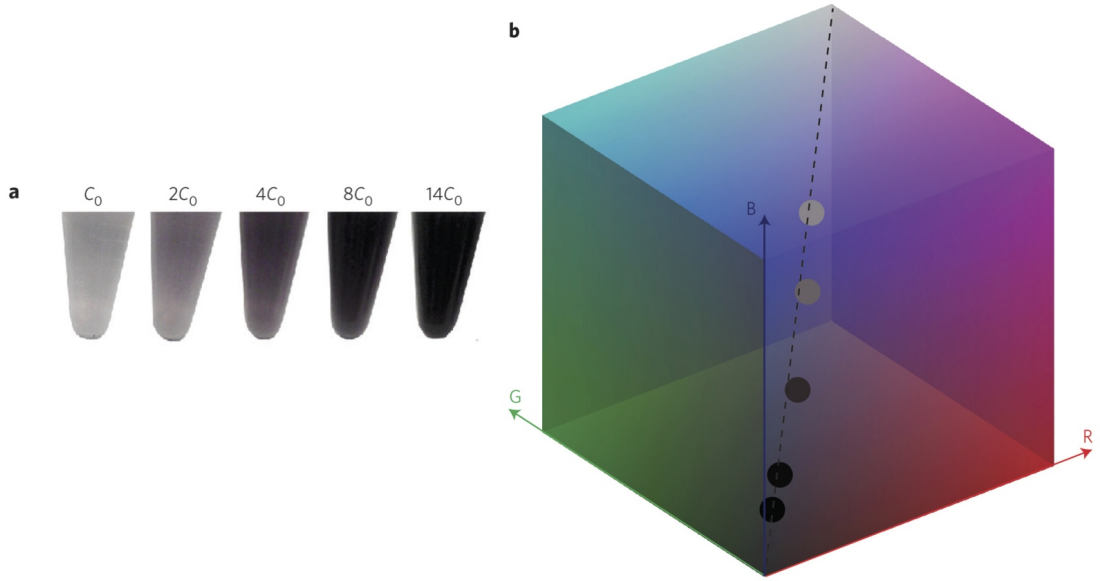

Figure 3.5: Tuning the structural darkness of the samples. (a) Visual appearance of samples at different concentrations, measured as multiples of unit concentration $C_0 = 2.7 \times 10^{10}$ cm^{-3}. (b) Position of each color in the RGB cube, obtained by extracting the relative component of red, green and blue from the corresponding images.

In a first series of experiments we dispersed the nano-absorbers into a liquid host material composed of water and studied the absorption of the nanostructures by varying their concentration as integer multiples of unit density $C_0 = 2.7 \times 10^{10}$ cm $^{-3}$. The value of C_0 was determined using inductively coupled plasma-optical emission spectrometry. In the case of a maximum concentration of $14C_0$, the volume filling fraction f of the nanostructures is microscopic at only $f = 1.9 \cdot 10^{-5}$. Despite the ultra-small concentration, we immediately perceived the absorption power of our nanostructures from the deep dark color acquired by the liquid (Fig. 3.5a, sample $14C_0$). By varying the nanoparticle concentration we observed the generation of different shades of grey (Fig. 3.5a). These were characterized by displaying the corresponding position in a red/green/blue (RGB) cube (Fig. 3.5b). Our mate-

rial displays colors (Fig. 3.5b, circles) on the diagonal connecting the darkest point in the cube with the brightest (Fig. 3.5b, dashed line). This indicates the broadband nature of our absorbers, which at all concentrations display a wide spectral response. Fig. 3.6 illustrates the color achieved by diluting a fixed concentration $14C_0$ of nanospheres, nanorods, as well as a mixture of them, into water. In these cases, the samples acquired only light shades of a red color, with no blackbody feature.

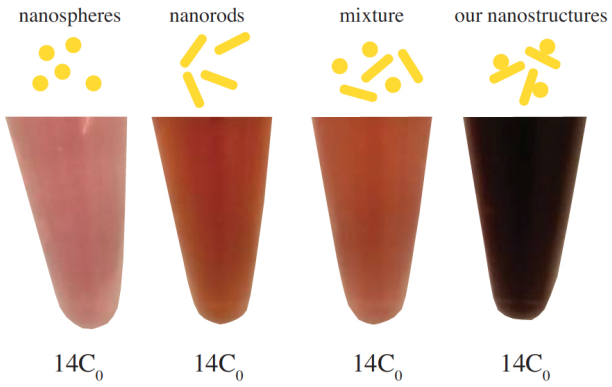

Figure 3.6: Structural darkness of our material versus individual components: nanospheres, nanorods and their mixture. The figure illustrates the structural color formed by (from left to right): individual nanospheres, individual nanorods, mixture of nanospheres and nanorods, and our nanostructures. In all cases we used the same concentration $14C_0$ of nanomaterial.

To quantify the level of darkness achieved by our nanostructures, we measured their absorption using a UV-VIS-IR spectrum analyzer (more details in Section 3.9 and illustrates in Fig. 3.13). The nanoparticles tended to sediment after about 10 days (Fig. 3.7), but sedimentation did not influence the reported results, which are summarized in Fig. 3.9. An integrating sphere was used in the configuration shown in Fig. 3.9a, with the sample placed in the middle of the sphere and off-axis (by angle θ, varying in the range $\pm 70^o$) with respect to the input light. Figure 3.9b presents the results of nanoparticle absorption γ and absorbance δ, the latter defined as

$\delta = \log_{10} \frac{1}{1-\gamma}$. This figure reports individual spectra obtained for each θ (Fig. 3.9b, solid red lines), as well as their average value over rotation angle θ varying in a range of 30^o (Fig. 3.9b, solid black line). In the broadband optical window investigated, the material shows a quite flat absorption spectrum between 98% and 99%, with a peak maximum of 99.2% at $\lambda = 497$ nm. Figure 3.9c presents a detailed plot of absorption versus sample concentration for the specific wavelength $\lambda = 497$ nm, illustrating the possibility to fully tune the material response over a wide range of absorption values between 20% and 99.2%. For concentrations greater than $14C_0$, no appreciable absorption increase is observed. Fig. 3.8 provides a further comparison of our absorbers and commercially available carbon nanotubes.

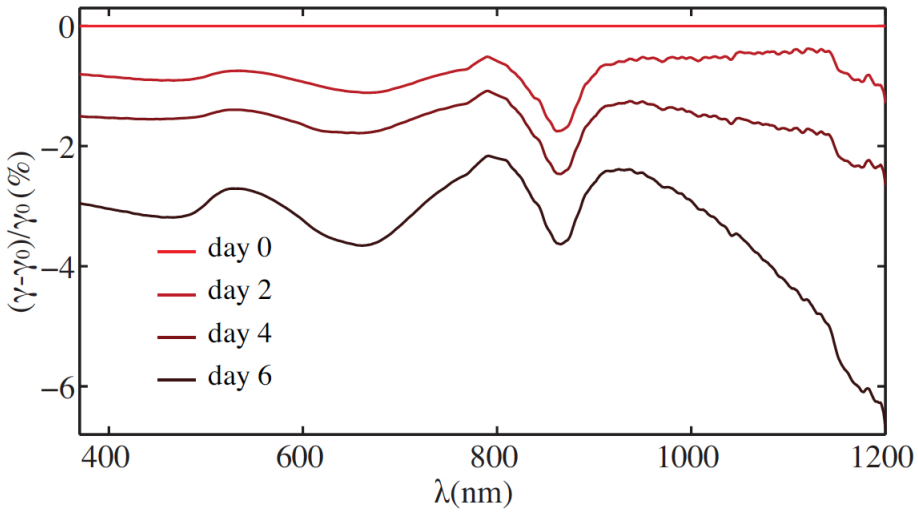

Figure 3.7: Nanoparticles absorption in liquid solution versus time. The figure illustrates the variation $\Delta\gamma = (\gamma - \gamma_0)/\gamma_0$ of nanoparticles absorption γ versus time, being γ_0 the nanoparticles absorption spectrum at day 0. The measurement has been performed by keeping the sample inside the integrating sphere and measuring the nanoparticles absorption day by day.

Achieving strong broadband absorption with a microscopic filling fraction of nanoparticles opens up the possibility of engineering thin-film structures of remarkable absorption power. Through spin coating, a thin layer of nano-absorbers was de-

posited over a Si substrate (Fig. 3.10 a), and the total absorption of the structure was measured with the integrating sphere set-up of Fig. 3.9a, varying the illumination angles between -70^o and +70^o. Figure 3.10b reports the results for normal incidence, and Fig. 3.10c illustrates the absorption averaged over the whole bandwidth between 400 and 1400 nm, for different illumination angles. A layer with a thickness of only 4.9 μm already achieves an average broadband absorption of 95% (Fig. 3.10b, solid red line), with a peak value of 96.8% at $\lambda = 900nm$. On increasing the layer thickness to t = 10.2 μm, we measured an almost flat average absorption of 98.43%, with a peak absorption of 99.7% at $\lambda = 850nm$. These results agree well with the nanoparticle absorption obtained in the liquid sample. The absorption of the sample is virtually insensitive to the illumination angle (Fig. 3.10c). By considering input angles as large as 60^o, the material maintains an impressive average broadband absorption of 98%. To the best of our knowledge, this value of averaged absorption at oblique incidence is the highest reported for a thin structure of 10.2 μm in such a large optical window.

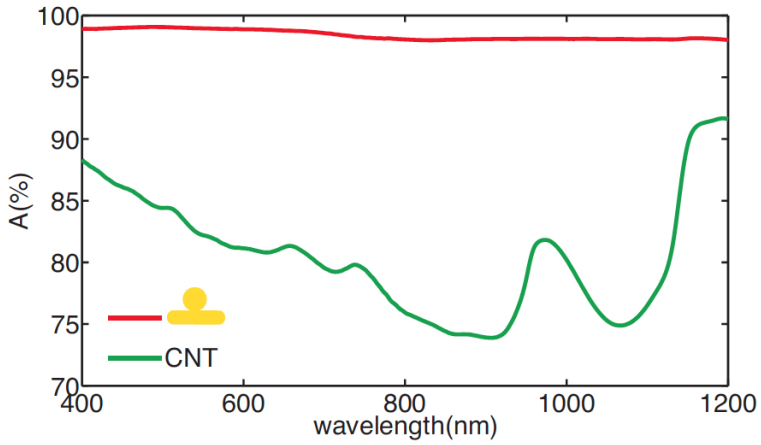

Figure 3.8: Absorption spectrum of our nanomaterial versus carbon nanotubes. The figure compares the absorption spectrum, measured by the integrating sphere configuration of Fig. 3.9a , of our nanostructures (solid red line) and commercial carbon nanotubes (CNT, solid green line). In order to compare the two systems in the same configuration, we used a fixed volume filling fraction of material corresponding to $f = 1.9 \cdot 10^{-5}$, which corresponds to a concentration of nanoabsorbers of $14C_0$. In our experiments, we employed carbon nanotubes from Sigma-Aldrich, with nanotube lengths between 0.3μm - 5μm.

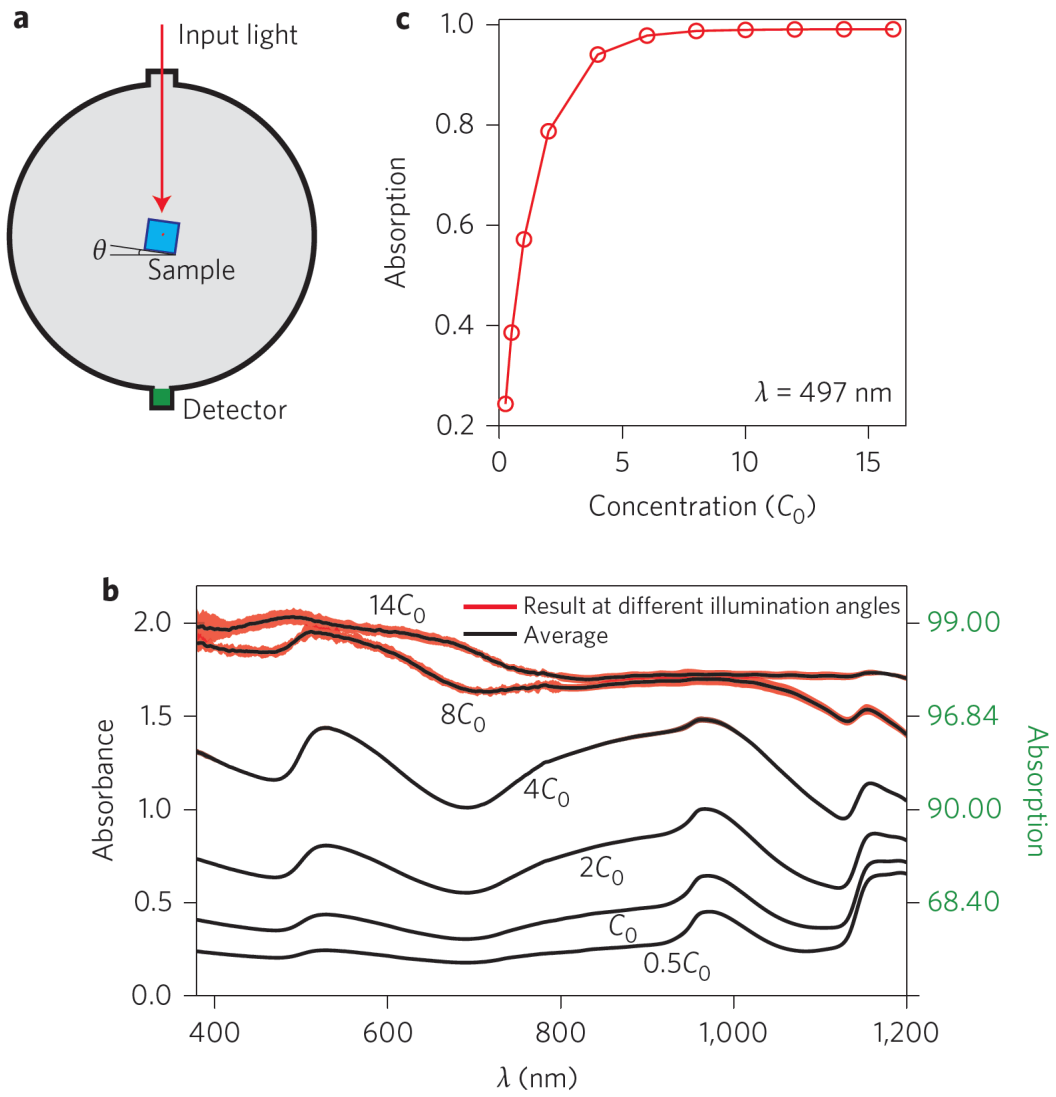

Figure 3.9: Absorption experimental results. (a) Sketch of the integrating sphere set-up used to measure the total integrated absorption. The sample is placed in the middle of the sphere, and a goniometric stage ensures off-axis illumination. (b) Nanoparticle absorption γ and absorbance $\log_{10}(1/(1-\gamma))$ measured between 400 and 1200 nm for varying sample concentration. Both the average value (solid black line) and the result for different illumination angles (solid red lines) is shown. (c) Absorption versus sample concentration (measured in multiples of unit concentration C0) at λ=497 nm.

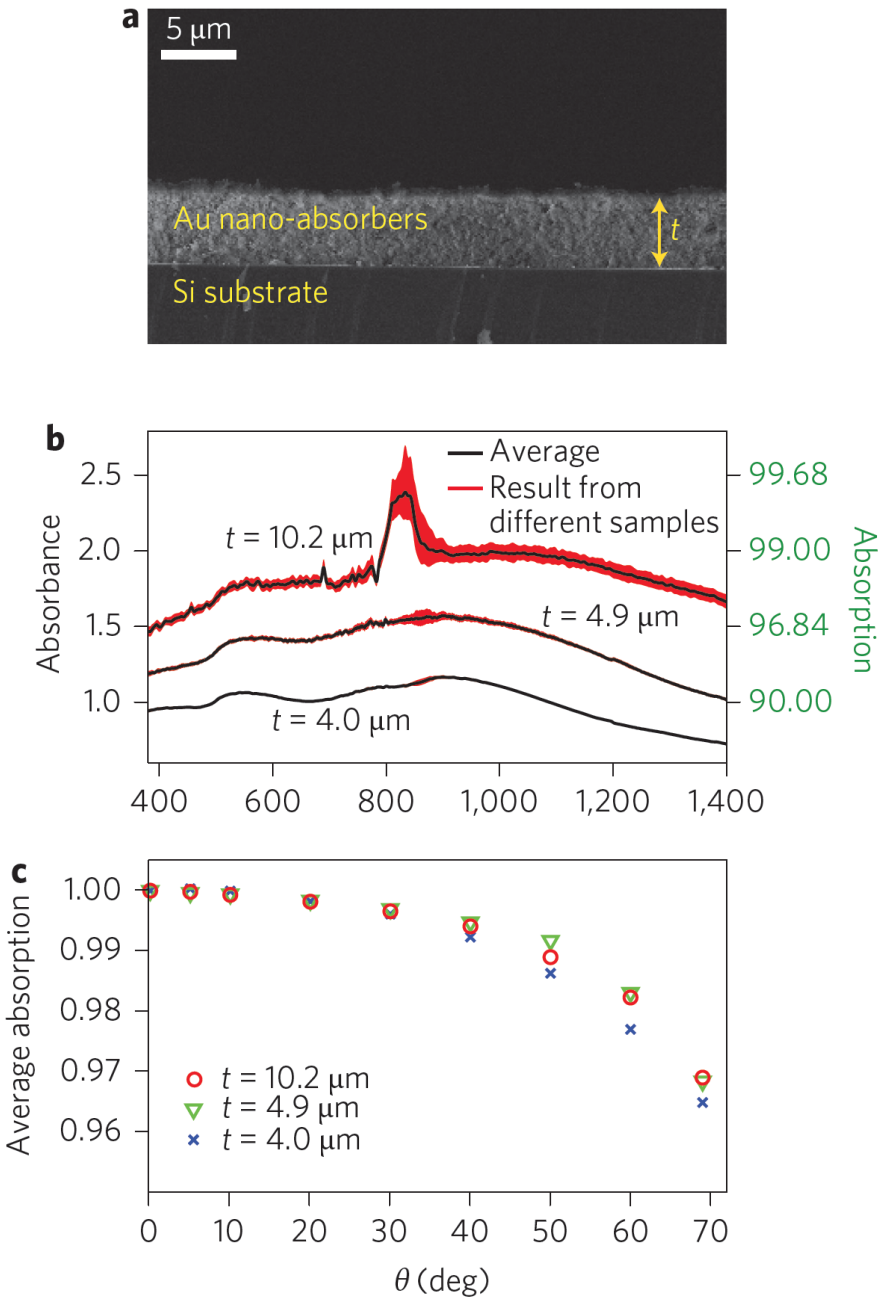

Figure 3.10: Absorption of planar thin films. (a) Scanning electron microscopy cross-section image of a fabricated sample composed of a Si substrate with a deposited thin layer of nano-absorbers. (b) Absorption spectra for different layer thicknesses t under normal incidence illumination. Measurements were performed with the integrating sphere set-up in Fig. 3.9a. Results are shown for different samples (solid red lines), as well as the average value (solid black lines). (c) Average absorption of the sample with varying illumination angle. For each input angle θ, the calculated absorption is averaged in the wavelength range 400-1400 nm (symbols). The average absorption for varying *theta* is normalized with respect to the average absorption under normal incident conditions ($\theta = 0$).

3.5 Light condensation in a structurally dark nanomaterial

The possibility to create thermally stable and versatile dark nanoparticles opens up new possible applications for blackbody materials. An intriguing question is related to the dynamics of a blackbody when placed into an active material that can continuously inject photons into the system. This condition can be realized easily by mixing the nanostructures with a dye optical amplifier, which is pumped to generate photons by fluorescence or stimulated emission. Intuitively, we might expect that all generated photons are absorbed inside the dark nanoparticles. However, if an extremely dark medium such as a blackbody is placed into an environment at non-zero temperature, light absorption becomes mediated by a strong process of thermal emission. We theoretically investigated the physical scenario by developing a quantum statistical model of the lightmatter interaction (more details in Section 3.10). We complemented our theory with experiments with Rhodamine B, a dye with a fluorescence peak at λ=625 nm. An aqueous solution composed of 1.4 mM Rhodamine B and a $4C_0$ concentration of nanostructures ($\approx$95% absorption in the fluorescence bandwidth of the dye) was optically pumped with a pulsed laser emitting 10 ns pulses with a repetition rate of 10 Hz at $\lambda = 532$ nm. Laser light was focused on a 3 mm circular spot at the surface of the sample. The resulting emission spectra were collected by a fibre-spectrograph. Figure 3.11 summarizes the theoretical and experimental results. According to our model, the energy density $W(\omega)$ of the system at thermodynamic equilibrium, and in the presence of an active material that injects photons in a bandwidth $\Delta\omega$, is given by:

$$W(\omega) = \frac{\sqrt{\Delta\omega^2 - \omega^2}}{\pi\Delta\omega^2} \coth\left[\beta\frac{l(P) - \omega}{2}\right] \tag{3.1}$$

where $\beta = 1/T$ is an effective inverse temperature that characterizes the thermodynamic equilibrium state of the material and l is a state parameter that depends on the pumping rate P, which measures the rate of photon number increase in the system. Details on the derivation of this equation are provided in Section 3.10. The condition of thermodynamic equilibrium is a natural hypothesis for our system. The lightmatter interaction with 10 ns pulses at a 10 Hz repetition rate generates photons that scatter inside the dye molecules and the nanoparticles for a very large temporal window before being probed by the millisecond integration time of our spectrum analyzer. This provides the photons with enough time to reorganize their distribution according to the thermodynamic configuration that minimizes the free energy of the system. Figure 3.11a illustrates the results of this process by plotting the behavior of W at different P. At low pumping rates, the emission spectrum does not show any particular behavior and maintains a bell-shaped form in $\omega \in \left[-\Delta\omega, \Delta\omega\right]$ (Fig. 3.11a, for P<2). However, when the pumping becomes stronger (Fig. 3.11a, P>3), a radically different dynamics is observed, in which the blackbody self-redistributes the energy in the spectrum and a condensation process occurs, which constructively builds up photons at the highest frequency $\omega_c = \Delta\omega$. Such counterintuitive dynamics depends on the fact that the condensate represents the most favorable energetic configuration for the system. In this process, the higher the energy that is optically pumped into the blackbody, the stronger the tendency of the system to redistribute the spectral power to create a macroscopic dominant state at the band-edge.

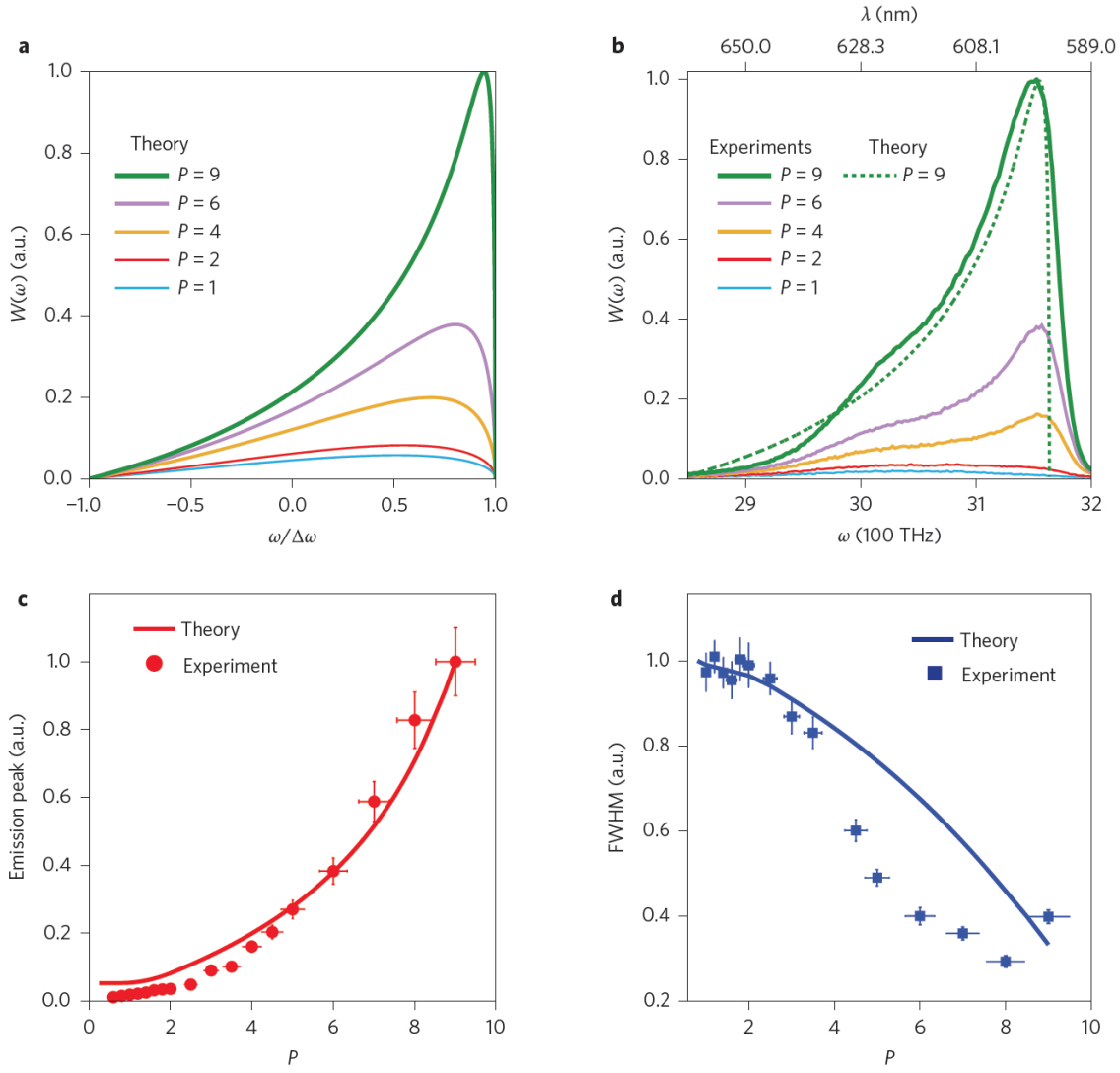

Figure 3.11: Light condensation with dark nanoparticles. (a) Theoretical prediction of the evolution of the energy density spectrum $W(\omega)$ of a blackbody in the presence of an active material, which generates photons in bandwidth δ. The photon number increase is expressed by the pumping rate P, which measures the variation of the total number of photons contained in the bandwidth $\Delta\omega$. The calculations were performed using equation 3.1, with an effective inverse temperature $\beta = 1/T = 1/300$. (b) Experimentally acquired emission spectra, obtained by pumping a Rhodamine B dye with a pulsed nanosecond laser system. Laser input power p was varied between p = 50 and 450 mW, which correspond to a pumping rate P between 1 and 9. The theoretical prediction in the case of P = 9 (dashed line) is reported for completeness. (c) and (d) Evolution of the emission peak (c) and FWHM (d) of the spectra displayed in (a) and (b) for varying pumping rate P. The error bars represent the standard deviation of the measurements of emission peak and laser power (c), and the standard deviation in the estimation of the FWHM and laser power (d).

Figure 3.11a presents the experimentally acquired emission spectra at different pumping rates. To match the pumping rate of our calculations, the laser input power was varied from p = 50 to 450 mW. At low powers we observed a broad-band emission around 628 nm, which corresponds to the dye fluorescence. When the pumping rate was higher, in complete agreement with Fig. 3.11a, we observed the spontaneous creation of an optical condensate, which systematically transfers all the available spectral energy at the band-edge frequency state around 590 nm. On comparing the experimental results (Fig. 3.11b, solid green line) with the theoretical prediction (Fig. b, dashed green line) at the largest pumping rate P = 9, we found remarkably good agreement. The properties of the condensation process are further studied in Fig. 3.11c, which shows the experimental (symbols) and theoretical (solid line) behavior of the energy peak for increasing P. Quite remarkably, we observe that the energy peak increases exponentially for a linear increase in P. At the highest input power p = 450 mW, which corresponds to an enhancement rate of P = 9, the emission peak is about 60 times larger than the initial value, showing very good agreement with our statistical model. The dynamics measured in Fig. 3.11c report the signature of a condensation process, which differs from the typical emission of resonant nanoplasmonic structures [74]. In fact, in these resonant structures the emission peak shows an abrupt transition when the pumping rate is increased. In the stimulated emission regime, the peak power increases linearly with P. In Fig. 3.11c, the system response exhibits a smooth nonlinear behaviour. This results from the nature of the condensation process. As seen in Fig. 3.11a,b, all the energy contained in the bandwidth progressively participates to amplify the macroscopic state at the band-edge: a linear increase in the total number of photons, which implies a linear increase in the area of $W(\omega)$, generates a nonlinear increase in the emission peak because the condensation process is obtaining energy from more and more frequencies.

Figure 3.11d, finally, shows the behaviour of the full-width at half maximum (FWHM) of the emission spectrum at different pumping rates P. Theory is quantitatively in good agreement with the experimental outcomes, which show a significant shrinking of the emission linewidth of the system. Deviations in the FWHM between theory and experiment in the central region of the curve are due to the presence of amplified spontaneous emission, or superluminescence [75], of the Rhodamine B used in our measurements.

Fig. 3.18 presents the emission spectra of the dye without nanoparticles, and shows a broad emission with superluminescence at a wavelength of 628 nm. In the experiments shown in Fig. 3.11b, the competition between superluminescence and light condensation is observed in the smooth knee formed around 628 nm in the recorded spectra. The presence of superluminescence is intrinsic to our set-up, where the concentration of nanoparticles is diluted in a much higher volume of dye (each nanoabsorber is dispersed in 6×10^9 dye molecules), and light scatters in a large region of dye before reaching the nanostructures. The presence of superluminescence alters the shape of the emission curve around $\lambda = 628$ nm, affecting the evaluation of FWHM in the central region of Fig. 3.11d. The deviation is minimized at high pumping rates, when the effects of condensation are stronger (Fig. 3.11b, dashed line, and Fig. 3.11d). Fig. 3.19 further analyses the spectral characteristics of the emission peak. This analysis shows that, at the highest pumping power of P = 9, the emission linewidth of the nanoparticles is only 5.6 nm wide, starting from an initial broad emission of $\sim$50 nm bandwidth at P = 1. This corresponds to a 1/9 th-fold reduction of the spectrum. Figure 3.12, finally, compares the effects of light condensation and superluminescence, showing the much stronger emission peak furnished by condensation effects.

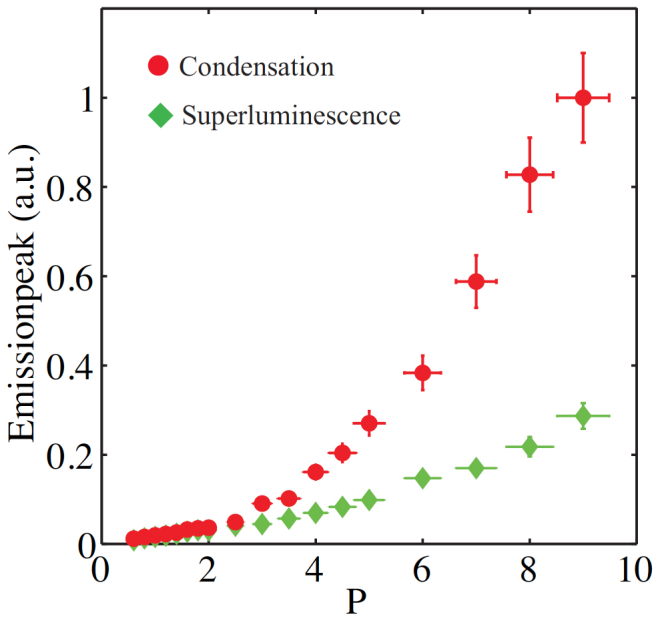

Figure 3.12: Competition between superluminescence and light condensation in the emitted spectra of Fig. 3.11b. Figure shows the behavior of the energy peak emitted through superluminescence (diamond markers) and condensation (circle markers) for a varying pumping rate in the emitted spectra of the dark material. The contribution of superluminescence has been extracted from the expansion of Eq. 3.18, by calculating the amplitude of the corresponding exponential peak emitted at 628 nm.

For nanoparticle concentrations lower than $4C_0$, we still observed the condensation dynamics but with less pronounced effects. This is due to the fact that at lower absorption, the system tends to lose the blackbody character, and electromagnetic energy is not efficiently trapped inside it, requiring a higher pumping power in order to initiate the condensation effect. Using a pumping power of p<450 mW we did not observe condensation effects for a nanoparticle concentration below $2C_0$ (average broadband absorption of 80%). It is worth stressing that the condensation dynamics reported in Fig. 3.11 is unrelated to the Anderson localization of light in strongly scattering dielectrics [76], which is a dynamic of spatial origin that does not show any similarity with the cooperative spectral dynamics of light condensa-

tion observed here.

3.6 Discussion

We have designed and realized nanostructured particles that, even in extremely microscopic quantities, present an almost ideal blackbody absorption performance in the visible and infrared window without requiring normal incidence conditions and/or specific polarizations. The structural darkness of the system is fully tunable over a wide range of absorption values and is observable in extremely thin film structures. In conjunction with an optical amplifier, it spontaneously generates monochromatic emission through a process of light condensation.

Engineered dark nanoparticles are quite interesting in many aspects. They are very versatile, easily dispersed into liquids and easily deposited in solid thin-film structures. By means of light condensation effects they achieve single line emission, such as in classical lasers, but without the use of a cavity, resonance or any special design element. In addition, monochromatic emission is achieved with exponential efficiency by harnessing broadband energy from emission spectra that can, in principle, be arbitrarily large. One interesting possible use of such nanostructures is to harness a wide portion of the solar spectrum and efficiently concentrate it to a single color. This could not only significantly increase the efficiency of photovoltaic technology, but also benefit a large part of available photonic/plasmonic technology for energy harvesting and transmission, which is typically optimized for narrowband excitations.

Another important possibility concerns the photothermal enhancement of energy conversion processes, including thermodynamic solar applications [49]. All these technologies rely on efficiently increasing the temperature of liquids (for example, water) or crystalline solid materials. The broad absorption characteristics observed in the nanoscale pores of our absorbers can have dramatic effects on the temperature increase of a host material, furnishing an ideal system with which to investigate energy-harvesting phenomena.

From a more fundamental perspective, the condensation observed in Fig. 3.11 opens up stimulating perspectives, especially with reference to the Bose-Einstein Condensation (BEC) of light observed in optical microcavities [68]. Although a thorough analysis of this issue goes beyond the scope of this Article, we can highlight some important aspects. In the experiments performed in ref. [68], the authors reported a BEC of light by varying the photon density in a dye material that was maintained in thermal equilibrium inside a microresonator. In our experiments we report condensation dynamics in a dye filled with dark nanoparticles, which do not possess any resonant behavior. As in ref. [68], thermalization is achieved through a complex process involving absorption, scattering and re-emission in the dye material. Both nanoparticles and dye molecules scatter light energy, so both systems can, in principle, contribute to the scattering process. However, the ultrasmall concentration of nanoparticles, their small scattering cross-section in the visible (Fig. 3.15e), as well as their dark nature, suggest that the main scattering player in this set-up is the dye material. The main role of the nanoparticles is to keep radiation inside the system, creating the blackbody condition necessary for light condensation to be observed according to our theory (Section 3.10 Energy condensation). Our experiments illustrate this point very clearly, showing the existence of a minimum darkness threshold (80%, as stated in the previous section) for experimentally observing light condensation in our set-up. This scenario is so far unexplored in active materials and can open new fundamental connections between the BEC of light and nanoplasmonics.

3.7 First principle simulations of light -matter interaction in a single nanoabsorber

In order to complement the ray optics picture provided in the main text, we here present the results of full first principle simulations on the light matter interaction with a single nanoabsorber. We begin by considering an enlarged portion of the structure represented in Fig. 3.1b left of the main text, and simulate by FDTD the dynamics of light in the presence of a radiating dipole placed in the axis origin $(x\prime, y\prime) = (0, 0)$. In the transformed geometry of Fig. 3.1b right, this point corresponds to the infinity point and simulates an external source placed far away from the nanostructure. As expected on the basis of ray analysis, light bounces into the structure and get coupled into the metallic waveguides in terms of Surface Plasmon Polariton (SPP) waves [77], which exists at the metallo dielectric interface (Fig. 3.13a) and are butt-coupled inside the channels. In the geometry of Fig. 3.13a, light propagates in the waveguide channels without never reaching the end, which occurs at infinity.

In the transformed geometry of Fig. 3.1 right, this illusion is provided by an adiabatic compression of the waveguide modes (Fig.3.13b-c). This originated from the contraction of the space generated by the coordinate transformation: while electromagnetic energy tends to propagate towards the kissing point K (corresponding to infinity in Fig. 3.13a), the velocity of the electromagnetic energy is progressively reduced in Fig. 3.13b-c, eventually reaching the point K in an infinite time. This mechanism allows light to be efficiently absorbed in an extremely narrow spatial region where the electromagnetic energy is accumulated (Fig. 3.13c). Figures 3.13d-e, finally, report the absorption σ_a and scattering σ_s cross section of a single nanoabsorber, comparing it to the response of a nanosphere (blue dots) and a nanorod (green dots). Calculations have been made by using finite element simula-

tions with COMSOL mutliphysics software. The absorption cross section of a single nanostructure, as expected on the basis of our theory, shows almost flat absorption over the visible and near infrared. The absorption of the nanosphere is, in general, orders of magnitude higher than the one of a nanorod and a nanosphere, except in the region between 400 nm and 500 nm where the nanosphere exhibits its nanoplasmonic resonance and the two structures have comparable cross section.

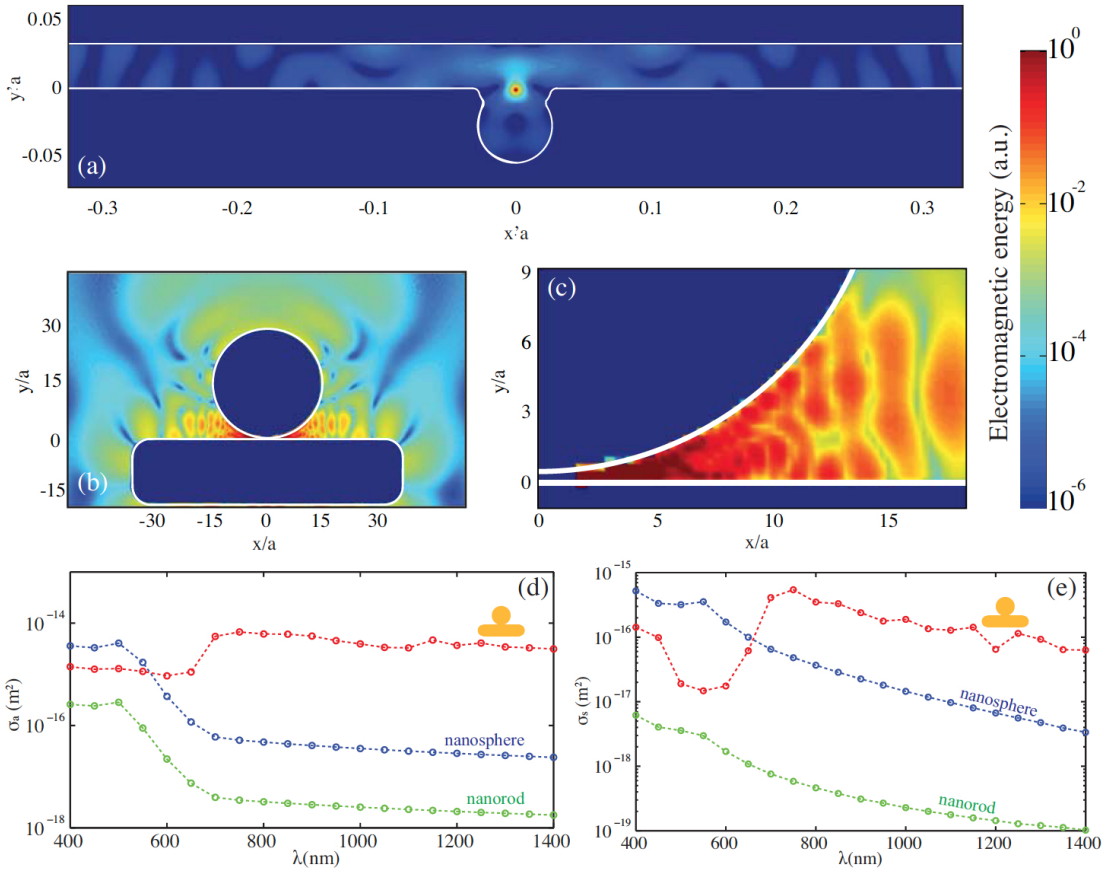

Figure 3.13: Light-matter interaction with a single nanoabsorber: firstprinciple results. Panel (a-b) report the FDTD calculated electromagnetic energy distribution of (a) the structure of Fig. 3.1b left and (b) the transformed structure represented in Fig. 3.1b right of the main text. Panel (c) provides a zoomed detail of the area around the kissing point region in Panel (b). In the simulation, we used a radiating dipole placed at infinity in the geometry of Panel (b). The dipole location in the transformed space of Panel (a) corresponds to the axes origin $(x', y') = (0, 0)$. Due to the scaling invariance of Maxwell equations, we use dimensionless spatial units defined with reference to the scaling constant a. Panel (e)-(d), finally, reports the absorption σ_a (d) and scattering σ_s (e) cross section, calculated by finite element simulations using the COMSOL multiphysics software.

3.8 Thermal stability of the nanostructures

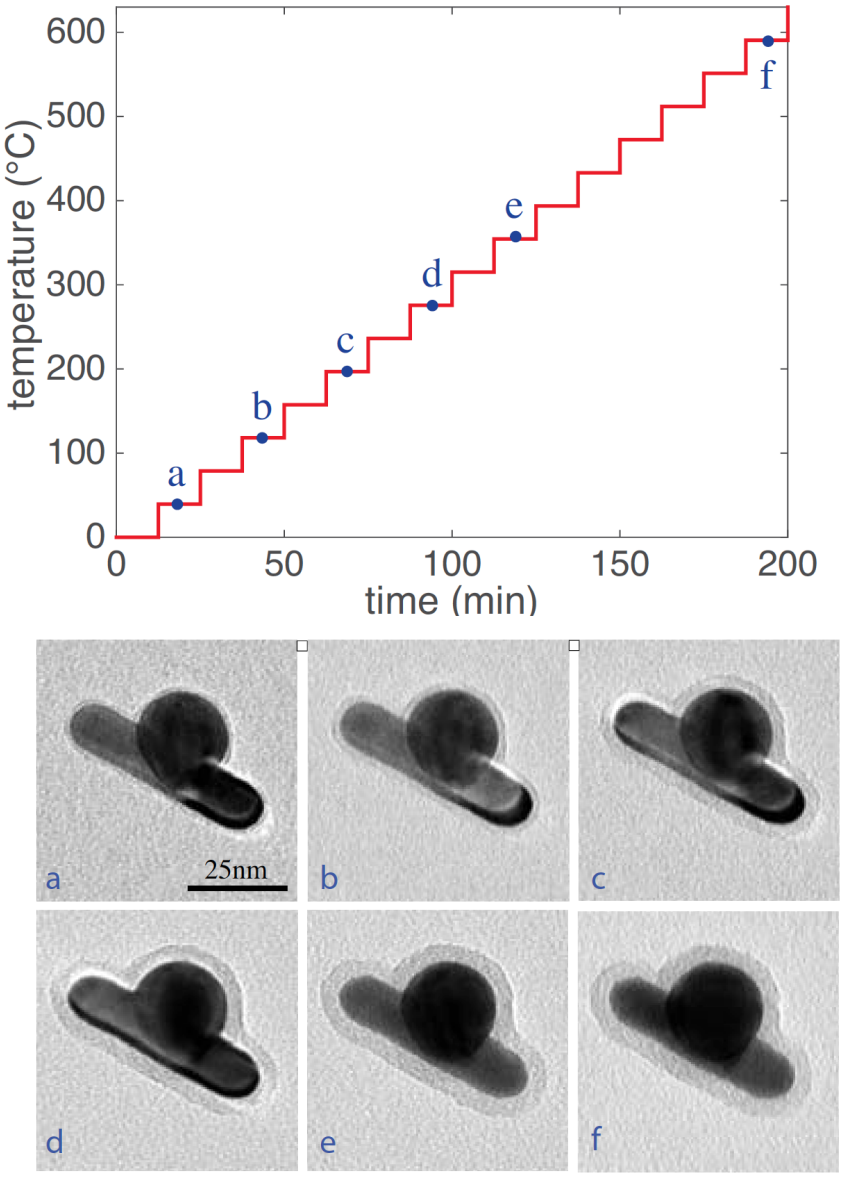

Figure 3.14: Stability of the nanoparticles versus temperature: in-situ TEM results. Left panel reports the temperature increase of the nanoparticles, measured from room temperature, with associated TEM snapshots (a-f panels on the right) of the same nanoparticle at different times.

The metallic bonding between the nanosphere and the nanorod gives to our nanoparticles excellent thermal stability properties, as we illustrate in this section. In a first

series of experiments, we monitor the stability of the nanoparticles subjected to an increasing temperature. Fig. 3.14 illustrates the results, obtained during 200 minutes where the nanoparticles temperature is increased from room temperature to T = 600^{o}C (Fig. 3.14, left panel). This measurement has been performed in-situ of the TEM imaging facility, by depositing the nanoparticles over the standard TEM grid and collecting TEM snapshots of the same nanostructure at different temperatures. The results (Fig. 3.14a-f) show that the system is completely stable and unaffected by the temperature increase. The amorphous material surrounding the particles and visible in Fig. 3.14 is carbon contaminant, which accumulated on the particles during the heating process. In a second series of experiments, we deposited the nanoparticles on the TEM grid and subjected them to a prolonged solar illumination (Fig. 3.15). This experiment is realized by using a Newport 91160-1000 solar simulator, which generates an intensity of 2KW/m^2. TEM images acquired before (Fig. 3.15a) and after 10 hours of solar illumination (Fig. 3.15b) show that the nanoparticles are perfectly stable and do not suffer from any apparent deformation. Fig. 3.16 reports the dynamics of the absorption spectra of the nanoparticles at different temperatures. The experiments were performed by heating the nanoparticles deposited by spin-coating over a planar sample, and then measuring the nanoparticles absorption at every 50^{o}C temperature increase after reaching the temperature of 150^{o}C degrees. The absorption spectra appears quite stable: at 150^{o}C, 200^{o}C and 250^{o}C degrees, the average absorption variation is 0.4%, 0.7% and 0.8%.

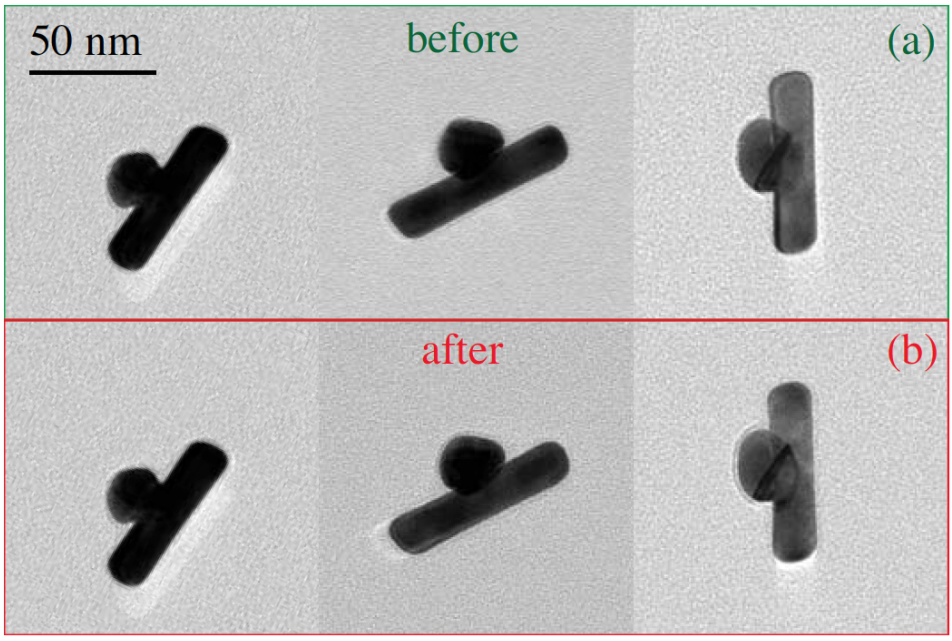

Figure 3.15: TEM images of nanoparticles after prolonged solar illumination. Panel a reports TEM images of selected nanoparticles at the beginning of the experiment, prior to the illumination. Panel b reports TEM images of the nanoparticles image after 10 hours of solar illumination, obtained by exposing the nanoparticles to a solar simulator generating the intensity of 2kW/m^2.

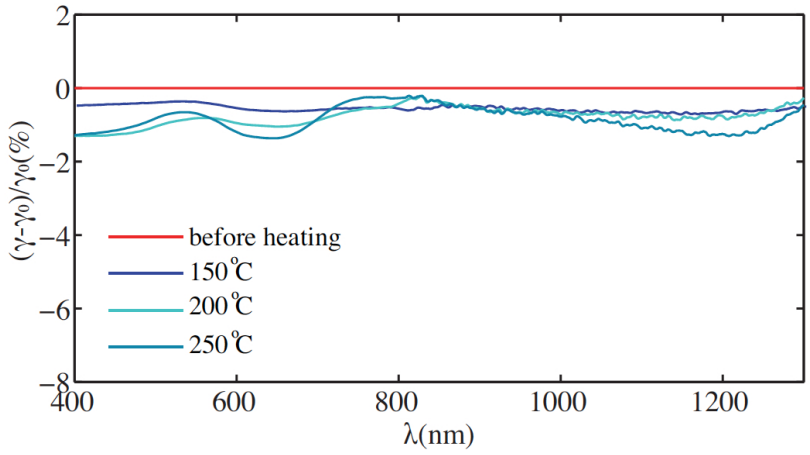

Figure 3.16: Nanoparticles absorption spectra versus temperature. The figure reports the variation $\Delta\gamma 0 = (\gamma - \gamma_0)/\gamma_0$ of nanoparticles absorption γ versus temperature, being γ_0 the nanoparticles absorption spectrum at room temperature. The temperature curve used is the same of Fig. 3.14a.

3.9 Spectrophotometer measurements

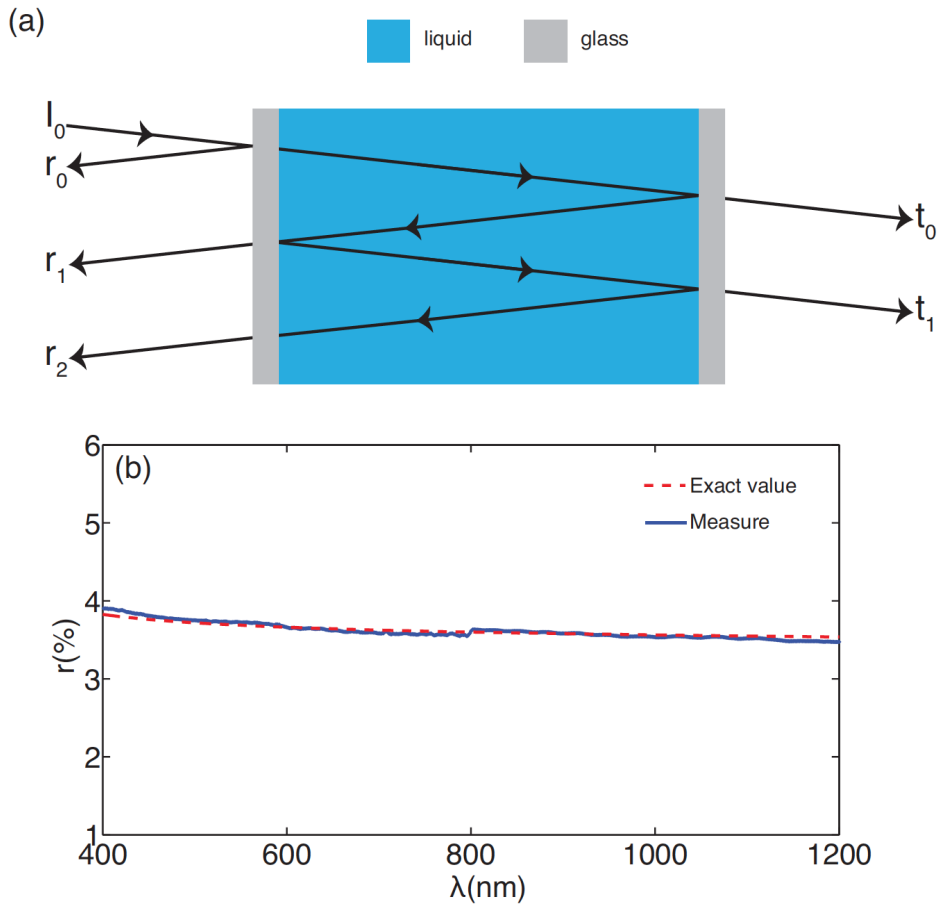

Figure 3.17: Calibration measurement of the UV-VIS-NIR spectrometer. (a) Multiple reflections model for analyzing light propagation in the glass cuvette sample. Panel (b) reports the reflectivity r measured from the transmission T_w and absorption A_w of a sample composed by a glass cuvette filled up with water, for normal incidence illumination. The solid red line represent our experimental measure, the solid blue line illustrates the exact result calculated by using Fresnel formulae and the refractive indices of glass and water available in the literature.

All absorption measurements were carried out using a CARY 5000 UV-VIS-NIR spectrophotometer equipped with an integrating sphere. Absorption was calculated as $100\% - T - R$, being T and R the energy transmission and reflection respec-

tively. The 100% transmission baseline measurement was an empty sphere. The absorption of the nanoparticles in the liquid solution is estimated by using standard arguments from elementary wave theory. Fig. 3.17a illustrates the dynamics of light when impinging on a sample composed by a glass cuvette with a liquid inside. Each glass side of the cuvette is characterized by one input air/glass and output glass/water interface. In order to simplify the analysis, we group together these two interfaces into a single air/glass/water interface element. For a liquid composed only by water, light of intensity I0 is initially reflected by the first interface air/-glass/water and generate the first component $r_0 = I_0 r$, being r the reflectivity of the air/glass/water interface element. The transmitted energy $I_0(1-r)$ propagates into water, reaching the output air/glass/water interface as $I_0(1-r)\alpha$, being $\alpha \in [0,1]$ the attenuation of water, with $1-\alpha$ the water absorption. Light transmitted at the output air/glass/water interface generates the first contribution to the transmissivity $t_0 = I_0(1-r)^2\alpha$, as well as a series of multiple reflections/transmissions in the sample, whose components can be straightforwardly found by iterating the propagation algorithm described above. Total reflectivity R_w, transmissivity T_w and absorption $A_w = 1 - T_w - R_w$ are expressed as follows:

$$\begin{cases} T_w = \sum_n \frac{t_n}{I_0} = \frac{(1-r^2)\alpha}{1-r^2\alpha^2} \\ R_w = \sum_n \frac{r_n}{I_0} = r(1+T_w\alpha) \\ A_w = \frac{(r-1)(1-\alpha)}{r\alpha-1} \end{cases} \tag{3.2}$$

When a second attenuating specie such as our nanoparticles is diluted in the liquid at an ultra small concentration, Eq. 3.2 hold with $\alpha \rightarrow \alpha \cdot \beta$, being $1-\beta \equiv \gamma$ the absorption of the nanoparticles. From the total absorption of the sample $A = (r-1)(1-\alpha\beta)/(r\alpha\beta-1)$, we can easily obtain the nanoparticles absorption γ by

direct inversion:

$$\gamma = 1 - \frac{A + r - 1}{\alpha(Ar + r - 1)} \tag{3.3}$$

Quantities r and α appearing in Eq. 3.3 are directly measured in our setup from the transmission T_w and absorption A_w of a water sample through Eq. 3.2. Once these quantities are measured, the nanoparticles absorption is obtained after an absorption measurement A through Eq. 3.3. To evaluate the accuracy of our setup, we provided a calibration experiment by reporting the spectrum of λ as measured from a water sample made by a glass cuvette filled with water. We considered normal incident condition. We compare the experimentally retrieved result to the exact value obtained from the transfer matrix equations of a multilayer structure composed by air/glass/water planar interfaces. For glass and water, we used optical constants estimated independently from us and available in the literature [78, 79]. Figure 3.17 b illustrates the results. The figure shows an excellent matching, with the largest difference between the exact result and the measured one of only 0.6%, showing the great accuracy of our setup. When deposited in the planar film structure, the nanoparticles absorption An is directly evaluated from the absorption $A_n = 100\% - R - T$ of the whole sample. 100% transmission baseline is an empty sphere.

3.10 Energy condensation

In this section we build a statistical model of a blackbody in the presence of a suitable gain material, and study at leading order the main emission properties of the system at thermodynamic equilibrium. Following the classical approach in the analysis of the blackbody spectrum [54], we use a quantum statistical mechanics framework that does not rely explicitly to the microscopic details of the system, but try to predict the main physical outcomes from general and universal perspectives. Our analysis begins by considering a cubical volume V , with side L, sufficiently large to completely include the blackbody material inside it. The electromagnetic details of the blackbody are defined by an inhomogeneous dielectric response $\epsilon(\mathbf{r}, \omega)$, defined inside V , which depends on both space $\mathbf{r}$ and frequency ω. In our case, the dielectric response function σdescribes the random spatial configuration of nanostructures that compose our material. Without loss of generality, due to the structure of our nano-absorbers and their nanoscale length, we can perform the calculations by assuming an ideal conductor with real ϵfunction. In the volume region defined by V , we can quantize the electromagnetic field by following the scattering method. This approach is introduced and thoroughly described in [80], hence, we here limit to present the main results, remanding to Ref. [80] for all the demonstrations. The scattering approach begins by expanding the vector potential A of Maxwell equations into a set of plane waves:

$$\mathbf{A}((r), t) = \sum_k \mathbf{e}_k \frac{\hat{Q}_k}{\sqrt{(V)}} e^{i(\mathbf{kr} - \omega_k t)} \tag{3.4}$$

being $\mathbf{e}_k$ a unit polarization vector of the k-th plane wave possessing wavevector $\mathbf{k}$ and frequency ω_k, while $\hat{Q}_k$ is is the corresponding position operator. The plane waves form a continuum set of modes, where for each frequency ω_k the wavevector $\mathbf{k}$ can be displaced in all possible spatial directions.

By introducing standard creation $\hat{a}_k^\dagger$ and annihilation $\hat{a}_k$ operators from the expansion $\hat{Q}_k = \sqrt{\hbar/2\omega_k}(\hat{a}_k^\dagger + \hat{a}_k)$, the scattering approach expresses the Hamiltonian $\hat{\mathcal{H}}$ of Maxwell equations in the compact nondiagonal form:

$$\hat{\mathcal{H}} = \sum_{kk'} J_{kk'} \hat{a}_k^\dagger \hat{a}_{k'} \tag{3.5}$$

described by a coupling matrix $\mathbf{J}$ characterised by symmetric couplings $J_{kk'} = J_{kk'}^\star$ defined as follows:

$$J_{kk'} = \hbar\omega_k \delta_{kk'} + \frac{\hbar\sqrt{\omega_k \omega_{k'}}}{4V} e_k^\star e_{k'} \int \frac{\chi}{\epsilon} e^{i\Delta_{kk'}\mathbf{r}} dV \tag{3.6}$$

having introduced the shorthands $\chi(\mathbf{r}) = 1 - \epsilon(\mathbf{r})$, $\Delta_{kk'} = k - k'$ and being $\delta_{kk'}$ the Kronecker delta function. Equations 3.5 and 3.6, despite the lengthy expression of 3.6 furnish a very intuitive physical scheme of light matter interaction. In the absence of nanostructures, $\epsilon = 1$, $\chi = 0$ and $J_{kk'} = \hbar\omega_k \delta_{kk'}$. In this condition, the energy Hamiltonian $\hat{\mathcal{H}} = \sum_{kk'} \hbar\omega_k \hat{a}_k^\dagger \hat{a}_{k'}$ becomes simply expressed by the sum of non-interacting elements. When a generic material is inserted into V, conversely, $\epsilon \neq 1$ and plane-waves become coupled by the non diagonal terms $J_{kk'}$ for $k \neq k'$. In our case, the coupling coefficients are fully random, due to the inhomogeneous dielectric constant $\epsilon(\mathbf{r})$ that models random distributions of nanostructures. The net effect of disorder is therefore to create a source of random couplings among the different modes that characterize photons propagation at every frequency and polarization. In the absence of gain, each plane wave described by $\hat{a}_k^\dagger$ and $\hat{a}_k$ k fluctuates around a stationary configuration of thermal equilibrium. When a suitable gain material (such as a dye or a more general optical amplifier) is inserted into the volume V and is optically pumped, the equilibrium configuration of the system is changed. While the optical pumping introduces new photons in the volume, the light-matter processes of spontaneous and stimulated emission alter their distributions by e.g.,

depleting the number of photons at some frequency and creating photons at other wavelengths. The effects of this dynamics are observed at every frequency, owing to the nonzero couplings $J_{kk'}$ among all the modes that describe light propagation. The complexity of this interaction makes a statistical treatment the most convenient choice to derive an effective model that can capture the main physical outcomes. From a statistical perspective, if the the spatio-temporal evolution of the photons dynamics is sufficiently long, the system has enough time to explore the available phase-space and find a new equilibrium state. This is described by a new average value of photon intensity, or equivalently, a new average photon number:

$$\sum_k \langle \hat{a}_k^\dagger \hat{a}_k \rangle = N\bar{n} \tag{3.7}$$

being $\langle ... \rangle$ a quantum statistical mechanics average, $\hat{a}_k^\dagger \hat{a}_k$ the photon number operator for the k-th mode, N the total number of photons in the volume V and $\bar{n}$ the average number of photons contained in a single mode. Equations 3.5 and 3.6, with the constraint defined by 3.7, completely specify our problem from a statistical mechanics perspective. They are very simple and general, describing an ensemble of interacting modes (Eq. 3.7) This model is very general and its predictions are not limited to the nanoparticle system considered in this work, but to any blackbody material where the number of photons is maintained at steady-state. At leading order in the dynamics of 3.5 and 3.6, we do not need to keep into account nonlinear interactions among the modes; as we will illustrate in the following, in fact, Eqs. 3.5 and 3.6 are already sufficient to predict the system dynamics and match very well our experimental results.

By generalizing the Langevin approach found in [81], it is also possible to demonstrate that the thermodynamic state characterized by an effective temperature is indeed the stationary state of the system of Eqs. 3.4 to 3.5. This analysis requires long and involved mathematics that goes beyond the scope of this paper and will

be presented elsewhere. The statistical analysis of Eqs. 3.5 and 3.6 can be performed in closed form, and we here present the principal results.

To solve for the associated thermodynamics, we add a Lagrange multiplier l to Eq. 3.5 and define a new Hamiltonian:

$$\hat{\mathcal{H}} = \sum_{kk'} J_{kk'} \hat{a}_k^\dagger \hat{a}_{k'} - \hbar l \sum_k \hat{a}_k^\dagger \hat{a}_k \tag{3.8}$$

The variable guarantees that the condition Eq. 3.7 is fulfilled during the dynamical evolution of Eq. 3.8. The partition function $\mathcal{Z}$ can be easily found by diagonalising the coupling matrix $\mathbf{J}$ and reads:

$$\mathcal{Z} = \mathrm{tr}\left(e^{-\beta\mathcal{H}}\right) = \prod_k \frac{1}{2\sinh\frac{\beta\hbar(\omega_k - l)}{2}} \tag{3.9}$$

being tr the trace operator, $\beta = 1/T$ with T an effective temperature, and Ω_k corresponding to the eigenvalues of the coupling matrix $\mathbf{J}$. The variables Ω_k represent a new set of frequencies, which are associated to the normal modes of the coupling matrix. The parameter T can be regarded as an effective temperature, which describes the configuration of thermodynamic equilibrium of the system. Once the partition function is known, we can calculate the Free Energy $\mathcal{F}$:

$$\mathcal{F} = -\frac{\log\mathcal{Z}}{\beta} = \frac{1}{\beta}\sum_k \log\left[2\sinh\frac{\beta\hbar(\Omega_k - l)}{2}\right] \tag{3.10}$$

By combining Eq. 3.10 with the expression obtained from the derivative of the Free Energy $\partial\mathcal{F}/\partial l = -\hbar\sum_k\langle\hat{b}_k^\dagger\hat{b}_k\rangle$, we can express the condition of Eq. 3.7:

$$\sum_k \frac{1}{2N}\coth\left[\frac{\beta\hbar(l - \Omega_k)}{2}\right] = \bar{n} \tag{3.11}$$

Equation 3.11 furnishes the state equation and allows to identify the various phases of the system. It is important to highlight a fundamental scaling law of the state

Eq. 3.11, which can be easily illustrated in the classical limit $\hbar \to 0$, which yields:

$$\sum_k \frac{1}{N} \frac{1}{\beta\hbar(l - \Omega_k)} = \bar{n} \tag{3.12}$$

Equation 3.12 is invariant with respect to the following scaling $\beta \to \beta \cdot \alpha$ and $\bar{n} \to \bar{n} \cdot \alpha$, for an arbitrary dimensionless α constant. It is therefore convenient to describe the state of the system with respect to a dimensionless pumping rate $P = \bar{n}/\alpha$, defined by the ratio between the average photon number carried by each mode and an arbitrary reference value α. Without loss of generality, we use $\alpha = 1/\hbar$, which simplifies the resulting expressions. Due to the continuum nature of the plane wave set used in all our expansions, is convenient to express the state equation the continuum limit, where $\Omega_k \to \omega$:

$$\frac{1}{2} \int p(\omega) \coth \left[\beta \frac{(l - \omega)}{2} \right] d\omega = P \tag{3.13}$$

with $p(\omega)$ representing the probability density distribution of the frequency eigenvalues ω of the coupling matrix $\mathbf{J}$. Without loss of generality, we can assume normally distributed couplings $J_{kk'}$. In this situation, the eigenvalue density $p(\omega)$ is expressed from the universal distribution of random matrices [82]:

$$p(\omega) = \frac{1}{2\pi\sigma^2} \sqrt{\sigma^2 - \omega^2} \tag{3.14}$$

The distribution in Eq. 3.14 is nonzero in $\omega \in [-2\sigma, 2\sigma]$, with $2\sigma \equiv \Delta\omega$ defining the total bandwidth of the plane-wave modes where Eq.3.7 is defined. The substitution of Eq. 3.14 into Eq. 3.13 furnishes a self-consistent equation of state for the Lagrangian multiplier l, which can be solved for a given pumping rate P and inverse temperature β. For any given values of P and β, the parameter decreases for increasing P until it reaches a critical value $l_c = \Delta\omega$, which determines a phase transition of the system. A further increase of P creates a condensed state, where

all the modes constructively buildup energy into the edge state at $\omega = \Delta\omega$, which becomes macroscopically dominant:

$$\frac{\hat{a}^{\dagger}_{\Delta\omega}\hat{a}_{\Delta\omega}}{N} = \left[1 - \frac{\beta_c(P)}{\beta}\right] \tag{3.15}$$

being $\beta_c(P)$ the inverse transition temperature defined by:

$$\frac{1}{2}\int p(\omega)\coth\left[\beta_c\frac{(\Delta\omega - \omega)}{2}\right]d\omega = P \tag{3.16}$$

The dynamics of this physical process can be observed from the emission spectrum of the system, obtained by equating Eq. 3.11 with the condition 3.7 written in the continuum limit, which yields the expression for the mean number of photon contained in each mode and in each frequency ω. The latter furnishes the energy density spectrum $W(\omega)$ of the system, measured in units of $\hbar\omega$, as a function of the self-consistent parameter l:

$$W(\omega) = \frac{\sqrt{\Delta\omega^2 - \omega^2}}{\pi\Delta\omega^2}\coth\left[\beta\frac{l - \omega}{2}\right] \tag{3.17}$$

When we increase the photon number rate P in the frequency bandwidth $\Delta\omega$, the inverse critical temperature β_c obtained from Eq. 3.16 becomes smaller and smaller, forcing the system to enter into a condensed phase regardless of its initial state (i.e., initial β and P). This result is particularly interesting, as it predicts the possibility of observing such light condensation at every regime, provided that the optical pumping is sufficiently large to start the process.

3.11 Competition between superluminescence and light condensation effects

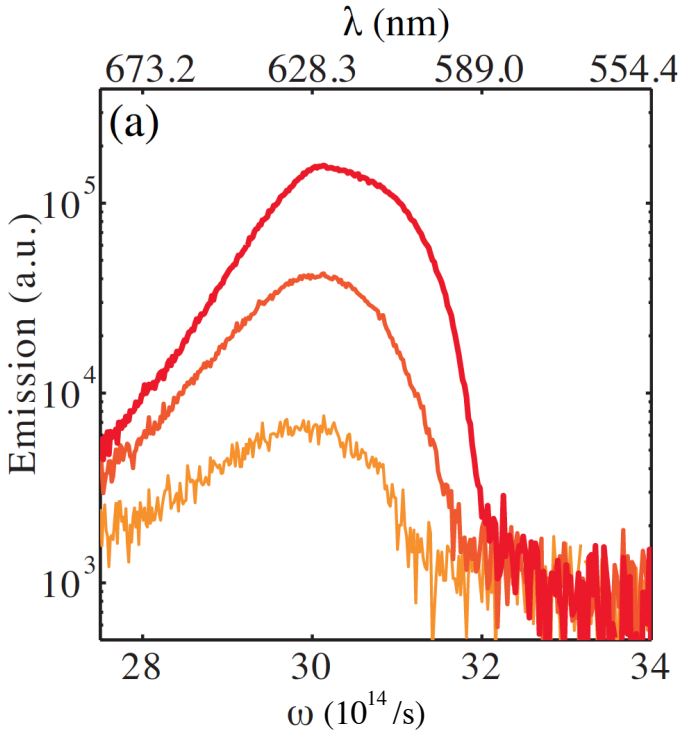

Figure 3.18: Dye emission for increasing pumping rates. Figure shows the dye emission spectra for increasing pumping rates P (from the bottom spectrum to the top: P = 1, P = 4, P = 7) in the same experimental conditions but without nanostructures.

To analyze the condensation process in more detail, we fit each emission spectra $W(\omega)$ with a series of Gaussian lineshaped functions:

$$W(\omega) = \sum_n a_n e^{-\frac{(\omega-\omega_n)^2}{\delta\omega_n^2/2}} \tag{3.18}$$

being a_n, ω_n and $\delta\omega_n$ the amplitude, central frequency and linewidth, respectively, of each gaussian function of the expansion.

Gaussian functions are quite robust, and well fit localized function profiles such as

the spectral emissions illustrated in Fig. 3.11b. Fig. 3.18a illustrates the distribution of linewidths $\delta\omega_n$ at different pumping rates P. In the plot, we scaled each linewidth $\delta\omega_n$ contribution with the corresponding amplitude an in the expansion 3.18. The figure provides a clear view of the dynamics, showing a very strong condensation process that, from an initial broad linewidth of $\simeq$50 nm, generates a final emission line that is only 5.6 nm wide. This correspond to a 9th-fold reduction of the spectral linewidth. As a further validation of these results, and in order to clearly show the fundamental role of our nanostructures in sustaining light condensation effects, we performed experiments by employing a solution of Rhodamine B with no nanostructures. Fig. 3.18b shows the distribution of linewidths $\delta\omega_n$ for the case of a pure solution of Rhodamine B, pumped with the same rate of Fig. 3.18a. In the absence of nanostructures, energy emission remains with broad spectral features, showing modes with approximatively 40 nm linewidth. Fig. 3.19 provides the emission spectra of the dye. For increasing pumping rates P, the dye tends to acquire a more asymmetric shape around the central emitted frequency at 628 nm, which identifies the superluminescence emission frequency of the dye. In order to quantitively study the competition among condensation and superluminescence, we extracted the latter contribution from the amplitude an of the gaussian function centred at 628 nm in the expansion 3.18 of the spectra of Fig. 3.11b. Fig. 3.12 reports the behavior of the energy peak of superluminescence for increasing pumping rate P. The contribution arising from light condensation at band-edge is reported for completeness. Despite the extremely small amount of nanostructures, the process of light condensation is extremely effective, showing a significant increase with respect to the much smaller variation due to superluminescence effects.

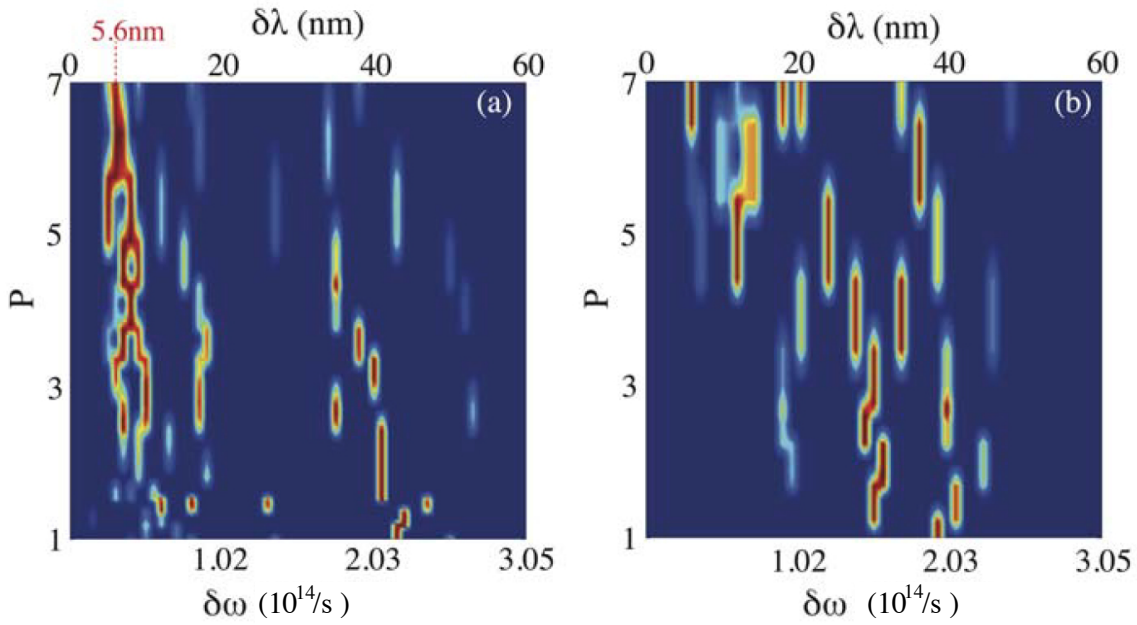

Figure 3.19: Analysis of the linewidth of emission spectra. Panel (a) reports the distribution of linewidths $\delta\omega_n$ of the experimental spectra $W(\omega)$ of Fig. 3.11b for a varying pumping rate. The analysis is performed by decomposing each $W(\omega)$ through Eq. 3.18, which encompasses n = 1, ...,N localised exponential functions each defined by an amplitude an and a linewdith $\delta\omega_n$. In panel (a), each contribution $\delta\omega_n$ is displayed with a colour that is proportional to the corresponding amplitude an in the expansion. Panel b shows the same type of analysis in the case of a pure solution of Rhodamine B.

Chapter 4

TRIGGERING EXTREME EVENTS AT THE NANOSCALE IN PHOTONIC SEAS

4.1 Energy localization and Rogue waves

The extreme localization of waves, either in space or in time, has always been a subject of great interest in science. Subwavelength manipulation of light has driven a large body of research in metamaterials and plasmonics, where metallic nanostructures and negative index materials have been investigated to achieve energy compression, ultrahigh efficiency photovoltaics and superlens effects [83, 84, 85, 86, 87, 88, 89, 90]. Nanofocusing of light has also stimulated new concepts in subwavelength imaging [91, 92], including the use of disorder with spatial light modulators to trap photons beyond the diffraction limit [93, 94]. The study of electromagnetic confinement on short temporal scales, conversely, is at the frontier of research in ultrafast optics, where it ultimately led to the development of advanced refocusing techniques and single-cycle laser sources [95, 96, 97]. Even though this body of research spans across very different areas, they are all characterized by the use of

deterministic effects and predictable events, which require the development of challenging fabrication processes, sophisticated experimental apparatus and/or elaborate wavefront reshaping techniques.

On the other hand, extreme localization of energy naturally arises in rare events such as hurricanes, rogue waves and tsunami, which seem to appear at once and then disappear again. Apart from their catastrophic nature, these phenomena are not normally exploited owing to their unpredictability, which makes it difficult to understand their physics and control their emergence. Among various types of rare dynamics, rogue waves are particularly interesting. Rogue Waves (RWs) are isolated events in wave motion that are characterized by the appearance of localized waveforms with exceptional amplitude. These events seem to be ubiquitous and have been reported in a large number of systems sharing diverse degrees of randomness, noise, unpredictability, linear and nonlinear responses [98, 99, 100, 101, 102, 103, 104, 105, 106, 107, 14, 108, 109]. A key issue is the active role of randomness [108, 109], and the question whether RW can be observed in fully deterministic structures with no intrinsic disorder. Deterministic systems are more easily controlled, they can provide a simpler platform for studying the physics of these phenomena, and they can challenge us with an intriguing problem: can we embed the exceptional amount of energy of a rogue wave into a simple integrated structure? And if this structure can be engineered, what are the specific limits that we can break with the unique properties of these events? The ubiquitous character of RW manifested in uniform media, such as water, and not relying on any particular geometry has the potential to open a new paradigm where extreme events are not only investigated for their elusive physics, but can also be the source of inspiration for unconventional light management techniques.

In this chapter, we report the combined ultrafast (163 fs long) and subwavelength (206nm wide) localization of photons at a wavelength λ=1.55 μm by exploiting a

new mechanism for the generation of rare events akin to rogue waves, which also allows one to gain new fundamental insights into the properties of these phenomena. Our system is a two-dimensional Photonic Crystal (PhC) resonator, integrated onto a chip, whose shape has been suitably engineered in a quarter-stadium form. This particular shape has been chosen to allow the generation of an incoherent wave ensemble through the mechanism of wave chaos [110]. Even though the material exhibits no nonlinearity, the stadium shape supports chaotic motion for light rays, and fully randomizes any input wavefront into an ensemble of strongly incoherent waves. In our system, suitably engineered losses trigger a mechanism of spontaneous synchronization, which constructively builds up energy into giant nanostructures of light. The experimental set-up is complemented by a home-built Near-Field Scanning optical Microscope (NSOM) [111], which allows us to measure both the amplitude and phase of light with nanometre and femtosecond accuracy.

4.2 Theoretical model: superposition of random plane waves

We begin our analysis by investigating the generation of localized rare events from an incoherent sea of random waves $\psi(\mathbf{r}, t)$:

$$\psi(\mathbf{r}, t) = \int a(\mathbf{k}, \omega) e^{i[\omega t - \mathbf{k}\cdot\mathbf{r} + \phi(\mathbf{k},\omega)]} d\omega d\mathbf{k} \tag{4.1}$$

with $a(\mathbf{k}, \omega)$ and $\phi(\mathbf{k}, \omega)$ random random amplitudes and phases, respectively, depending on the wavevector $\mathbf{k}$ and frequency ω and ϕ are distributed uniformly. Equation 4.1 describes a classical random walk whose intensity probability density $P(I) = P(|\psi|^2)$ follows a Rayleigh law $P(I) = \exp(-I)$ as confirmed in Fig. 4.1a. This case was simulated with an ensemble of 2000 random waves with amplitudes $a(\mathbf{k})$ uniformly distributed in [0, 1], with randomly displaced wavevectors $|k| < \pi/\lambda$ and and uniformly distributed frequencie $\omega \in [1, 2]$. For these conditions, no rare event of large intensity is generated (Fig. 4.1b). If we apply a suitably small perturbation to the system, however, we observe a radically different scenario. Figure 4.1c,d illustrates what happens when the phase probability distribution is diluted by, for example, a range of inaccessible values for ϕ(Fig. 4.1c inset). We observe an anomalous deviation from the Rayleigh law and the appearance of a rare event (Fig. 4.1c circlemarkers). The deviation fromthe Rayleigh law shown in Fig. 4.1c has a characteristic "L" shape with a long tail, which is the hallmark for the appearance of rogue waves (Fig. 4.1d). Considering the small magnitude of the perturbation $\delta\phi = \pi/10$, the generation of rare events of strong amplitude ($\simeq 60\%$ higher than the Rayleigh limit) is quite remarkable.

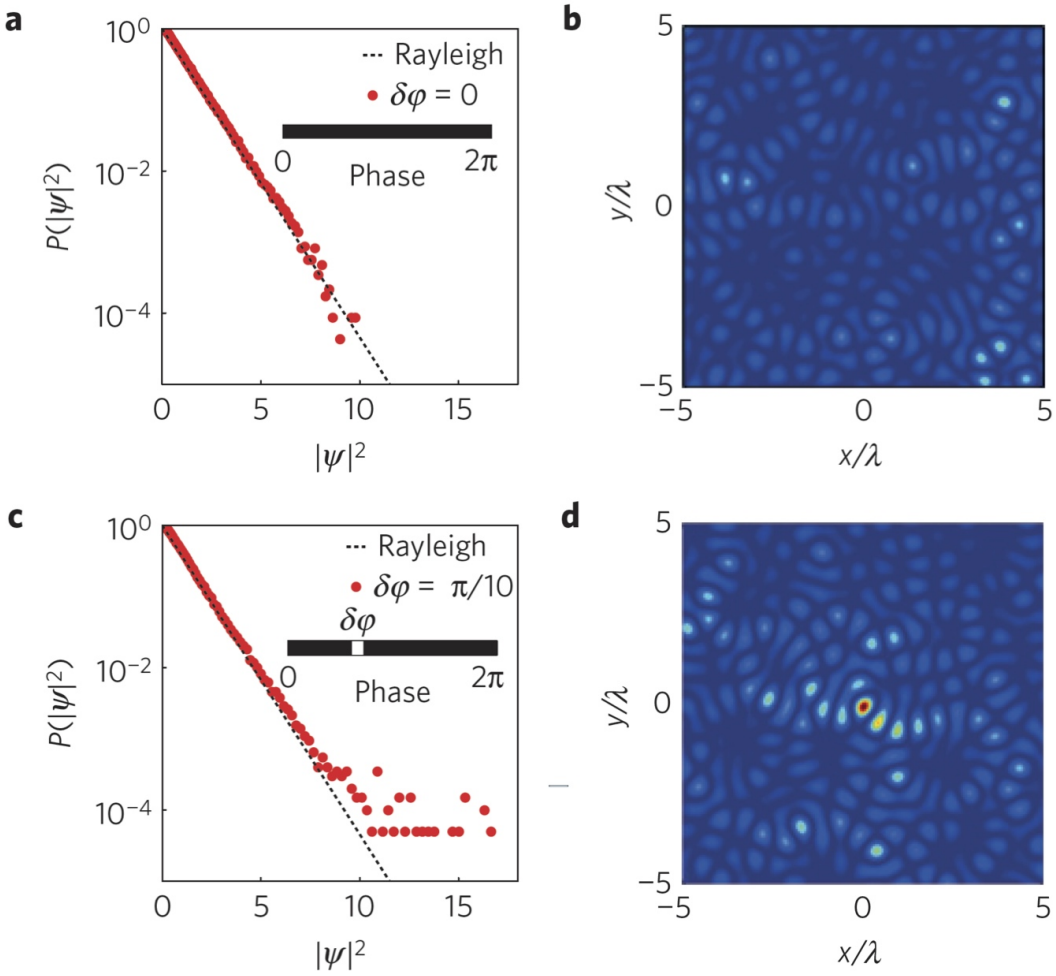

Figure 4.1: Classical and diluted random walks of photons. Intensity probability density (a,c) and spatial wave pattern at t=0 (b,d) generated by an ensemble of 2000 random waves with uniformly (a,b) and diluted (c,d) phase distribution. Dilution is realized by inserting a small gap $\delta\phi = \pi/10$ of inaccessible values in the probability distribution of ϕ(c, inset). By comparing (b) and (d), we observe the spontaneous formation of a rogue wave in the chaotic light pattern. In all simulations, we consider a randomly displaced wavevector k in the plane and uniformly distributed amplitudes $a \in [0, 1]$ and frequencies $\omega \in [1, 2]$.

The generation of rare events can be intuitively explained by using the idea of path cancellation. In a classical random walk, the point of maximum intensity I_n is observed with the lowest probability density $P(I_n) = e^{-I_n}$. The value I_n can be obtained by different combinations of random waves; however, there exists at least

one situation where I_n is generated from a set of waves that destructively interfere, whose phase is randomly distributed in a region of width δ, and all the remaining waves that constructively interfere. This event is, by definition, rare and observed at one (or very few) spatial point, which we label p. When we make the gap δ inaccessible, the field evolution shows the same paths as the case with no dilution, minus all the paths originated by waves with phase in the gap δ. The removal of these paths now enable at p the appearance of a rare event where all the waves constructively interfere, or equivalently, are synchronized. The intensity generated in p is now larger than the Rayleigh limit I_n, owing to the removal of the components that were interfering destructively. Such a rare event can be expressed as follows:

$$\psi(\mathbf{r},t) = \int a_0 \exp\left[i(\omega t - \mathbf{k}\cdot\mathbf{r} + \phi_0)\right] d\omega d\mathbf{k} \tag{4.2}$$

with ϕ_0 a generic constant value. Equation 4.2 can be regarded as a spontaneous synchronization of statistical origin. When such a synchronization involves all the frequency bandwidth $\Delta\omega$of the field, the spectral energy contained at each frequency $\omega \in \Delta\omega$ is constructively summed up and the resulting intensity reaches the largest possible value for that particular field. Notably, equation 4.2 embeds a super-oscillatory [112] nature that beats the diffraction limit even when only diffraction-limtted components are allowed to interfere. In particular, if we consider a buildup process where all the possible components $k = |\mathbf{k}| < 2\pi/\lambda$ are summed up, by integrating eq. 4.2 we obtain:

$$\psi(\mathbf{r},t) \propto J_0(k|\mathbf{k}|)\frac{\sin\left(\frac{\delta\omega}{2}t\right)}{t} \tag{4.3}$$

with $\delta\omega$ the frequency bandwidth where equation 4.2 holds. Equation 4.3, in intensity, exhibits a subwavelength spatial fullwidth at half-maximum (FWHM) that is 25% smaller than the diffraction limit $\lambda/2$, and a time FWHM of $\tau = 2\pi/\delta\omega$. Sub-

wavelength confinement originates from the Bessel wave $J_0(kr)$, which is able to oscillate faster than its band limited Fourier components owing to super-oscillations. Super-oscillations have been largely investigated for the realization of superlenses [91], although super-resolution usually comes at the expense of side lobes that can be several orders of magnitude higher than the subwavelength spot. The rogue wave nature of our rare event, conversely, always guarantees that super-oscillatory behaviors are observed as bright energy spots with small sidelobes, offering a natural pathway towards overcoming this problem. The brightness of the energy spot depends on the spectral bandwidth $\delta\omega$ of the waves that get synchronized: the larger the bandwidth, the larger the energy peak of the rogue wave.

4.3 System Design based on FDTD simulations

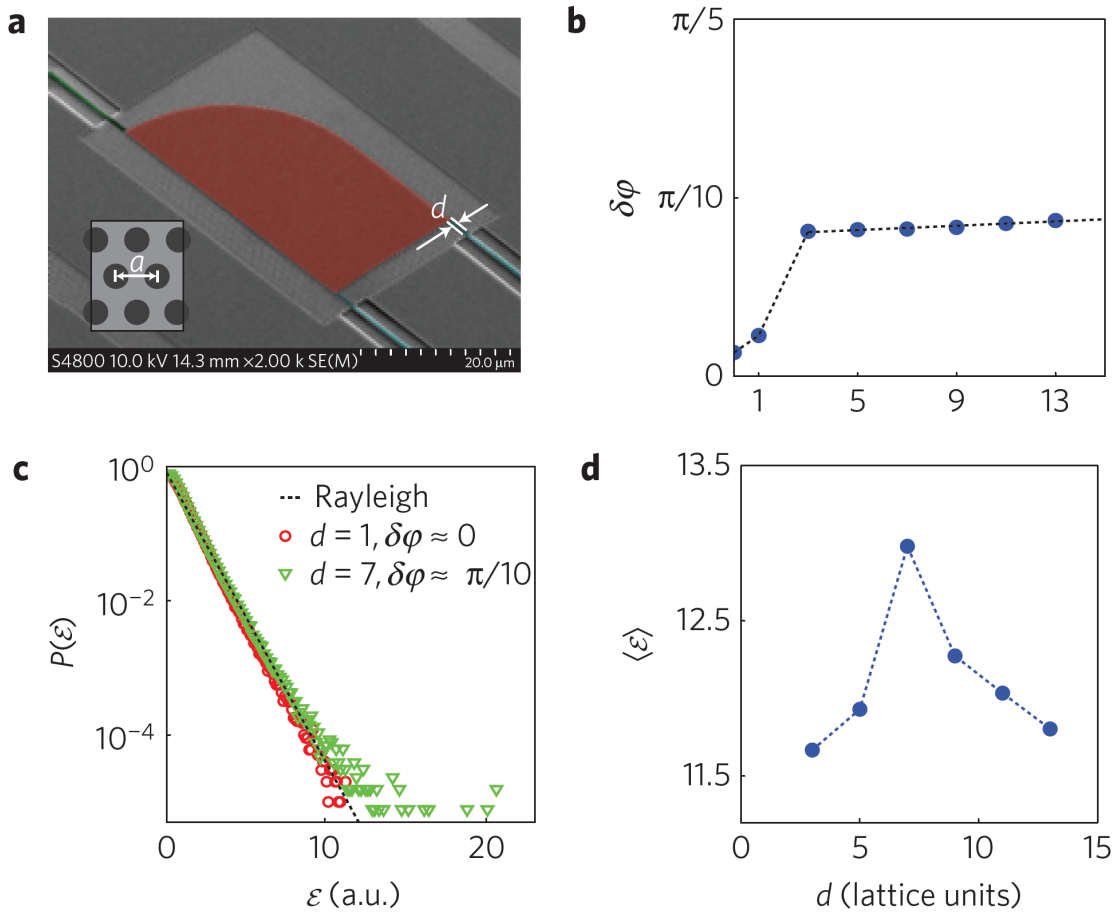

Figure 4.2: Photonic crystal resonator. Design and FDTD simulations. a, SEM image of the structure with the resonator area highlighted in false color. (b) Largest gap, $\delta\phi$, in the phase probability density versus waveguide spacing d. (c) Probability distribution of the electromagnetic energy density, $\langle\mathcal{E}\rangle$, for $d = 1$ (circle markers), d=7 (triangle markers) and a classical random walk process (dashed line). (d) Order parameter, $\eta = \langle\mathcal{E}\rangle$, versus d.

To illustrate the generation of ultrafast, sub-λ rogue waves in an integrated structure, we design two-dimensional PhC optical cavities with losses controlled by the width of the output channels (Fig. 4.2a). Light of a frequency within the bandgap of the photonic crystal can escape from the system only via the input/output channels, otherwise being reflected at the resonator boundaries. Wave chaos [110] fully

randomizes light reflections at the resonator boundaries and generates a "photonic sea" of incoherent waves, where diffraction-limited contributions are continuously mixed up. To intuitively understand the effect of the waveguide channels, we use the same idea of path cancellation introduced previously. When outgoing channels are absent, light rays cannot escape the system and continuously mix up, generating a classical random walk with phases randomly distributed in the whole interval [0,2π]. Such a phase distribution results from the sum of all the paths of light rays in the closed cavity. In the presence of outgoing channels, conversely, a fraction of rays escape from the system and deplete the dynamics from their corresponding paths.

The cancellation of these paths inhibits the random walk from exploring the full set of phases, and is expected to create a gap in the phase distribution for sufficiently large values of d that is, when a sufficiently large number of paths are cancelled. The relationship between the phase gap $\delta\phi$ and the output waveguide width d, however, is far from trivial, and we assess it via massively parallel finite difference time domain (FDTD) simulations with our code NANOCPP (ref. [63]). To ensure a high accuracy, we employed a high resolution of 40 points per internal wavelength.To model a realistic case,we consider the propagation of a supercontinuum source with wavelengths in $\lambda \in [1.535, 1.565]\mu$m, (that is, 30nm bandwidth centered at $\lambda_0 = 1.55\mu$m, launched at the input waveguide of the PhC cavity. By applying the Prony algorithm (see Methods), we extracted the probability distribution of the electromagnetic field amplitude and phase, calculating the size of the largest phase gap $\delta\phi$ (Fig. 4.2b) and the electromagnetic energy (Fig. 4.2c) for different output channel widths d. The waveguide spacing d is varied by removing an integer number of rows from the photonic crystal lattice. As seen in Fig. 4.2b, a variation of d creates a phase gap $\delta\phi$ with a nonlinear relationship. For $d = 3$, a small gap of approximately $\delta\phi = \pi/10$ opens up, which slowly increases in size for larger d. To

investigate the most favorable condition for the observation of these phenomena, we first calculate the average energy density $\eta = \langle \mathcal{E} \rangle$:

$$\eta = \langle \mathcal{E} \rangle = \int \mathcal{E}' P(\mathcal{E}') d\mathcal{E}' \tag{4.4}$$

with $P(\mathcal{E}')$t he probability distribution of the electromagnetic energy density in the system. The average density $\eta$of equation 4.4 can be used to measure the largest deviation from the Rayleigh law, and therefore acts as an order parameter for the observation of rogue waves in the structure. Figure 4.2d reports the behavior of η versus waveguide spacing d, showing a maximum around $d = 7$. In this regime, rare events (Fig. 4.2c triangle markers) of energy twice as high as the Rayleigh limit (Fig. 4.2c circle markers) are observed. The behavior of η versus d shown in Fig. 4.2d highlights the competition between a larger gap in phase space due to the increase of d (see Fig. 4.2b) and the reduction of the chaotic strength of the cavity resulting from the presence of larger output waveguides. This aspect is further illustrated by a set of classical billiard simulations (see Section 4.9 for more details). Figure 4.3 summarizes our FDTD results in the optimal case d=7, showing the spatial distribution of the electromagnetic energy density inside the cavity when an isolated rogue wave is formed simultaneously in both space (Fig. 4.3a-c) and time (Fig. 4.3d,e). To quantitatively demonstrate that the observed rare events belong to the class of rogue waves, other than the anomalous deviation from the exponential shown in Fig. 4.2c,d, we also calculate the Significant Wave Height (SWH). The latter is defined as the average of the highest one-third of the waves nearby and represents a widely accepted parameter for the identification of rogue waves. As discussed in ref. [113], rogue waves are characterized by a maximum peak that is at least twice as large as the SWH. This threshold criterion has been initially introduced in hydrodynamics, and is therefore formulated with reference to the wave amplitude. We comply to the original formulation and measure the SWH with ref-

erence to the electromagnetic wave amplitude, which is a parameter accessible from our FDTD simulations. The spatial hot spot shown in Fig. 3 meets this criterion, as its electromagnetic field is 2.51 times higher in space and 2.20 times higher in time than its SWH. The subwavelength nature of the rogue wave is readily evaluated by applying equation 4.3 (Fig. 4.3c dashed line), showing a perfect agreement with the result of FDTD (Fig. 4.3c solid line). The time evolution of the rogue wave exhibits a FWHM of approximatively 250 fs, which matches well with equation 4.3 by using the full input pulse bandwidth $\delta\lambda = \lambda_0^2\delta\omega/2\pi c = 30nm$ (Fig. 4.3e), with c the speed of light. Quite remarkably, this means that such rogue waves are constructively accessing the spectral energy contained in the whole frequency bandwidth of the field. This also identifies the maximum value in Fig. 4.2 as the maximum energy that can be extracted for the given input bandwidth of 30 nm.

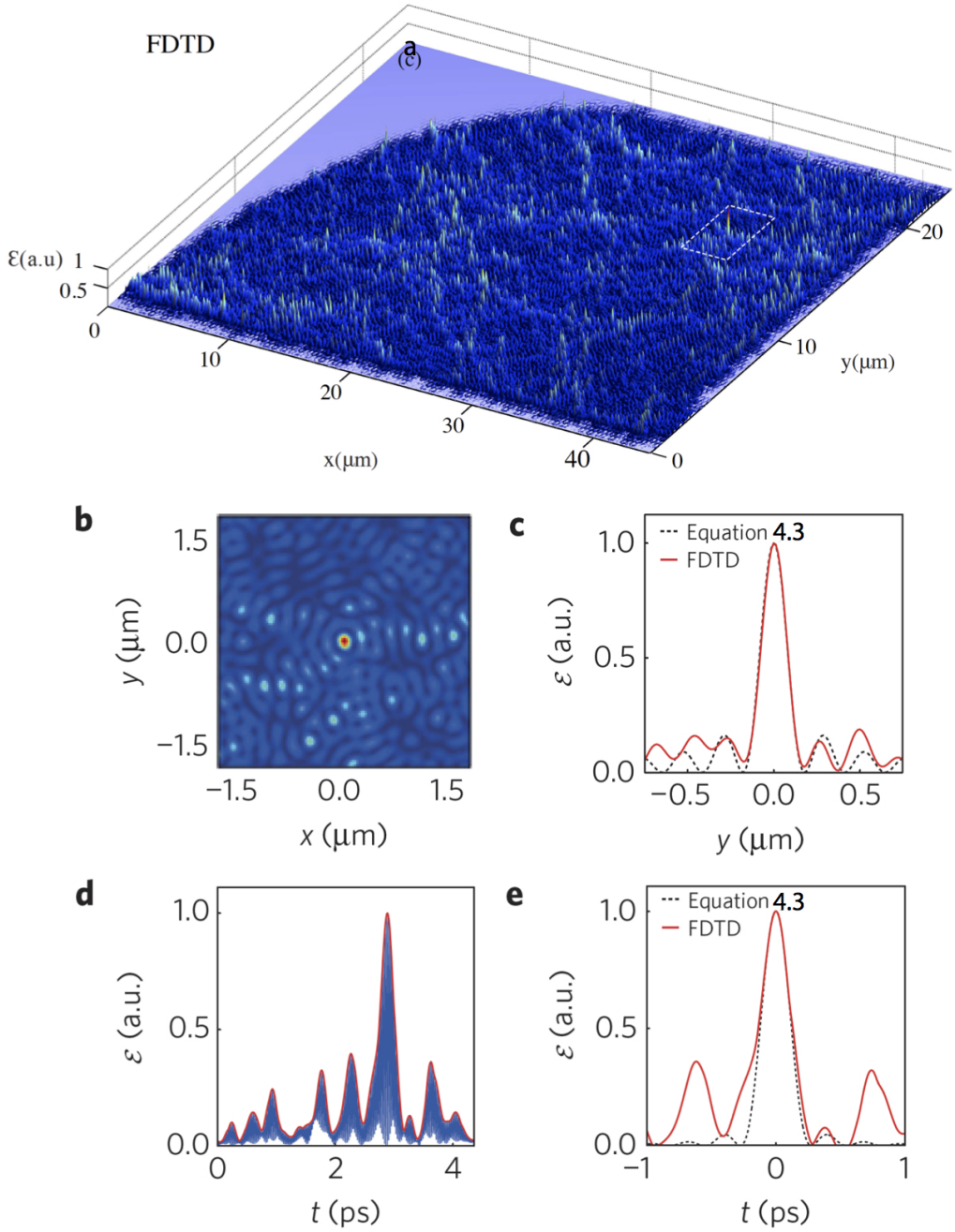

Figure 4.3: FDTD analysis of ultrafast subwavelength light localization (a) Electromagnetic energy distribution in the cavity in the presence of an extremely localized rogue wave. (b) Zoomed detail on the RW energy peak in the area indicated by the dashed rectangle in (a). (c) Section of the energy distribution along y (solid line) and the theoretical prediction based on our random wave model (dashed line). (d) Temporal dynamics of the RW spatial energy peak. (e) Detailed dynamics of d (solid line) with the corresponding theoretical prediction (dashed line). In b,c and e, the axis origin is centered with respect to the intensity maximum of the rogue wave.

4.4 PhC sample fabrication

We now set out to observe nanoscale RWs on our chips.We begin by fabricating a series of silicon-on-insulator planar photonic crystal cavities with output couplers of different widths. The fabrication of optical resonators is realized by a silicon-on-insulator substrate consisting of a 220-nm-thick silicon layer on a 2-μm-thick layer of SiO_2. The patterns were written using ZEP resist with a modified LEO/RAITH electron-beam lithography system with a 2nm step size, then etched with a balanced blend of SF_6 and CHF_3 gases in a reactive ion etching step. After stripping off the residual resist, the sample was cleaved for end-fire coupling [39].

4.5 FDTD experiements

In our experiments, we launch 1550 nm, 150 fs light pulses into these resonators and image the electromagnetic field with an NSOM (see Methods for more details). In similar fashion to the FDTD analysis, we experimentally recorded the RW dynamics only after the light pulse has been inside the cavity for a sufficient long time to generate a photonic sea. Figure 4.4 a-c summarizes the statistical analysis of light dynamics inside the optical resonator, providing a quantitative comparison between theory and experimental NSOM results.

Figure 4.4a considers the case for d=1, comparing the classical random walk condition from NSOM measurements (triangle markers) and equation 4.7 (dashed line), which represents the analytical estimate (see Methods). Considering the rare nature of the phenomenon under study, the agreement between theory and experiments is quite remarkable. Figure 4.4b then compares the experimental retrieved energy distribution in the optimal case d=7 for the observation of RWs (circle markers) with the theoretical predictions of FDTD simulations (triangle markers) and our random wave model described by equation 4.1 (diamond markers). Fig. 4.5 illustrates each of the latter contributions NSOM, FDTD and predictions from equation (1) separately, to better appreciate the high level of agreement between experiments and theory. Figure 4.4a,b also demonstrates the high level of control offered by our integrated chips in the generation of these events.

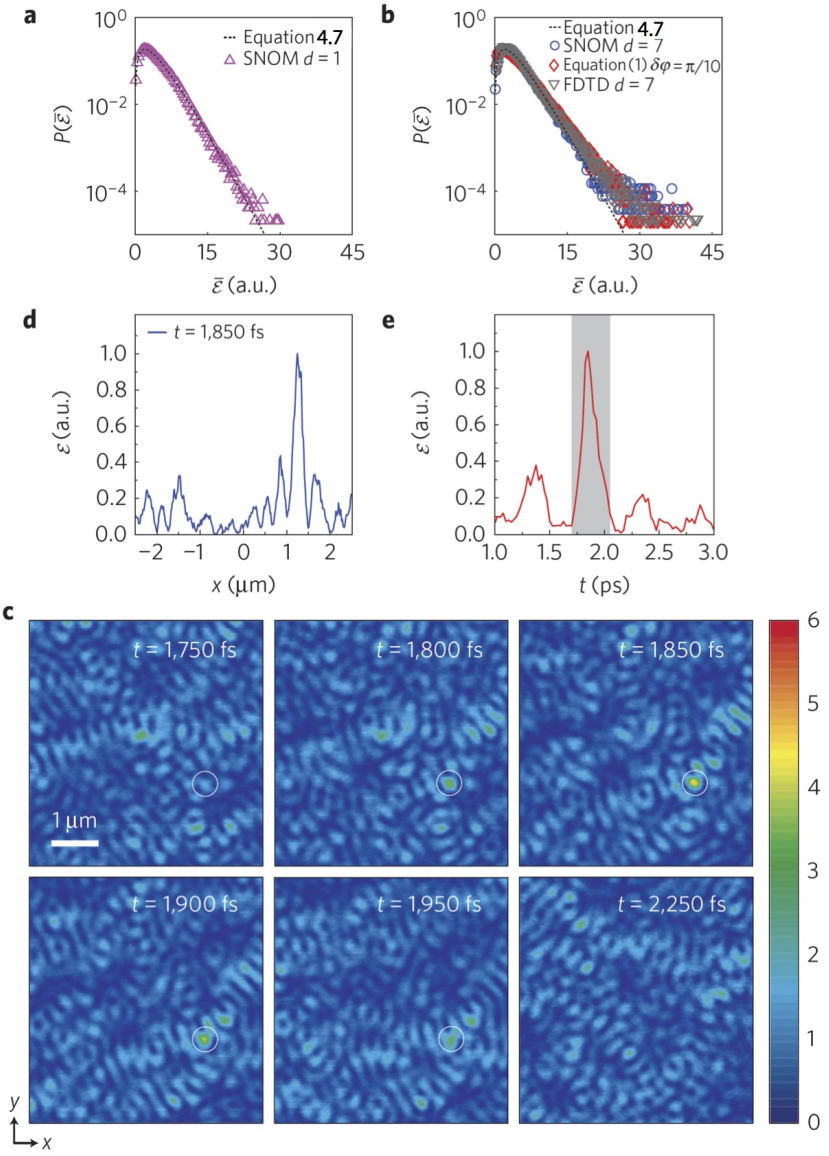

Figure 4.4: Summary of NSOM experimental results and comparison with theory. (a) Comparison of the time-averaged energy probability density, $P(\bar{\mathcal{E}})$, retrieved from NSOM experiments for d-1 (triangle markers). (b) Comparison of FDTD results (triangle markers) and NSOM experiments for the case of d=7 (circle markers), with Eq. 4.1 for $\delta\phi = \pi/10$ (diamond markers). In both panels, the probability law dependence of the classical random walk (dashed line) is also shown for reference. (c) Time evolution of the electromagnetic energy density when a nanoscale rogue wave settles in. (d) Section of the energy distribution along x when the rogue wave exhibits the maximum intensity. (e) Temporal dynamics of the rogue wave energy peak. In (c) the color bar on the right indicates the values of the electromagnetic energy density, which are normalized with respect to the significant wave height of the field intensity (SWHI).

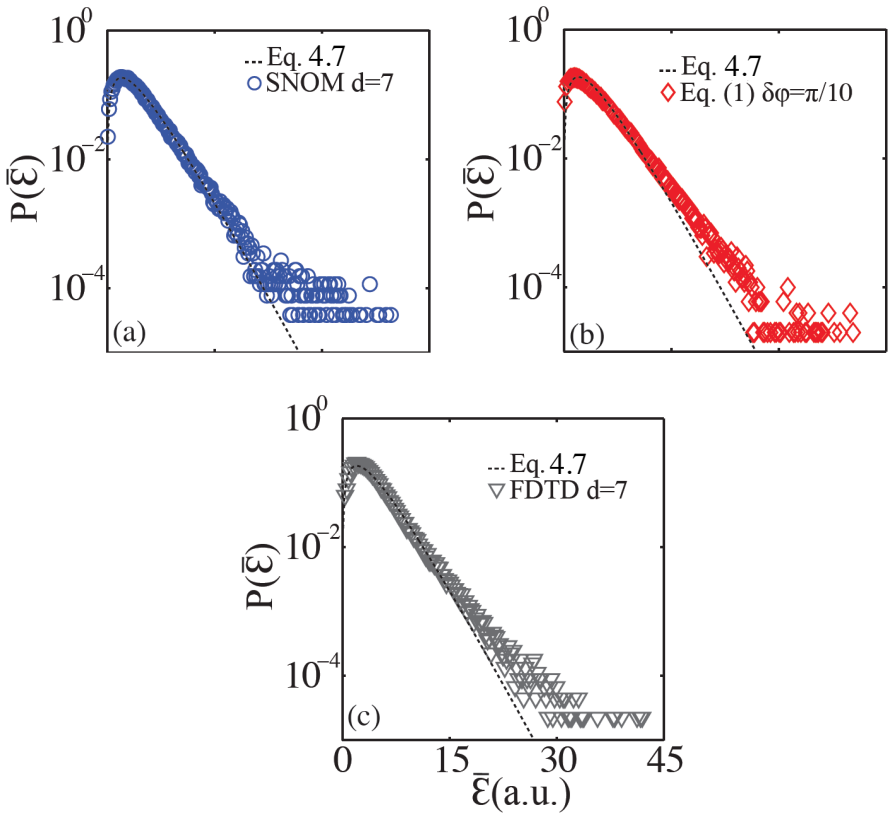

Figure 4.5: Details of Fig .4.4b. (a) shows (circle markers) the time average energy probability density $P(\bar{\mathcal{E}})$ retrieved from NSOM experiment in the case of $d = 7$. (b) reports (diamond markers) the prediction of $P(\bar{\mathcal{E}})$ from the random wave model encompassed by Eq. 4.1 with a phase gap $\delta\phi = \pi/10$. (c) displays (triangle markers) the calculation of $P(\bar{\mathcal{E}})$ from FDTD simulations with $d = 7$.All panels report for completeness the probability law dependence of the classical random walk(dashedline)

.

Figure 4.4c shows a photo sequence of the spatial distribution of the electromagnetic energy when an ultrafast subwavelength rogue wave is formed by spontaneous synchronization. The intensity distributions along x (Fig. 4.4d) and in time (Fig. 4.4e) match well with our FDTD predictions (Fig. 4.3c-e). In Fig. 4.4c,we normalized the field energy with respect to the SWH calculated from the field intensity, which we called SWHI to distinguish it from the SWH previously calculated from the field amplitude. The peak intensity of the rogue wave formed in Fig. 4.4c is

six times larger than its SWHI. To further provide a quantitative comparison with our FDTD simulations, we also we measured the SWH with reference to the field amplitude, which is accessible in each NSOM experiment. Our rogue waves exhibit a field peak amplitude that is 2.41 times higher than their SWH in space and 2.1 times higher in time, in full agreement with our FDTD predictions. Experimentally generated rogue waves exhibit a subwavelength spatial FWHM of 206 nm, which is 25% smaller than $\lambda/2n = 287$ nm(with n=2.7 the three-dimensional effective index of the guidedmodes inside the cavity). The temporal FWHM extension of the rogue wave, conversely, is 163 fs and corresponds to a bandwidth of $\delta\lambda = 49$nm, which matches the full electromagnetic field bandwidth ($\approx$50 nm). As further proof of the reproducibility of our results,we added a second NSOM image (Fig. 4.6) showing the formation of an ultrafast subwavelength rogue wave appearing at a different spatio-temporal position.

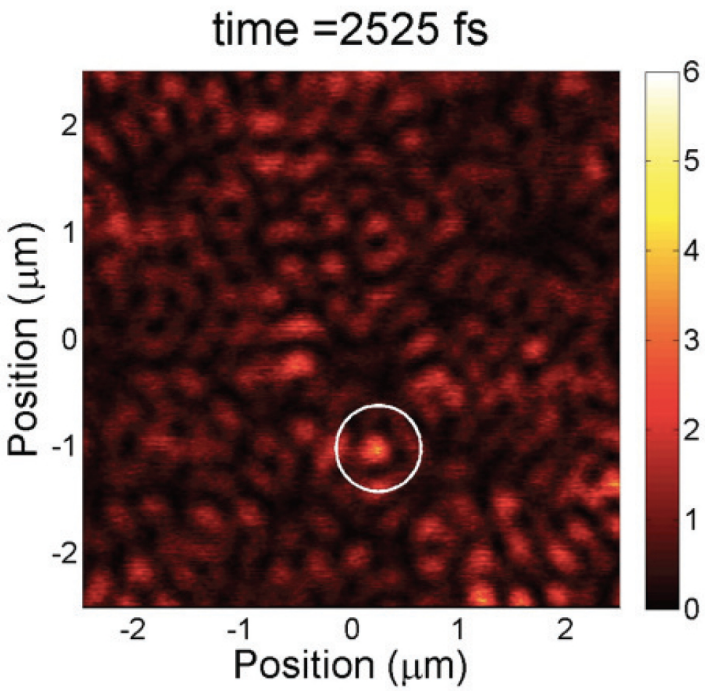

Figure 4.6: NSOM experimental results showing the spatial distribution of electromagnetic energy density of a rogue wave appearing in a different position of the sample and at a different time. The energy amplitude (colorbar) is normalized with respect to the significant wave height SWHI of the rogue wave intensity.

4.6 Discussion

We have proposed and demonstrated a simple integrated platform that generates ultrafast rare events, which exploit the spectral energy of the full frequency bandwidth of an incoherent field to build up nanostructures of light with giant intensity. Our analytical model, FDTD simulations and experimental observations agree extremely well, showing that the statistics of these ultrashort subwavelength structures can be generated on demand, including their spatio-temporal shape.

Our chaotic resonators open up new possibilities, both in fundamental and applied science. Compared with nanoplasmonic structures, they also achieve subwavelength localization, but without using tapered metal nanostructures, specific nanoantenna designs or lossymaterials. Furthermore, they do not require the use of coherent fields, and the appearance of localized energy spots is not limited to the near field. In our experiments we observe rogue waves whose mutual distance is ≈ 50 μm, which corresponds $\approx$120 wavelengths in Si and is far beyond the near-field distance of nanoplasmonic hot energy spots. Compared with other methods for generating subdiffraction-limited light using randomness, no sophisticated spatial light modulator system is required. In the above-mentioned cases (plasmonic structures and random systems), evanescent contributions beyond the diffraction cutoff are generated. The use of rare events provides an alternative approach, where diffraction-limited components are exploited in very simple dielectrics.

We can identify many applications that may benefit from such an extreme light-matter interaction, where their appearance is not constrained to any specific position but conversely requires a large intensity and a given distribution. These range from extremely sensitive spectrometers based on speckle[114], to new sensing apparatus based on random light patterns randomly displaced in two dimensions [115], low-threshold lasers sustained by randomly localized electromagnetic modes [64], and new energy-harvesting devices relying on chaotic light motion [63].

An important aspect concerns the suppression of detrimental or destructive manifestations of rogue waves, which other than the open sea [116] seem to be relevant also in high-speed data communication [117]. Our results shown in Fig. 4.2d open an interesting question whether or not RW can be completely eliminated by either increasing chaos or the system losses, which can stimulate interesting work in both nonlinear optics and hydrodynamics. The interplay between nonlinearity and spontaneous waves synchronization is also an issue of of fundamental interest. A thorough investigation on this topic is clearly beyond the scope of this work; however, some interesting points can be highlighted. In the present work we exploit the mechanism of wave chaos to randomize the dynamics of electromagnetic waves in phase controlled conditions, which are settled by specific waveguide channels. Extremely localized rare events then emerge from a totally incoherent field, where the phases are fully delocalized between 0 and 2π. This opens up a new interesting panorama as compared with nonlinear dynamics, where rogue waves have been predicted to appear only if the incoherence of the system is small enough [107]. Another very intriguing point is related to what can happen if such a random ensemble evolves into a cavity with a fully nonlinear response. The non-trivial interplay between spontaneous synchronization and classical Kerr nonlinearities [106] can furnish important new results in the study of rare events in physics.

4.7 Phase Gap analysis

In our FDTD simulations, we calculate the time evolution of the electromagnetic field at each point of the spatial grid inside the cavity, and decompose it using the Prony algorithm. Given a time-varying function $s(t)$, the Prony analysis can be considered as a natural extension of the Fourier transform, allowing the decomposition of the signal $s(t)$ into a series of damped complex exponentials:

$$s(t) = \sum_{j=1}^{N} A_j e^{\left(i\omega_j - \frac{1}{\tau_j}\right)t + i\phi_j} \tag{4.5}$$

where the amplitude A_j, frequency ω_j, phase ϕ_j and lifetime τ_j of each frequency component of the signal are directly calculated. The extraction of these coefficients requires the inversion of an N by N matrix, whose lengthy expression can be found in refs [118, 37] and Chapter 1. In our code, the Prony extraction is computed in parallel and at each instant of the simulation, furnishing the evolution of all the coefficients A_j, ω_j, ϕ_j and τ_j during time. The latter express the distribution of amplitudes and phases of the electromagnetic field at each spatial point, and allow a calculation of the corresponding probability density distributions.

4.8 Near-field scanning optical microscopy and corresponding intensity statistics

To image the light-field distributions inside the chaotic resonators we use a home-built NSOM, whose operation is described in detail in refs [111, 119] Briefly, an aperture probe consisting of an aluminium-coated tapered SiO_2 fiber with a 100-300nm sized aperture is placed at a distance of 20nm from the surface, within the evanescent tail of the electromagnetic field inside the cavity. This aperture converts a small fraction of the near-field radiation to far-field radiation that is transported through the fiber to a detector, and by raster scanning the probe across the cavity we can construct a two-dimensional map of the electromagnetic field inside the cavity. To detect this inherently weak signal we use a heterodyne detection scheme where the microscope is placed in one branch of a Mach-Zehnder interferometer and interfere the signal from the probe with a reference pulse. This approach both amplifies our signal and, by placing and scanning a delay line in one of the branches, it also allows us to obtain temporal information. NSOM experiments measure both real $R_j(\mathbf{r})$ and imaginary $C_j(\mathbf{r})$ components of the electromagnetic field in the complex representation $E_j(\mathbf{r}) = R_j + iC_j(\mathrm{i} = \mathrm{x}, \mathrm{y})$. The field intensity $\mathcal{I}$ obtained from NSOM experiments is expressed as follows:

$$\mathcal{I} = R_x^2 + R_y^2 + C_x^2 + C_y^2 \tag{4.6}$$

In a classical random walk condition, R_j and C_j are normally distributed and the intensity probability generalizes the Rayleigh distribution to a chi-squared probability density with four degrees of freedom:

$$P(\mathcal{I}) = \frac{\mathcal{I}}{4\Gamma(4)} e^{-\frac{\mathcal{I}}{2}} \tag{4.7}$$

where Γ is the Gamma function. At large intensity, equation 4.7 is described well by a Rayleigh law, whereas at low $\mathcal{I}$ its shape is characterized by a pronounced peak. To compare NSOM experiments with FDTD data, we observe that equation 4.6 corresponds to the time average of the electromagnetic field in real space, that is $\mathcal{I} = \bar{\mathcal{E}}$, with $\bar{\mathcal{E}}$ denoting a time average of $\bar{\mathcal{E}}$ over one optical cycle.

4.9 Chaotic breakdown at larger wave-guide spacing d

We carried out a series of ray optics simulations on the structure illustrated in Fig. 4.2a, which represents an open optical billiard. Details on these types of structures and the associated ray optics simulations can be found in [110] and references therein. The dynamics of light rays is reported in the Poincare phase diagram (χ, Φ), defined by the reflection angleχ and the angle Φ between the system center and the intersection of the ray with the resonator boundary (Fig. 4.7a). Figures 4.7(b-e) shows our results in the case of (b) d = 1, (c) d = 7 and (d) d = 13. When the system is practically closed for d = 1, we observe fully developed chaos, with all the phase space (χ, Φ) randomly visited during the time evolution (Fig. 4.7b). For d = 7, 13, conversely, the system shows the alternation of chaotic islands and regular motion due to the reduction of the mixing properties of the system (Fig. 4.7d). As a result of the increased losses for $d > 1$, some portions of the phase space are never visited (Fig. 4.7cd), which is accompanied by a stronger reduction of the phase space portion that exhibit chaos, thus preventing an efficient generation of a chaotic sea from light reflections at the resonator boundaries.

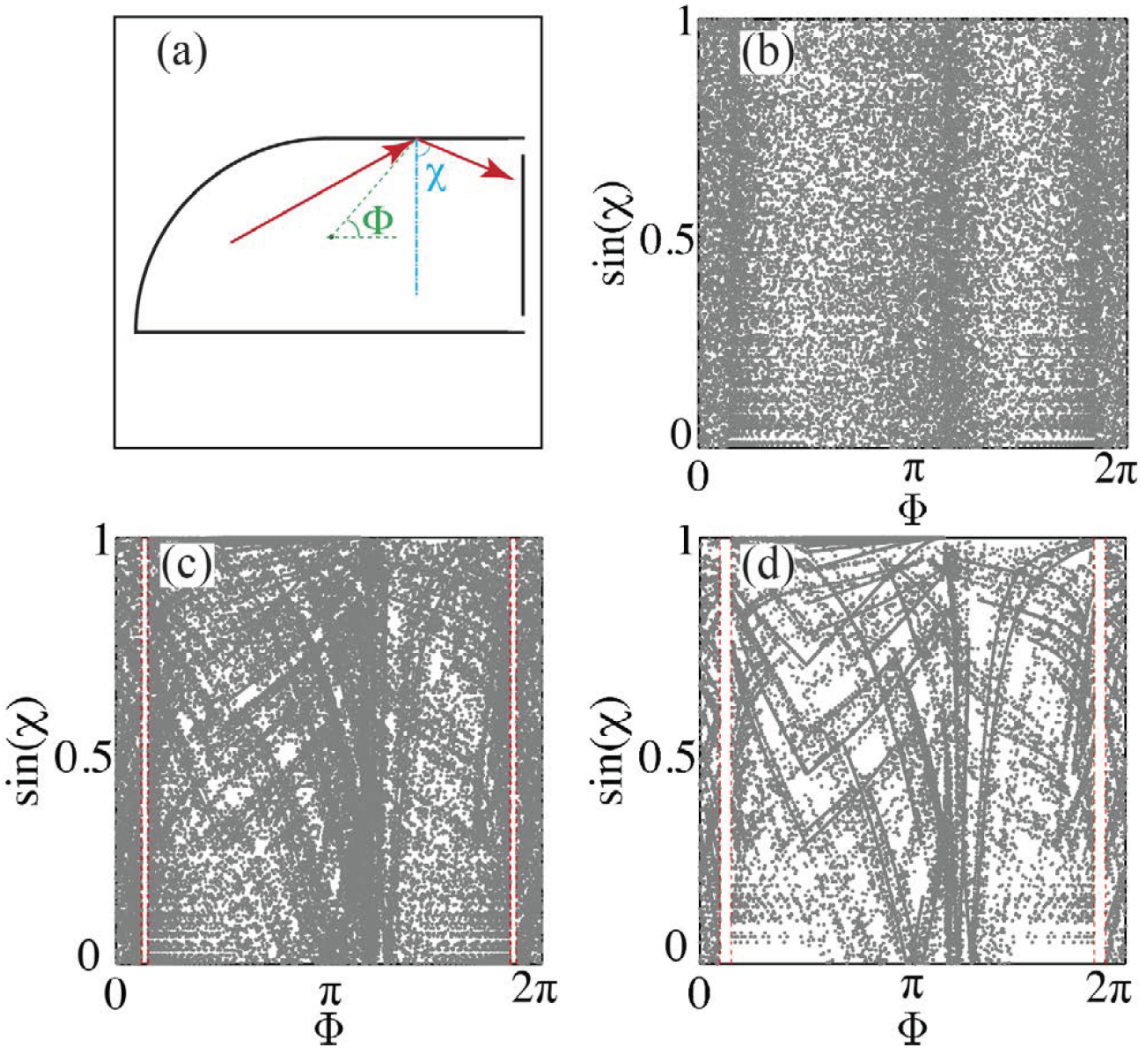

Figure 4.7: (a) The construction of the Poincare phase-space in the system. (b-d) Poincare diagram(χ, Φ) illustrating light dynamics inside the resonator in the case of (b) d = 0, (c) d = 7 and (d) d = 13.

Chapter 5

DICKE PHASE TRANSITION WITH MULTIPLE SUPERRADIANT STATES IN QUANTUM CHAOTIC RESONATORS

5.1 Introduction of superradiance

Superradiance is an emergent property of quantum systems that has stirred a large interest in scientific research [19, 120, 121, 122, 123, 124]. Initially predicted by Dicke in the context of two-level atoms [16], superradiance has been investigated in a wide range of systems including gases [18], plasmas [125], semiconductors [126, 127, 127, 128], free-electron lasers [129, 130], Bose-Einstein condensates [131, 132, 133, 134, 135], superconductors [136], quantum systems with impurities [137], and quantum dots [126, 138, 139]. In two-level media, a superradiant state results from the spontaneous synchronization of different atoms immersed in a common radi-

ation field, whose wavelength is larger than the volume occupied by the material. When this condition is met, a quantum phase transition occurs and atoms radiate energy with a quadratic dependence on their population ($\propto N^2$), much higher than the rate predicted by incoherent spontaneous emission ($\propto N^2$) [140, 141, 142, 143]. The consequence of such a superradiant behavior is recognized in the spatiotemporal domain, where a directional, short-lived energy burst is generated due to the enhanced radiation rate, while in the case of incoherent emission, only exponentially decaying intensity is observed [120].

The physics of the superradiant phase transition manifests itself in general N-body systems as a self-organization process [122]. In this context, the starting model is that of an effective, non-Hermitian Hamiltonian describing a system with open channels. When the system is closed and the channel strength is 0, the Hamiltonian is Hermitian and shows real eigenvalues with infinite lifetimes (i.e., zero imaginary component). As the coupling with the environment increases, imaginary eigenvalues appear in the spectrum and resonances become wider in the frequency domain, due to the finite lifetime of the corresponding eigenmodes. When resonances start to overlap, they coherently interact and reorganize, thus originating a phase transition where multiple superradiant states with broad widths emerge in the spectrum [144, 145, 146]. The existence of such a transition has also recently been argued as a mechanism to explain the strong deviations from classical Porter-Thomas probability distribution observed in neutron-resonance experiments, thus establishing new connections with the dynamics of complex nuclei [121]. However, if compared to the large body of theoretical results, experimental work has been limited in this area. As a consequence, several properties of superradiant states are still debated, including the emergence of specific scaling laws, the existence of universal statistics, and how these quantities dynamically approach the superradiant transition [147]. Understanding the features of the Dicke transition can be of primary importance

not only from a fundamental perspective but also to foster the realization of new devices, including terahertz amplifiers, optical emitters, and laser systems that are under intense investigation [123, 124, 148, 149, 150, 151].

5.2 Analogy between Schrodinger and Maxwell

In recent years, due to the many analogies between electrons and photons, light has become a widely used tool to investigate energy-transport dynamics. This analogy is particularly interesting in two dimensions, where the isomorphisms between Schrdinger and Maxwell equations allow us to investigate different quantum phenomena that manifest in dielectric optical microresonators whose forms mimic classically chaotic billiards [39, 152, 153, 154, 155, 156, 157, 76]. Here, we show that a suitably engineered optical resonator can mimic the dynamics of an open many-body system, allowing for a detailed study of superradiant states. One of the difficulties of the original system investigated by Dicke lies in the requirement of a coupling strength of the order of the energy separation of the atomic energy levels [134]. Our setup, conversely, takes its advantage from the technology of photonics crystals and allows the observation of any coupling regime [39, 63]. The use of transparent dielectrics, moreover, neglects any unwanted loss mechanism (such as, e.g., material absorption) and provides an ideal platform to investigate different properties of quantum chaotic systems.

Here, we show that a suitably engineered optical resonator can mimic the dynamics of an open many-body system, allowing for a detailed study of superradiant states. One of the difficulties of the original system investigated by Dicke lies in the requirement of a coupling strength of the order of the energy separation of the atomic energy levels [134]. Our setup, conversely, takes its advantage from the technology of photonics crystals and allows the observation of any coupling regime [39, 63]. The use of transparent dielectrics, moreover, neglects any unwanted loss mechanism (such as, e.g., material absorption) and provides an ideal platform to investigate different properties of quantum chaotic systems.

5.3 theoretical predictions: Random Matrix Theory modeling

An open quantum N-body system can be considered as an effective Hamiltonian H_{eff} coupled with M decay channels:

$$H_{eff} = H_0 - i\frac{\alpha}{2}VV^T \tag{5.1}$$

where H_0 is the Hamiltonian of the closed system and V is an N $\times$ M matrix that models the channel space, with the coupling amplitude defined by α. For nonzero α, the Hamiltonian H_{eft} is non-Hermitian and possesses a complex eigenvalue $\Omega_n = E_n - (i/2)\Gamma_n$, characterized by the energy $E_n = \hbar\omega$ and damping (or resonance width) Γ_n. The coupling strength κ between the system and the open space (i.e., the continuum of modes) can be evaluated as follows [145]:

$$\kappa = \frac{\mathrm{Im}\big[\mathrm{Tr}(H_{eff})\big]}{N\langle D\rangle} = \left\langle \frac{\Gamma}{D} \right\rangle \tag{5.2}$$

where the $\langle D\rangle$ is the mean energy-level distance and $\langle\Gamma\rangle$ is the mean value of the resonance width Γ.

At low coupling $\kappa \approx 0$, the resonance-width distribution follows a χ-squared [158], while for increasing κ, appreciable deviations for a χ^2 distribution are expected. In the latter case, numerical evidence suggests that the distribution of resonances follows a universal power-law γ_2 distribution [121]. The superradiant transition is theoretically predicted in the perfect coupling regime $\kappa = \kappa_c = 1$ [121, 145, 159, 160] , when resonances split and superradiant states emerge in the spectrum.

5.4 experimental results with two-dimensional chaotic optical resonators

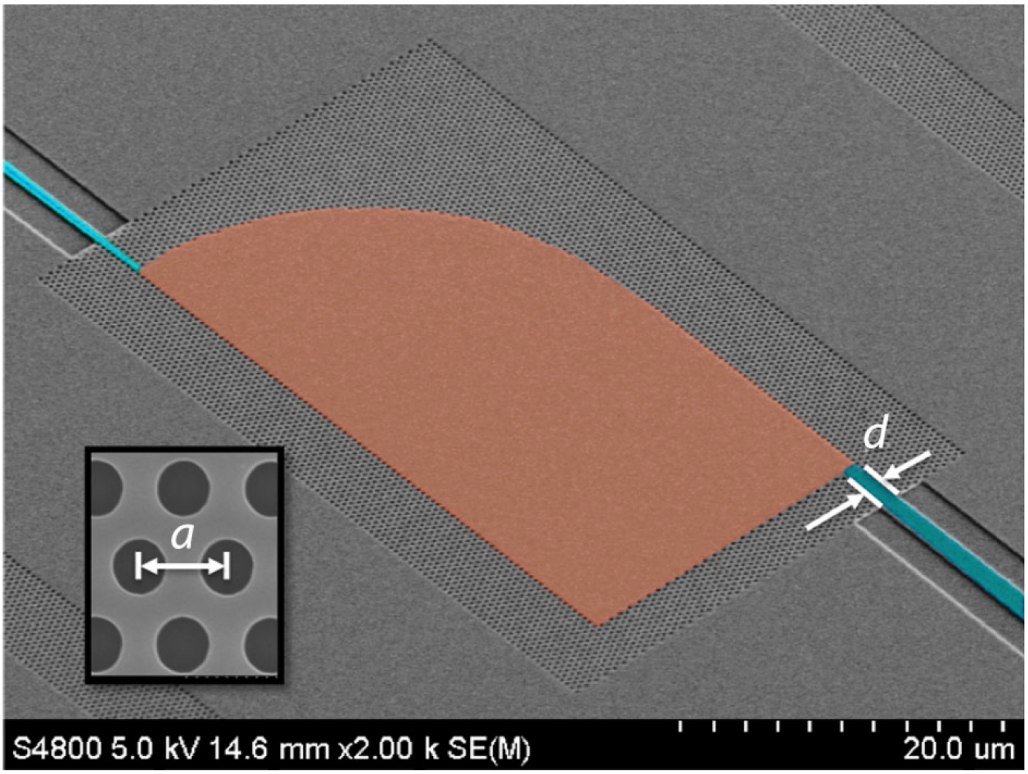

Figure 5.1: SEM image of the quarter-stadium resonator. Inset:Enlarged image of the photonic crystal lattice.

To investigate the appearance of the Dicke transition in our system, we design experiments based on open chaotic cavities realized in two-dimensional photonics crystals (PhCs) in a silicon-on-insulator platform. We chose the PhC technology for their versatility on managing light behavior on integrated photonics circuits [161, 162]. Figure 5.1 shows the SEM image of a typical sample, characterized by a quarter-stadium resonator equipped with input (left channel) and output (right channel) waveguides, the latter with a tunable width d. Fabrication details of the structure can be found in Ref. [39].

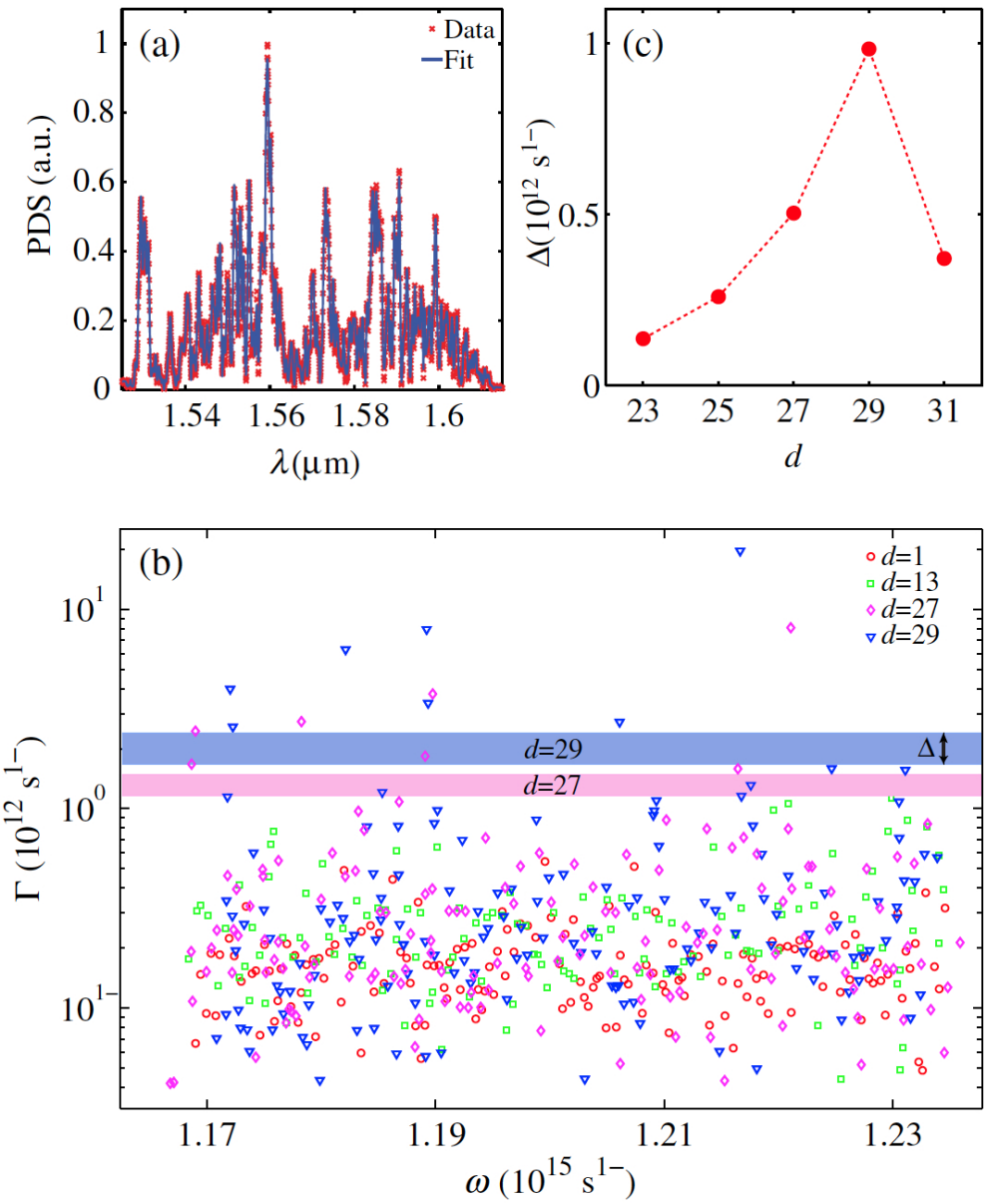

Figure 5.2: (a) Experimentally measured power-density spectrum (PDS) (cross markers) and theoretical reconstruction (solid line) via wavelet multiscale analysis for different waveguide spacings d. (b) Experimentally extracted resonance (ω, Γ) distribution for different output waveguide spacings d. (c) Experimentally measured gap width Δ, which separates superradiant states from long-living resonances, versus d.

The stadium shape guarantees that strong chaos is developed in the structure, thus leading to a fully random unperturbed Hamiltonian H_0. The area of the resonator is 800 μm^2. The inset of the same figure shows an enlarged view of the periodic

lattice, designed to work as omnidirectional mirror for light confined and polarized in the plane of the crystal. The period a = 450 nm and radius r = 0.3a place the working range of wavelength in the C + L band, around 1550 nm.

Resonance widths Γ_i and frequency eigenvalues ω_i can be accurately extracted from the transmitted power-density spectrum measured at the end of the output waveguide, by employing the experimental setup and the wavelet multiscale analysis described, e.g., in Ref. [39]. Figure 5.2 a displays a typical experimental spectrum and its reconstruction through multiscale analysis, showing the excellent accuracy of the reconstruction procedure. In order to obtain a complete statistic, we realize 48 samples and collect a total of 7000 resonances. Figure 5.2 b displays the resonance distribution in the plane (ω, Γ) for selected values of output channel width d. The latter is measured in lattice unit-cell units and is varied by removing an integer number of rows in the PhC.

Figure 5.2 shows the appearance of a superradiant transition when the spacing increases from d =1 to d=29. By increasing the waveguide spacing, in fact, we clearly observe resonances splitting with the emergence of a spectral gap [solid area in Fig. 5.2b], dividing the resonance plane(ω, Γ) into two distinct regions: a background containing a large multitude of long-living modes and M=7 superradiant states possessing very short lifetimes. The width of such superradiant states is about 100 times larger than the widths measured for d=1. In our experiments, the number of modes supported by the cavity is N $\approx 10^2$ (as extracted from wavelet multiscale analysis), which shows that the enhancement rate of short-living states is N times larger with respect to noninteracting resonances, in perfect agreement with what is expected for a superradiant behavior.

Figure 5.2 c shows the behavior of the gap width Δ versus waveguide spacing d. The gap manifests itself for d $\geq$23 and shows a strongly nonlinear behavior, which is observed as a quadratic increase up to d =29 with a further decrease for larger

increments of d. The specific number M=7 of superradiant states observed in our experiments depends on the nature of the cavity losses, which defines the size of the channel space. Multiple waveguide openings with different channel widths d, in particular, can sustain the formation of different channel spaces, leading to the generation of different numbers of superradiant states.

5.5 analysis of the properties of superradiant states

To quantitatively validate the occurrence of a superradiant phase transition, we calculate the parameter κ of Eq. 5.2. In order to get a self-consistent evaluation of this parameter, we employ an independent analysis based on RMT, which is able to furnish more informationsuch as, e.g., the number of open channels Mabout the dynamics of the Dicke transition. To this extent, we begin by diagonalizing an ensemble of H_{eff} given by Eq. 5.1 with H_0 taken from the Gaussian orthogonal ensemble of random matrices and the elements of V obeying a normal distribution with zero mean and unit standard deviation [147]. We then collect large statistics of the random-matrix eigenvalues and calculate the probability distribution $P_{RMT}(\Gamma)$ of resonance width Γ_i, comparing it with distributions $P_{exp}(\Gamma)$ calculated from the experimental data of Fig. 5.2 b.

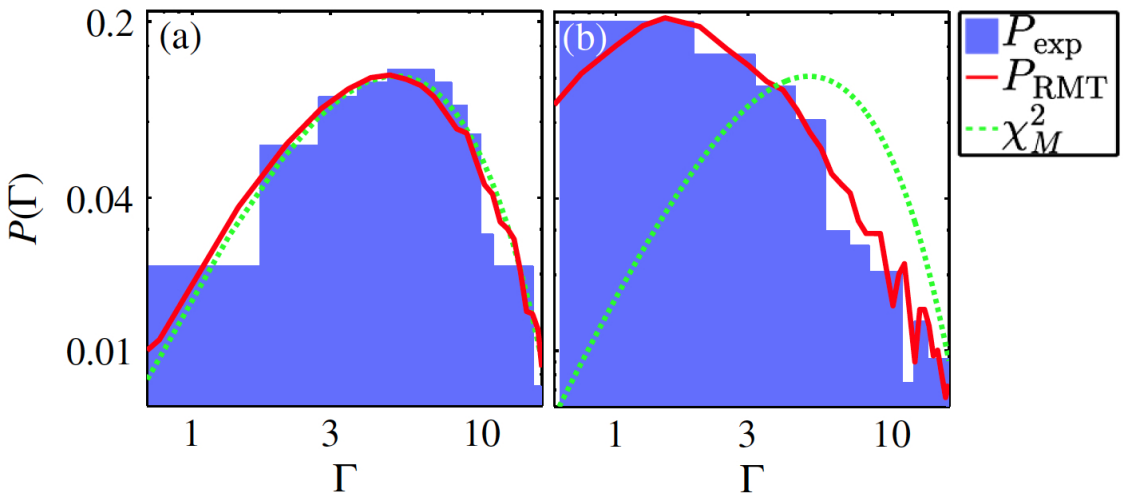

Figure 5.3: Experimentally extracted resonance-width distribution $P_{exp}(\Gamma)$ (solid curve) for (a) d=1 and (b) d=29, compared with numerically computed densities $P_{RMT}(\Gamma)$ from random-matrix-theory analysis (solid line) and with a χ^2 distribution (dashed line).

Figure 5.3 shows typical results in the low coupling [Fig. 3(a)] and superradiant

[Fig. 5.3 b] regimes. Probability densities $P_{RMT}(\Gamma)$ are parametrized by the number of open channels M and the coupling strength κ, the latter varied through α, while experimental P_{exp} distributions depend solely on the losses d. In our comparisons, we evaluate parameters M and κ by a least-squares fit of the $P_{RMT}(\Gamma)$ distribution with the corresponding experimental density $P_{exp}(\Gamma)$ computed at a specific d. Quite remarkably, for any spacing d, RMT analysis yields a constant channel-space size M= 7, which perfectly agrees with the experimental results of Fig. 5.2 that show the appearance of M=7 superradiant states. Figures 5.3 a and 5.3 b also compare experimental results with a χ^2 distribution (dashed line). The latter is known to correctly describe the regime of small resonances overlapping, i.e., $\kappa \ll 1$, and well matches the case of d=1, while it consistently fails in the superradiant case for d=29 due to strong resonances overlapping.

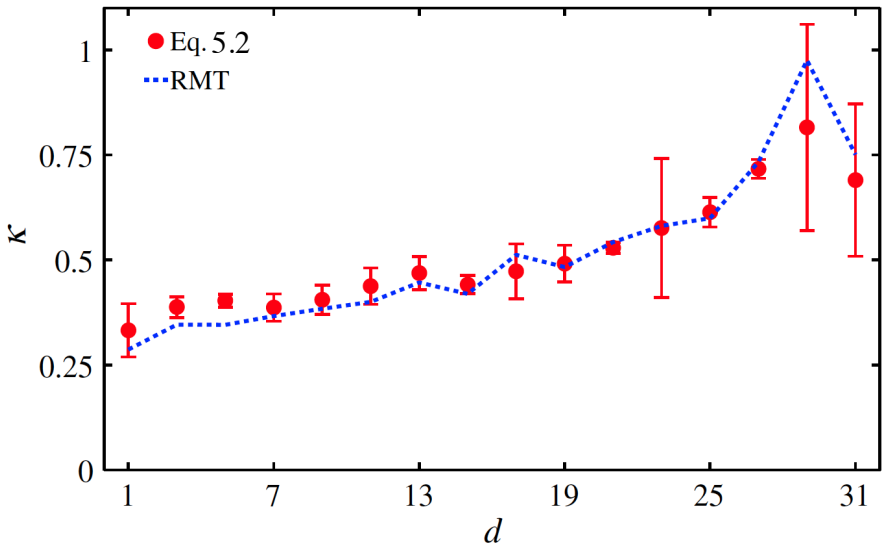

Figure 5.4: Experimentally calculated coupling strength κ versus d: comparison between estimates from Eq. 5.2 (markers) and RMT theory (dashed line).

In order to complete our self-consistent evaluation of κ, we compare RMT predictions with the direct application of Eq. 5.2 to our experimental results, investigating how the transition is approached when the losses d are increased. Figure **??**

shows our results. In general, the value of κ calculated through Eq. 5.2 matches very well the results of RMT, showing the clear appearance of a superradiant phase transition for $d \geq$ As the value of d is increased from d=1, in particular, the coupling strength κ increases from $\kappa \approx 0.3$ and reaches the critical point $\kappa_c \approx 1$ at d= 29. The behavior of κ versus d is strongly nonlinear and can be divided into three characteristic regions (Fig. 5.4). Below d =25, κ increases very slowly and linearly with d. For 25≤d≤29, we observe a dramatic increase toward the critic regime $\kappa_c = 1$, while for $d \geq 30$, we observe a decrement from $\kappa \approx 1$ to $\kappa \approx 0.7$. The latter is due to the breaking of the chaotic behavior of the resonator when the losses becomes too large, with the consequent weakening of the mixing property of the system.

A further analysis of superradiant transition concerns the scaling law of probability density $P_{exp}(\Gamma)$ for for large Γ. There is, in fact, numerical evidence from RMT analysis that the probability density in the superradiant regime follows a universal power law $\propto \Gamma^{-2}$ [121]. If this result is experimentally confirmed, it can provide a new test to verify the presence of a superradiant phase transition. Besides that, our setup also allows us to investigate the transition dynamics and how such power-law distribution is approached. To this extent, we fit the tail of the resonancewidth distribution $P_{exp}(\Gamma)$ with a power curve $\Gamma^{-\beta}$ and evaluate the coefficient ? from a least-squares procedure.

Figure 5.5 a illustrates our results for a varying coupling strength κ. Figure 5.5b shows a typical outcome of our fitting procedure, displaying an enlarged version of the probability distribution $P_{exp}(\Gamma)$ for d=29. As observed, the probability density at large Γ well agrees with a power-law Γ^{-2} curve. All the other cases (not reported here) are represented with the same degree of accuracy by a $\Gamma^{-\beta}$ function. The dynamics of β for varying losses d follows a similar behavior of κ versus d: For d<25, we observe a slowly linear decrease from $\beta \approx 2.5$, while for d>25, when the super-

radiant phase transition appears, the dynamics dramatically converges to $\beta \approx 2$, experimentally confirming the prediction of RMT.

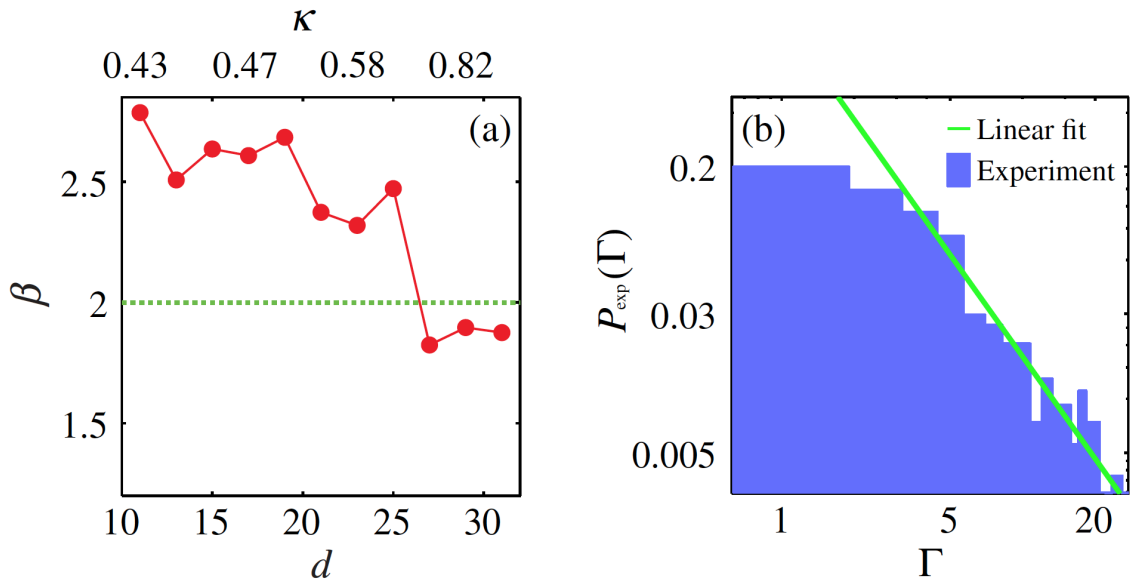

Figure 5.5: (a) Power-law exponent β (markers) of the large Γ behavior of $P_{exp}(\Gamma) \propto \Gamma^{-\beta}$ at different d. The limiting value $\beta = 2$ is reported as a dashed line. (b) Comparison between experimental $P_{exp}(\Gamma)$ for d=29 (solid curve) and power-law distribution Γ^{-2} (solid line).

5.6 discussion

We designed a transparent optical material to investigate the dynamics of the superradiant phase transition in the presence of multiple superradiant states. Our system circumvented the difficulties in observing the Dicke transition in two-level atomic media and allowed a detailed experimental study of superradiant states. Our results showed that the dynamics of the Dicke transition is strongly nonlinear: Characteristic quantities vary slowly below the critical coupling $\kappa_c = 1$, while near κ_c, the superradiant transition appears dramatically, with the system entering a new self-organized phase. This regime has been experimentally observed by the emergence of $M = 7$ superradiant states, whose resonance widths are N times larger than all the others, with N being the total number of resonances. In the superradiant regime, we demonstrated that the resonance-width probability of superradiant states follows a Γ^{-2}power law, which provides a new criterion to test the occurrence of a superradiant transition in a physical system. This work is expected to stimulate new fundamental studies on cooperative dynamics and facilitate the development of novel applications of many-body systems.

Chapter 6

CONCLUDING REMARKS

6.1 Summary

In this thesis, with the inspiration from the Nature evolution, we show how we can design and manipulate the optical properties in chaotic resonators.

A simple deformation to the geometry will introduce the chaos into the system, stimulating the phenomena of energy equipartition that can dramatically enhance the energy storage ability of a resonator. Using similar principle by a random distribution of designed nano structures, we can further increase the energy harvesting, i.e. building a blackbody system can collect all the energy from ultraviolet to infrared, with the practical application not only as a perfect absorber but also a new type of light source.

Inspired by the Rogue waves in the ocean, we firstly designed and realized its optical counterpart in a linear regime. With the aid of chaos embedded in the geometry of resonator, we can localized the light beyond the diffraction limit, creating another pathway to manipulate light at nanoscale in a homogeneous media without sophisticated structures. With similar chaotic resonators, we realize Dicke superradiance experimentally in a pure optical structure, providing a simple to test the Dicke transition as the analog of atomic systems.

REFERENCES

[1] U. G. Wegst, H. Bai, E. Saiz, A. P. Tomsia, and R. O. Ritchie, "Bioinspired structural materials," *Nature materials*, 2014.

[2] B. K. Ahn, S. Das, R. Linstadt, Y. Kaufman, N. R. Martinez-Rodriguez, R. Mirshafian, E. Kesselman, Y. Talmon, B. H. Lipshutz, J. N. Israelachvili *et al.*, "High-performance mussel-inspired adhesives of reduced complexity," *Nature communications*, vol. 6, 2015.

[3] P. Tao, W. Shang, C. Song, Q. Shen, F. Zhang, Z. Luo, N. Yi, D. Zhang, and T. Deng, "Bioinspired engineering of thermal materials," *Advanced Materials*, vol. 27, no. 3, pp. 428–463, 2015.

[4] R. A. Potyrailo, R. K. Bonam, J. G. Hartley, T. A. Starkey, P. Vukusic, M. Vasudev, T. Bunning, R. R. Naik, Z. Tang, M. A. Palacios *et al.*, "Towards outperforming conventional sensor arrays with fabricated individual photonic vapour sensors inspired by morpho butterflies," *Nature communications*, vol. 6, 2015.

[5] N. N. Shi, C.-C. Tsai, F. Camino, G. D. Bernard, N. Yu, and R. Wehner, "Keeping cool: Enhanced optical reflection and radiative heat dissipation in saharan silver ants," *Science*, vol. 349, no. 6245, pp. 298–301, 2015.

[6] A. P. Raman, M. A. Anoma, L. Zhu, E. Rephaeli, and S. Fan, "Passive radiative cooling below ambient air temperature under direct sunlight," *Nature*, vol. 515, no. 7528, pp. 540–544, 2014.

[7] V. Saranathan, C. O. Osuji, S. G. Mochrie, H. Noh, S. Narayanan, A. Sandy, E. R. Dufresne, and R. O. Prum, "Structure, function, and self-assembly of single network gyroid (i4132) photonic crystals in butterfly wing scales," *Pro-*

ceedings of the National Academy of Sciences, vol. 107, no. 26, pp. 11 676–11 681, 2010.

[8] H. Yin, B. Dong, X. Liu, T. Zhan, L. Shi, J. Zi, and E. Yablonovitch, "Amorphous diamond-structured photonic crystal in the feather barbs of the scarlet macaw," *Proceedings of the National Academy of Sciences*, vol. 109, no. 27, pp. 10 798–10 801, 2012.

[9] P. Vukusic, B. Hallam, and J. Noyes, "Brilliant whiteness in ultrathin beetle scales," *Science*, vol. 315, no. 5810, pp. 348–348, 2007.

[10] Q. Bao and K. P. Loh, "Graphene photonics, plasmonics, and broadband optoelectronic devices," *ACS nano*, vol. 6, no. 5, pp. 3677–3694, 2012.

[11] M. L. Brongersma, Y. Cui, and S. Fan, "Light management for photovoltaics using high-index nanostructures," *Nature materials*, vol. 13, no. 5, pp. 451–460, 2014.

[12] H. A. Haus, *Waves and Fields in Optoelectronics*. Prentice Hall, 1984.

[13] K. Mizuno, J. Ishii, H. Kishida, Y. Hayamizu, S. Yasuda, D. N. Futaba, M. Yumura, and K. Hata, "A black body absorber from vertically aligned single-walled carbon nanotubes," *Proceedings of the National Academy of Sciences*, vol. 106, no. 15, pp. 6044–6047, 2009.

[14] M. Onorato, S. Residori, U. Bortolozzo, A. Montina, and F. Arecchi, "Rogue waves and their generating mechanisms in different physical contexts," *Physics Reports*, vol. 528, no. 2, pp. 47–89, 2013.

[15] J. M. Dudley, F. Dias, M. Erkintalo, and G. Genty, "Instabilities, breathers and rogue waves in optics," *Nature Photonics*, vol. 8, no. 10, pp. 755–764, 2014.

[16] R. H. Dicke, "Coherence in spontaneous radiation processes," *Physical Review*, vol. 93, no. 1, p. 99, 1954.

[17] A. Kalachev and V. Samartsev, "Optical superradiance in impurity crystals and its possible applications," *LASER PHYSICS-LAWRENCE-*, vol. 12, no. 8, pp. 1114–1125, 2002.

[18] N. Skribanowitz, I. Herman, J. MacGillivray, and M. Feld, "Observation of dicke superradiance in optically pumped hf gas," *Physical Review Letters*, vol. 30, no. 8, p. 309, 1973.

[19] M. Gross and S. Haroche, "Superradiance: an essay on the theory of collective spontaneous emission," *Physics Reports*, vol. 93, no. 5, pp. 301–396, 1982.

[20] H. Mabuchi and A. Doherty, "Cavity quantum electrodynamics: coherence in context," *Science*, vol. 298, no. 5597, pp. 1372–1377, 2002.

[21] J. Clark and G. Lanzani, "Organic photonics for communications," *Nature photonics*, vol. 4, no. 7, pp. 438–446, 2010.

[22] K. Nozaki, A. Shinya, S. Matsuo, Y. Suzaki, T. Segawa, T. Sato, Y. Kawaguchi, R. Takahashi, and M. Notomi, "Ultralow-power all-optical ram based on nanocavities," *Nature Photonics*, vol. 6, no. 4, pp. 248–252, 2012.

[23] F. Leo, S. Coen, P. Kockaert, S.-P. Gorza, P. Emplit, and M. Haelterman, "Temporal cavity solitons in one-dimensional kerr media as bits in an all-optical buffer," *Nature Photonics*, vol. 4, no. 7, pp. 471–476, 2010.

[24] H. A. Atwater and A. Polman, "Plasmonics for improved photovoltaic devices," *Nature materials*, vol. 9, no. 3, pp. 205–213, 2010.

[25] A. Chalcraft, S. Lam, D. O'Brien, T. Krauss, M. Sahin, D. Szymanski, D. Sanvitto, R. Oulton, M. Skolnick, A. Fox *et al.*, "Mode structure of the l3 photonic crystal cavity," *Applied Physics Letters*, vol. 90, no. 24, pp. 241 117–241 117, 2007.

[26] R. K. Chang and A. J. Campillo, *Optical processes in microcavities*. World scientific, 1996, vol. 3.

[27] T. Gensty, K. Becker, I. Fischer, W. Elsäßer, C. Degen, P. Debernardi, and G. P. Bava, "Wave chaos in real-world vertical-cavity surface-emitting lasers," *Physical review letters*, vol. 94, no. 23, p. 233901, 2005.

[28] J. U. Nockel and A. D. Stone, "Ray and wave chaos in asymmetric resonant optical cavities," *Nature*, vol. 385, no. 6611, pp. 45–47, 01 1997.

[29] T. Harayama, P. Davis, and K. S. Ikeda, "Stable oscillations of a spatially chaotic wave function in a microstadium laser," *Physical review letters*, vol. 90, no. 6, p. 063901, 2003.

[30] C. Gmachl, F. Capasso, E. Narimanov, J. U. Nöckel, A. D. Stone, J. Faist, D. L. Sivco, and A. Y. Cho, "High-power directional emission from microlasers with chaotic resonators," *Science*, vol. 280, no. 5369, pp. 1556–1564, 1998.

[31] C. Michel, V. Doya, O. Legrand, and F. Mortessagne, "Selective amplification of scars in a chaotic optical fiber," *Physical review letters*, vol. 99, no. 22, p. 224101, 2007.

[32] T.-D. Lee, C.-Y. Chen, Y. Lin, M.-C. Chou, T.-h. Wu, and R.-K. Lee, "Surface-structure-assisted chaotic mode lasing in vertical cavity surface emitting lasers," *Physical review letters*, vol. 101, no. 8, p. 084101, 2008.

[33] C. Chen, Y. Yu, R. C. Chen, Y. Huang, K. Su, Y. Chen, and K. Huang, "Transient dynamics of coherent waves released from quantum billiards and analogous observation from free-space propagation of laser modes," *Physical review letters*, vol. 102, no. 4, p. 044101, 2009.

[34] P. Brouwer, K. Frahm, and C. Beenakker, "Quantum mechanical time-delay matrix in chaotic scattering," *Physical review letters*, vol. 78, no. 25, p. 4737, 1997.

[35] G. S. Murugan, J. S. Wilkinson, and M. N. Zervas, "Optical microdiscus resonators by flattening microspheres," *Applied Physics Letters*, vol. 101, no. 7, p. 071106, 2012.

[36] M. Robnik, "Classical dynamics of a family of billiards with analytic boundaries," *Journal of Physics A: Mathematical and General*, vol. 16, no. 17, p. 3971, 1983.

[37] A. G. Tyhuis, *Electromagnetic inverse Profiling.* VNU Science Press, 1987.

[38] G. Gallavotti, *Statistical mechanics: A short treatise.* Springer Science & Business Media, 2013.

[39] A. Di Falco, T. Krauss, and A. Fratalocchi, "Lifetime statistics of quantum chaos studied by a multiscale analysis," *Applied Physics Letters*, vol. 100, no. 18, p. 184101, 2012.

[40] L. Malaquin, T. Kraus, H. Schmid, E. Delamarche, and H. Wolf, "Controlled particle placement through convective and capillary assembly," *Langmuir*, vol. 23, no. 23, pp. 11 513–11 521, 2007.

[41] X.-H. Li, R. Song, Y.-K. Ee, P. Kumnorkaew, J. F. Gilchrist, and N. Tansu, "Light extraction efficiency and radiation patterns of iii-nitride light-emitting diodes with colloidal microlens arrays with various aspect ratios," *Photonics Journal, IEEE*, vol. 3, no. 3, pp. 489–499, 2011.

[42] K. Y. Suh, H. Yoon, H. H. Lee, A. Khademhosseini, and R. Langer, "Solventless ordering of colloidal particles through application of patterned elastomeric stamps under pressure," *Applied physics letters*, vol. 85, no. 13, pp. 2643–2645, 2004.

[43] E. Ott, *Chaos in dynamical systems.* Cambridge university press, 2002.

[44] G. Boffetta, M. Cencini, M. Falcioni, and A. Vulpiani, "Predictability: a way to characterize complexity," *Physics reports*, vol. 356, no. 6, pp. 367–474, 2002.

[45] A. Cao, X. Zhang, C. Xu, B. Wei, and D. Wu, "Tandem structure of aligned carbon nanotubes on au and its solar thermal absorption," *Solar energy materials and solar cells*, vol. 70, no. 4, pp. 481–486, 2002.

[46] M. Lira-Cantú, A. M. Sabio, A. Brustenga, and P. Gómez-Romero, "Electrochemical deposition of black nickel solar absorber coatings on stainless steel aisi316l for thermal solar cells," *Solar energy materials and solar cells*, vol. 87, no. 1, pp. 685–694, 2005.

[47] J. Lehman, A. Sanders, L. Hanssen, B. Wilthan, J. Zeng, and C. Jensen, "Very black infrared detector from vertically aligned carbon nanotubes and electric-field poling of lithium tantalate," *Nano letters*, vol. 10, no. 9, pp. 3261–3266, 2010.

[48] N. Liu, M. Mesch, T. Weiss, M. Hentschel, and H. Giessen, "Infrared perfect absorber and its application as plasmonic sensor," *Nano letters*, vol. 10, no. 7, pp. 2342–2348, 2010.

[49] A. Lenert, D. M. Bierman, Y. Nam, W. R. Chan, I. Celanović, M. Soljačić, and E. N. Wang, "A nanophotonic solar thermophotovoltaic device," *Nature nanotechnology*, vol. 9, no. 2, pp. 126–130, 2014.

[50] T. V. Teperik, F. G. De Abajo, A. Borisov, M. Abdelsalam, P. Bartlett, Y. Sugawara, and J. Baumberg, "Omnidirectional absorption in nanostructured metal surfaces," *Nature photonics*, vol. 2, no. 5, pp. 299–301, 2008.

[51] K. Aydin, V. E. Ferry, R. M. Briggs, and H. A. Atwater, "Broadband polarization-independent resonant light absorption using ultrathin plasmonic super absorbers," *Nature communications*, vol. 2, p. 517, 2011.

[52] Y. Cui, K. H. Fung, J. Xu, H. Ma, Y. Jin, S. He, and N. X. Fang, "Ultrabroadband light absorption by a sawtooth anisotropic metamaterial slab," *Nano letters*, vol. 12, no. 3, pp. 1443–1447, 2012.

[53] M. A. Kats, R. Blanchard, P. Genevet, and F. Capasso, "Nanometre optical coatings based on strong interference effects in highly absorbing media," *Nature materials*, vol. 12, no. 1, pp. 20–24, 2013.

[54] P. W. Milonni, *The Quantum Vacuum.* (Academic, 1994.

[55] J.-J. Greffet, R. Carminati, K. Joulain, J.-P. Mulet, S. Mainguy, and Y. Chen, "Coherent emission of light by thermal sources," *Nature*, vol. 416, no. 6876, pp. 61–64, 2002.

[56] D. Mann, Y. Kato, A. Kinkhabwala, E. Pop, J. Cao, X. Wang, L. Zhang, Q. Wang, J. Guo, and H. Dai, "Electrically driven thermal light emission from individual single-walled carbon nanotubes," *Nature Nanotechnology*, vol. 2, no. 1, pp. 33–38, 2007.

[57] Y.-F. Huang, S. Chattopadhyay, Y.-J. Jen, C.-Y. Peng, T.-A. Liu, Y.-K. Hsu, C.-L. Pan, H.-C. Lo, C.-H. Hsu, Y.-H. Chang *et al.*, "Improved broadband and quasi-omnidirectional anti-reflection properties with biomimetic silicon nanostructures," *Nature nanotechnology*, vol. 2, no. 12, pp. 770–774, 2007.

[58] Z. Yu, A. Raman, and S. Fan, "Fundamental limit of nanophotonic light trapping in solar cells," *Proceedings of the National Academy of Sciences*, vol. 107, no. 41, pp. 17 491–17 496, 2010.

[59] Z.-P. Yang, L. Ci, J. A. Bur, S.-Y. Lin, and P. M. Ajayan, "Experimental observation of an extremely dark material made by a low-density nanotube array," *Nano letters*, vol. 8, no. 2, pp. 446–451, 2008.

[60] N. Selvakumar, S. Krupanidhi, and H. C. Barshilia, "Carbon nanotube-based tandem absorber with tunable spectral selectivity: Transition from near-perfect blackbody absorber to solar selective absorber," *Advanced Materials*, vol. 26, no. 16, pp. 2552–2557, 2014.

[61] T. Matsumoto, T. Koizumi, Y. Kawakami, K. Okamoto, and M. Tomita, "Perfect blackbody radiation from a graphene nanostructure with application to high-temperature spectral emissivity measurements," *Optics express*, vol. 21, no. 25, pp. 30 964–30 974, 2013.

[62] J. Zhu, Z. Yu, G. F. Burkhard, C.-M. Hsu, S. T. Connor, Y. Xu, Q. Wang, M. McGehee, S. Fan, and Y. Cui, "Optical absorption enhancement in amorphous silicon nanowire and nanocone arrays," *Nano letters*, vol. 9, no. 1, pp. 279–282, 2008.

[63] C. Liu, A. Di Falco, D. Molinari, Y. Khan, B. Ooi, T. Krauss, and A. Fratalocchi, "Enhanced energy storage in chaotic optical resonators," *Nature Photonics*, vol. 7, no. 6, pp. 473–478, 2013.

[64] C. Conti, M. Leonetti, A. Fratalocchi, L. Angelani, and G. Ruocco, "Condensation in disordered lasers: Theory, 3 d+ 1 simulations, and experiments," *Physical review letters*, vol. 101, no. 14, p. 143901, 2008.

[65] A. Picozzi, J. Garnier, T. Hansson, P. Suret, S. Randoux, G. Millot, and D. Christodoulides, "Optical wave turbulence: towards a unified nonequilibrium thermodynamic formulation of statistical nonlinear optics," *Physics Reports*, vol. 542, no. 1, pp. 1–132, 2014.

[66] R. Weill, B. Fischer, and O. Gat, "Light-mode condensation in actively-mode-locked lasers," *Phys. Rev. Lett.*, vol. 104, p. 173901, 2010.

[67] A. Fratalocchi, "Mode-locked lasers: Light condensation," *Nature Photonics*, vol. 4, no. 8, pp. 502–503, 2010.

[68] J. Klaers, J. Schmitt, F. Vewinger, and M. Weitz, "Bose-einstein condensation of photons in an optical microcavity," *Nature*, vol. 468, no. 7323, pp. 545–548, 2010.

[69] P. Vukusic, B. Hallam, and J. Noyes, "Brilliant whiteness in ultrathin beetle scales," *Science*, vol. 315, no. 5810, pp. 348–348, 2007.

[70] U. Leonhardt, "Optical conformal mapping," *Science*, vol. 312, no. 5781, pp. 1777–1780, 2006.

[71] J. Pendry, A. Aubry, D. Smith, and S. Maier, "Transformation optics and subwavelength control of light," *science*, vol. 337, no. 6094, pp. 549–552, 2012.

[72] W. Ni, X. Kou, Z. Yang, and J. Wang, "Tailoring longitudinal surface plasmon wavelengths, scattering and absorption cross sections of gold nanorods," *Acs Nano*, vol. 2, no. 4, pp. 677–686, 2008.

[73] J. Huang, Y. Zhu, M. Lin, Q. Wang, L. Zhao, Y. Yang, K. X. Yao, and Y. Han, "Site-specific growth of au–pd alloy horns on au nanorods: a platform for highly sensitive monitoring of catalytic reactions by surface enhancement raman spectroscopy," *Journal of the American Chemical Society*, vol. 135, no. 23, pp. 8552–8561, 2013.

[74] M. Noginov, G. Zhu, A. Belgrave, R. Bakker, V. Shalaev, E. Narimanov, S. Stout, E. Herz, T. Suteewong, and U. Wiesner, "Demonstration of a spaser-based nanolaser," *Nature*, vol. 460, no. 7259, pp. 1110–1112, 2009.

[75] J. T. Verdeyen, *Laser electronics*. Prentice Hall, Englewood Cliffs, NJ, 1989.

[76] C. Conti and A. Fratalocchi, "Dynamic light diffusion, three-dimensional anderson localization and lasing in inverted opals," *Nature Physics*, vol. 4, no. 10, pp. 794–798, 2008.

[77] S. A. Maier, *Plasmonics: fundamentals and applications*. Springer Science & Business Media, 2007.

[78] I. Malitson, "Interspecimen comparison of the refractive index of fused silica," *JOSA*, vol. 55, no. 10, pp. 1205–1208, 1965.

[79] G. M. Hale and M. R. Querry, "Optical constants of water in the 200-nm to 200-μm wavelength region," *Applied optics*, vol. 12, no. 3, pp. 555–563, 1973.

[80] R. J. Glauber and M. Lewenstein, "Quantum optics of dielectric media," *Physical Review A*, vol. 43, no. 1, p. 467, 1991.

[81] C. De Dominicis and I. Giardina, *Random fields and spin glasses: a field theory approach*. Cambridge University Press, 2006.

[82] M. Mehta, *Random Matrices*. New York: Academic Press, 1991.

[83] R. F. Oulton, V. J. Sorger, T. Zentgraf, R.-M. Ma, C. Gladden, L. Dai, G. Bartal, and X. Zhang, "Plasmon lasers at deep subwavelength scale," *Nature*, vol. 461, no. 7264, pp. 629–632, 2009.

[84] J. Chen, M. Badioli, P. Alonso-González, S. Thongrattanasiri, F. Huth, J. Osmond, M. Spasenović, A. Centeno, A. Pesquera, P. Godignon *et al.*, "Optical nano-imaging of gate-tunable graphene plasmons," *Nature*, vol. 487, no. 7405, pp. 77–81, 2012.

[85] D. K. Gramotnev and S. I. Bozhevolnyi, "Plasmonics beyond the diffraction limit," *Nature photonics*, vol. 4, no. 2, pp. 83–91, 2010.

[86] G. M. Lerman, A. Yanai, and U. Levy, "Demonstration of nanofocusing by the use of plasmonic lens illuminated with radially polarized light," *Nano letters*, vol. 9, no. 5, pp. 2139–2143, 2009.

[87] X. Zhang and Z. Liu, "Superlenses to overcome the diffraction limit," *Nature materials*, vol. 7, no. 6, pp. 435–441, 2008.

[88] J. A. Schuller, E. S. Barnard, W. Cai, Y. C. Jun, J. S. White, and M. L. Brongersma, "Plasmonics for extreme light concentration and manipulation," *Nature materials*, vol. 9, no. 3, pp. 193–204, 2010.

[89] A. Polman and H. A. Atwater, "Photonic design principles for ultrahigh-efficiency photovoltaics," *Nature materials*, vol. 11, no. 3, pp. 174–177, 2012.

[90] Y. Nishijima, L. Rosa, and S. Juodkazis, "Surface plasmon resonances in periodic and random patterns of gold nano-disks for broadband light harvesting," *Optics express*, vol. 20, no. 10, pp. 11 466–11 477, 2012.

[91] E. T. Rogers, J. Lindberg, T. Roy, S. Savo, J. E. Chad, M. R. Dennis, and N. I. Zheludev, "A super-oscillatory lens optical microscope for subwavelength imaging," *Nature materials*, vol. 11, no. 5, pp. 432–435, 2012.

[92] T. Kao, E. Rogers, J. Ou, and N. Zheludev, "digitally addressable focusing of light into a subwavelength hot spot," *Nano letters*, vol. 12, no. 6, pp. 2728–2731, 2012.

[93] Y. Choi, T. D. Yang, C. Fang-Yen, P. Kang, K. J. Lee, R. R. Dasari, M. S. Feld, and W. Choi, "Overcoming the diffraction limit using multiple light

scattering in a highly disordered medium," *Physical review letters*, vol. 107, no. 2, p. 023902, 2011.

[94] I. Vellekoop, A. Lagendijk, and A. Mosk, "Exploiting disorder for perfect focusing," *Nature Photonics*, vol. 4, no. 5, pp. 320–322, 2010.

[95] O. Katz, E. Small, Y. Bromberg, and Y. Silberberg, "Focusing and compression of ultrashort pulses through scattering media," *Nature photonics*, vol. 5, no. 6, pp. 372–377, 2011.

[96] G. Krauss, S. Lohss, T. Hanke, A. Sell, S. Eggert, R. Huber, and A. Leitenstorfer, "Synthesis of a single cycle of light with compact erbium-doped fibre technology," *Nature Photonics*, vol. 4, no. 1, pp. 33–36, 2010.

[97] B. Oktem, C. Ülgüdür, and F. Ö. Ilday, "Soliton–similariton fibre laser," *Nature Photonics*, vol. 4, no. 5, pp. 307–311, 2010.

[98] M. Onorato, A. R. Osborne, M. Serio, and S. Bertone, "Freak waves in random oceanic sea states," *Physical Review Letters*, vol. 86, no. 25, p. 5831, 2001.

[99] A. Ganshin, V. Efimov, G. Kolmakov, L. Mezhov-Deglin, and P. V. McClintock, "Observation of an inverse energy cascade in developed acoustic turbulence in superfluid helium," *Physical review letters*, vol. 101, no. 6, p. 065303, 2008.

[100] R. Höhmann, U. Kuhl, H.-J. Stöckmann, L. Kaplan, and E. Heller, "Freak waves in the linear regime: A microwave study," *Physical review letters*, vol. 104, no. 9, p. 093901, 2010.

[101] D. Solli, C. Ropers, P. Koonath, and B. Jalali, "Optical rogue waves," *Nature*, vol. 450, no. 7172, pp. 1054–1057, 2007.

[102] J. M. Dudley, G. Genty, and B. J. Eggleton, "Harnessing and control of optical rogue waves in supercontinuum generation," *Optics Express*, vol. 16, no. 6, pp. 3644–3651, 2008.

[103] J. Kasparian, P. Béjot, J.-P. Wolf, and J. M. Dudley, "Optical rogue wave statistics in laser filamentation," *Optics express*, vol. 17, no. 14, pp. 12 070–12 075, 2009.

[104] A. Karsaklian Dal Bosco, D. Wolfersberger, and M. Sciamanna, "Extreme events in time-delayed nonlinear optics," *Optics letters*, vol. 38, no. 5, pp. 703–705, 2013.

[105] N. Marsal, V. Caullet, D. Wolfersberger, and M. Sciamanna, "Spatial rogue waves in a photorefractive pattern-forming system," *Optics letters*, vol. 39, no. 12, pp. 3690–3693, 2014.

[106] A. Picozzi, J. Garnier, T. Hansson, P. Suret, S. Randoux, G. Millot, and D. Christodoulides, "Optical wave turbulence: towards a unified nonequilibrium thermodynamic formulation of statistical nonlinear optics," *Physics Reports*, vol. 542, no. 1, pp. 1–132, 2014.

[107] K. Hammani, B. Kibler, C. Finot, and A. Picozzi, "Emergence of rogue waves from optical turbulence," *Physics Letters A*, vol. 374, no. 34, pp. 3585–3589, 2010.

[108] C. Bonatto, M. Feyereisen, S. Barland, M. Giudici, C. Masoller, J. R. R. Leite, and J. R. Tredicce, "Deterministic optical rogue waves," *Physical review letters*, vol. 107, no. 5, p. 053901, 2011.

[109] F. Baronio, A. Degasperis, M. Conforti, and S. Wabnitz, "Solutions of the vector nonlinear schrödinger equations: evidence for deterministic rogue waves," *Physical review letters*, vol. 109, no. 4, p. 044102, 2012.

[110] H.-J. Stöckmann, *Quantum chaos: an introduction*. Cambridge university press, 2006.

[111] M. Sandtke, R. Engelen, H. Schoenmaker, I. Attema, H. Dekker, I. Cerjak, J. Korterik, F. Segerink, and L. Kuipers, "Novel instrument for surface plasmon polariton tracking in space and time," *Review of scientific instruments*, vol. 79, no. 1, p. 013704, 2008.

[112] M. Berry, "A note on superoscillations associated with bessel beams," *Journal of Optics*, vol. 15, no. 4, p. 044006, 2013.

[113] K. Dysthe, H. E. Krogstad, and P. Müller, "Oceanic rogue waves," *Annu. Rev. Fluid Mech.*, vol. 40, pp. 287–310, 2008.

[114] B. Redding, S. F. Liew, R. Sarma, and H. Cao, "Compact spectrometer based on a disordered photonic chip," *Nature Photonics*, vol. 7, no. 9, pp. 746–751, 2013.

[115] S. D. Cohen, H. L. d. S. Cavalcante, and D. J. Gauthier, "Subwavelength position sensing using nonlinear feedback and wave chaos," *Physical review letters*, vol. 107, no. 25, p. 17, 2011.

[116] B. Cahill and A. Lewis, "Resource variability and extreme wave conditions at the atlantic marine energy test siter," in *4th International Conference on Ocean Energy*, Dublin, Oct. 2011.

[117] S. Vergeles and S. K. Turitsyn, "Optical rogue waves in telecommunication data streams," *Physical Review A*, vol. 83, no. 6, p. 061801, 2011.

[118] J. F. Hauer, C. Demeure, and L. Scharf, "Initial results in prony analysis of power system response signals," *Power Systems, IEEE Transactions on*, vol. 5, no. 1, pp. 80–89, 1990.

[119] N. Rotenberg and L. Kuipers, "Mapping nanoscale light fields," *Nature Photonics*, vol. 8, no. 12, pp. 919–926, 2014.

[120] T. Brandes, "Coherent and collective quantum optical effects in mesoscopic systems," *physics reports*, vol. 408, no. 5, pp. 315–474, 2005.

[121] G. Celardo, N. Auerbach, F. Izrailev, and V. Zelevinsky, "Distribution of resonance widths and dynamics of continuum coupling," *Physical review letters*, vol. 106, no. 4, p. 042501, 2011.

[122] K. Hepp and E. H. Lieb, "On the superradiant phase transition for molecules in a quantized radiation field: The dicke maser model," *Annals of Physics*, vol. 76, no. 2, pp. 360–404, 1973.

[123] D. Meiser, J. Ye, D. Carlson, and M. Holland, "Prospects for a millihertz-linewidth laser," *Physical review letters*, vol. 102, no. 16, p. 163601, 2009.

[124] D. Meiser and M. Holland, "Steady-state superradiance with alkaline-earth-metal atoms," *Physical Review A*, vol. 81, no. 3, p. 033847, 2010.

[125] H. Xia, A. A. Svidzinsky, L. Yuan, C. Lu, S. Suckewer, and M. O. Scully, "Observing superradiant decay of excited-state helium atoms inside helium plasma," *Physical review letters*, vol. 109, no. 9, p. 093604, 2012.

[126] Y.-N. Chen, D.-S. Chuu, and T. Brandes, "Current detection of superradiance and induced entanglement of double quantum dot excitons," *Physical review letters*, vol. 90, no. 16, p. 166802, 2003.

[127] S.-H. Lim, T. G. Bjorklund, F. C. Spano, and C. J. Bardeen, "Exciton delocalization and superradiance in tetracene thin films and nanoaggregates," *Physical review letters*, vol. 92, no. 10, p. 107402, 2004.

[128] M. Ichimiya, M. Ashida, H. Yasuda, H. Ishihara, and T. Itoh, "Observation of superradiance by nonlocal wave coupling of light and excitons in cucl thin films," *Physical review letters*, vol. 103, no. 25, p. 257401, 2009.

[129] L. Giannessi, M. Artioli, M. Bellaveglia, F. Briquez, E. Chiadroni, A. Cianchi, M. Couprie, G. Dattoli, E. Di Palma, G. Di Pirro *et al.*, "High-order-harmonic generation and superradiance in a seeded free-electron laser," *Physical review letters*, vol. 108, no. 16, p. 164801, 2012.

[130] T. Watanabe, X. Wang, J. Murphy, J. Rose, Y. Shen, T. Tsang, L. Giannessi, P. Musumeci, and S. Reiche, "Experimental characterization of superradiance in a single-pass high-gain laser-seeded free-electron laser amplifier," *Physical review letters*, vol. 98, no. 3, p. 034802, 2007.

[131] S. Inouye, A. Chikkatur, D. Stamper-Kurn, J. Stenger, D. Pritchard, and W. Ketterle, "Superradiant rayleigh scattering from a bose-einstein condensate," *Science*, vol. 285, no. 5427, pp. 571–574, 1999.

[132] D. Schneble, Y. Torii, M. Boyd, E. W. Streed, D. E. Pritchard, and W. Ketterle, "The onset of matter-wave amplification in a superradiant bose-einstein condensate," *Science*, vol. 300, no. 5618, pp. 475–478, 2003.

[133] S. Inouye, T. Pfau, S. Gupta, A. Chikkatur, A. Görlitz, D. Pritchard, and W. Ketterle, "Phase-coherent amplification of atomic matter waves," *Nature*, vol. 402, no. 6762, pp. 641–644, 1999.

[134] K. Baumann, C. Guerlin, F. Brennecke, and T. Esslinger, "Dicke quantum phase transition with a superfluid gas in an optical cavity," *Nature*, vol. 464, no. 7293, pp. 1301–1306, 2010.

[135] M. Kozuma, Y. Suzuki, Y. Torii, T. Sugiura, T. Kuga, E. Hagley, and L. Deng, "Phase-coherent amplification of matter waves," *Science*, vol. 286, no. 5448, pp. 2309–2312, 1999.

[136] O. Viehmann, J. von Delft, and F. Marquardt, "Superradiant phase transitions and the standard description of circuit qed," *Physical review letters*, vol. 107, no. 11, p. 113602, 2011.

[137] Y. S. Greenberg, C. Merrigan, A. Tayebi, and V. Zelevinsky, "Quantum signal transmission through a single-qubit chain," *The European Physical Journal B*, vol. 86, no. 9, pp. 1–10, 2013.

[138] M. Scheibner, T. Schmidt, L. Worschech, A. Forchel, G. Bacher, T. Passow, and D. Hommel, "Superradiance of quantum dots," *Nature Physics*, vol. 3, no. 2, pp. 106–110, 2007.

[139] G. Khitrova and H. M. Gibbs, "Quantum dots: Collective radiance," *Nature Physics*, vol. 3, no. 2, pp. 84–86, 2007.

[140] N. Lambert, C. Emary, and T. Brandes, "Entanglement and the phase transition in single-mode superradiance," *Physical review letters*, vol. 92, no. 7, p. 073602, 2004.

[141] D. Nagy, G. Kónya, G. Szirmai, and P. Domokos, "Dicke-model phase transition in the quantum motion of a bose-einstein condensate in an optical cavity," *Physical review letters*, vol. 104, no. 13, p. 130401, 2010.

[142] V. Bastidas, C. Emary, B. Regler, and T. Brandes, "Nonequilibrium quantum phase transitions in the dicke model," *Physical review letters*, vol. 108, no. 4, p. 043003, 2012.

[143] A. Baksic, P. Nataf, and C. Ciuti, "Superradiant phase transitions with three-level systems," *Physical Review A*, vol. 87, no. 2, p. 023813, 2013.

[144] V. Sokolov and V. Zelevinsky, "On a statistical theory of overlapping resonances," *Physics Letters B*, vol. 202, no. 1, pp. 10–14, 1988.

[145] ——, "Collective dynamics of unstable quantum states," *Annals of Physics*, vol. 216, no. 2, pp. 323–350, 1992.

[146] N. Auerbach and V. Zelevinsky, "Super-radiant dynamics, doorways and resonances in nuclei and other open mesoscopic systems," *Reports on Progress in Physics*, vol. 74, no. 10, p. 106301, 2011.

[147] T. Guhr, A. Müller-Groeling, and H. A. Weidenmüller, "Random-matrix theories in quantum physics: common concepts," *Physics Reports*, vol. 299, no. 4, pp. 189–425, 1998.

[148] M. Asada, "Theory of superradiance from photon-assisted tunneling electrons and its application to terahertz device," *Journal of applied physics*, vol. 94, no. 1, pp. 677–685, 2003.

[149] T. Teperik and A. Degiron, "Superradiant optical emitters coupled to an array of nanosize metallic antennas," *Physical review letters*, vol. 108, no. 14, p. 147401, 2012.

[150] J. G. Bohnet, Z. Chen, J. M. Weiner, D. Meiser, M. J. Holland, and J. K. Thompson, "A steady-state superradiant laser with less than one intracavity photon," *Nature*, vol. 484, no. 7392, pp. 78–81, 2012.

[151] O. Kyriienko, A. Kavokin, and I. Shelykh, "Superradiant terahertz emission by dipolaritons," *Physical review letters*, vol. 111, no. 17, p. 176401, 2013.

[152] M. C. Rechtsman, J. M. Zeuner, Y. Plotnik, Y. Lumer, D. Podolsky, F. Dreisow, S. Nolte, M. Segev, and A. Szameit, "Photonic floquet topological insulators," *Nature*, vol. 496, no. 7444, pp. 196–200, 2013.

[153] L. Levi, Y. Krivolapov, S. Fishman, and M. Segev, "Hyper-transport of light and stochastic acceleration by evolving disorder," *Nature Physics*, vol. 8, no. 12, pp. 912–917, 2012.

[154] T. Pertsch, P. Dannberg, W. Elflein, A. Bräuer, and F. Lederer, "Optical bloch oscillations in temperature tuned waveguide arrays," *Physical Review Letters*, vol. 83, no. 23, p. 4752, 1999.

[155] A. Fratalocchi and G. Assanto, "All-optical landau-zener tunneling in waveguide arrays," *Optics express*, vol. 14, no. 5, pp. 2021–2026, 2006.

[156] R. Morandotti, U. Peschel, J. Aitchison, H. Eisenberg, and Y. Silberberg, "Experimental observation of linear and nonlinear optical bloch oscillations," *Physical Review Letters*, vol. 83, no. 23, p. 4756, 1999.

[157] H. Trompeter, T. Pertsch, F. Lederer, D. Michaelis, U. Streppel, A. Bräuer, and U. Peschel, "Visual observation of zener tunneling," *Physical review letters*, vol. 96, no. 2, p. 023901, 2006.

[158] C. Porter and R. Thomas, "Fluctuations of nuclear reaction widths," *Physical Review*, vol. 104, no. 2, p. 483, 1956.

[159] G. Celardo, F. Izrailev, V. Zelevinsky, and G. Berman, "Open system of interacting fermions: Statistical properties of cross sections and fluctuations," *Physical Review E*, vol. 76, no. 3, p. 031119, 2007.

[160] G. Celardo and L. Kaplan, "Superradiance transition in one-dimensional nanostructures: An effective non-hermitian hamiltonian formalism," *Physical Review B*, vol. 79, no. 15, p. 155108, 2009.

[161] C. Conti, A. Di Falco, and G. Assanto, "Optical parametric oscillations in isotropic photonic crystals," *Optics express*, vol. 12, no. 5, pp. 823–828, 2004.

[162] A. Di Falco, C. Conti, and G. Assanto, "Impedance matching in photonic crystal microcavities for second-harmonic generation," *Optics letters*, vol. 31, no. 2, pp. 250–252, 2006.

[163] K. S. Yee *et al.*, "Numerical solution of initial boundary value problems involving maxwells equations in isotropic media," *IEEE Trans. Antennas Propag*, vol. 14, no. 3, pp. 302–307, 1966.

[164] A. Taflove, "Application of the finite-difference time-domain method to sinusoidal steady-state electromagnetic-penetration problems," *Electromagnetic Compatibility, IEEE Transactions on*, no. 3, pp. 191–202, 1980.

[165] A. Taflov, "A perspective on the 40-year history of fdtd computational electrodynamics," *Applied Computational Electromagnetics Society Journal*, vol. 22, no. 1, p. 1, 2007.

[166] A. Fratalocchi, C. Conti, and G. Ruocco, "Three-dimensional ab initio investigation of light-matter interaction in mie lasers," *Physical Review A*, vol. 78, no. 1, p. 013806, 2008.

[167] A. Fratalocchi, C. Conti, and G. Ruocc, "Mode competitions and dynamical frequency pulling in mie nanolasers: 3d ab-initio maxwell-bloch computations," *Optics express*, vol. 16, no. 12, pp. 8342–8349, 2008.

[168] K. Willis, J. Ayubi-Moak, S. Hagness, and I. Knezevic, "Global modeling of carrier-field dynamics in semiconductors using emc–fdtd," *Journal of computational electronics*, vol. 8, no. 2, pp. 153–171, 2009.

[169] C. Guiffaut and K. Mahdjoubi, "A parallel fdtd algorithm using the mpi library," *Antennas and Propagation Magazine, IEEE*, vol. 43, no. 2, pp. 94–103, 2001.

[170] A. Taflove, S. C. Hagness *et al.*, *Computational electrodynamics: the finite-difference time-domain method*. Artech House, 1995.

[171] D. Wales, *Energy landscapes: Applications to clusters, biomolecules and glasses*. Cambridge University Press, 2003.

[172] H. Poincaré, "Sur le probleme des trois corps et les équations de la dynamique," *Acta mathematica*, vol. 13, no. 1, pp. A3–A270, 1890.

[173] E. N. Lorenz, "Section of planetary sciences: The predictability of hydrodynamic flow*,," *Transactions of the New York Academy of Sciences*, vol. 25, no. 4 Series II, pp. 409–432, 1963.

[174] M. Sciamanna and K. Shore, "Physics and applications of laser diode chaos," *Nature Photonics*, vol. 9, no. 3, pp. 151–162, 2015.

[175] L. Jackson, A. Lindgren, Y. Kim *et al.*, "A chaotic attractor from chuas circuit," *IEEE Transactions on Circuits and Systems*, vol. 31, p. 1055, 1984.

[176] S. Alben and M. J. Shelley, "Flapping states of a flag in an inviscid fluid: Bistability and the transition to chaos," *Phys. Rev. Lett.*, vol. 100, p. 074301, Feb 2008.

[177] V. Petrov, V. Gaspar, J. Masere, and K. Showalter, "Controlling chaos in the belousovzhabotinsky reaction," *Nature*, vol. 361, no. 6409, pp. 240–243, 1993.

[178] S. J. Schiff, K. Jerger, D. H. Duong, T. Chang, M. L. Spano, W. L. Ditto *et al.*, "Controlling chaos in the brain," *Nature*, vol. 370, no. 6491, pp. 615–620, 1994.

[179] L. Li, H. Peng, J. Kurths, Y. Yang, and H. J. Schellnhuber, "Chaos–order transition in foraging behavior of ants," *Proceedings of the National Academy of Sciences*, vol. 111, no. 23, pp. 8392–8397, 2014.

[180] O. Bohigas, M.-J. Giannoni, and C. Schmit, "Characterization of chaotic quantum spectra and universality of level fluctuation laws," *Physical Review Letters*, vol. 52, no. 1, p. 1, 1984.

[181] F. Saif, "Classical and quantum chaos in atom optics," *Physics Reports*, vol. 419, no. 6, pp. 207–258, 2005.

[182] M. Courtney, N. Spellmeyer, H. Jiao, and D. Kleppner, "Classical, semiclassical, and quantum dynamics in the lithium stark system," *Physical Review A*, vol. 51, no. 5, p. 3604, 1995.

[183] N. Friedman, A. Kaplan, D. Carasso, and N. Davidson, "Observation of chaotic and regular dynamics in atom-optics billiards," *Physical review letters*, vol. 86, no. 8, p. 1518, 2001.

[184] S. Chaudhury, A. Smith, B. Anderson, S. Ghose, and P. Jessen, "Quantum signatures of chaos in a kicked top," *Nature*, vol. 461, no. 7265, pp. 768–771, 2009.

[185] A. Frisch, M. Mark, K. Aikawa, F. Ferlaino, J. L. Bohn, C. Makrides, A. Petrov, and S. Kotochigova, "Quantum chaos in ultracold collisions of gas-phase erbium atoms," *Nature*, vol. 507, no. 7493, pp. 475–479, 2014.

[186] F. Stephens, M. Deleplanque, I. Lee, A. Macchiavelli, D. Ward, P. Fallon, M. Cromaz, R. Clark, M. Descovich, R. Diamond *et al.*, "Order-to-chaos transition in rotational nuclei," *Physical review letters*, vol. 94, no. 4, p. 042501, 2005.

[187] T. Gensty, K. Becker, I. Fischer, W. Elsäßer, C. Degen, P. Debernardi, and G. P. Bava, "Wave chaos in real-world vertical-cavity surface-emitting lasers," *Physical review letters*, vol. 94, no. 23, p. 233901, 2005.

APPENDICES

A Numerical Methods

A.1 FDTD Methond

FDTD is an numerical method to solve the maxwell equations for the electromagnetic waves. The original idea was developed by Kane Yee in 1962 [163] and the name was coined by Allen Taflove in 1980 [164]. After five decades of development, FDTD becomes one of the most used numerical methods in computational electromagnetics, covering a broad wavelength range from visible light, microwaves to near-DC signals [165]. Further more, the Maxwell solver based on FDTD can be coupled with other models such as Bloch equation and Boltzmann transportequation to model more complicated physics [166, 167, 168]. Besides, the flexibility of the method benefits its use in parallel computing [169].

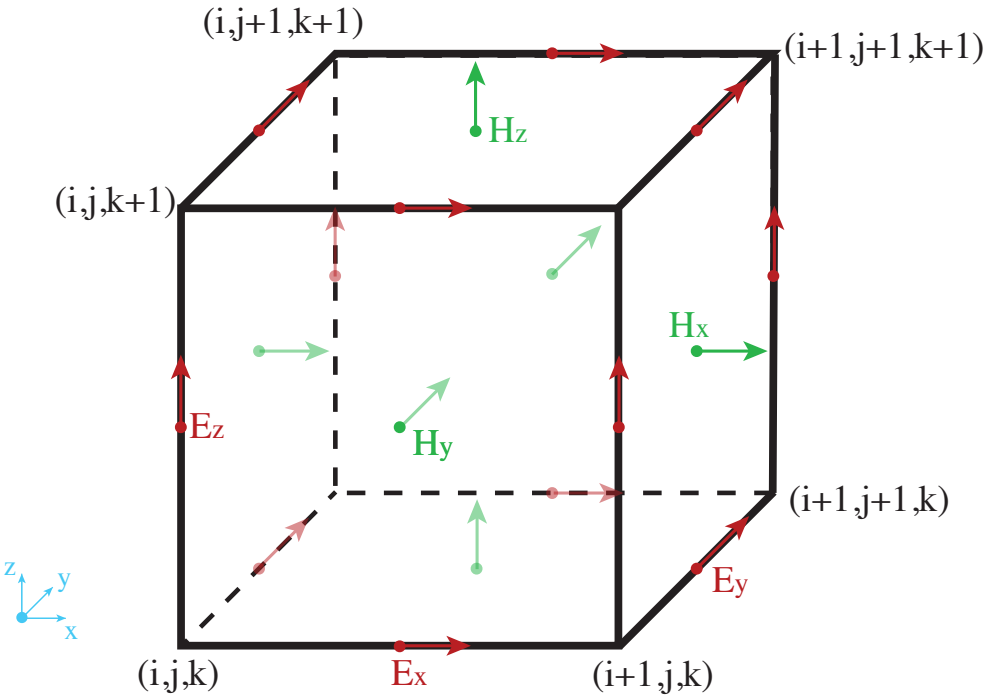

Figure A.1: Yee lattice for FDTD

The dynamics of electromagnetic waves follows Maxwell equations:

$$\nabla \times \mathbf{E} = -\mu \frac{\partial \mathbf{H}}{\partial t} \tag{A.1}$$

$$\nabla \times \mathbf{H} = \varepsilon \frac{\partial \mathbf{E}}{\partial t} + \sigma \mathbf{E} \tag{A.2}$$

with $\mathbf{E}$ and $\mathbf{H}$ the electric and magnetic field, ε and μ the permittivity and permeability and σ the conductivity. The temporal change of electric field ($\frac{\partial \mathbf{E}}{\partial t}$) depends on the change of magnetic field in space ($\nabla \times \mathbf{H}$) and vice versa. For any point in space, the value of current electric filed depends on both the previous value in time and the local distribution of magnetic field in space.

Using finite difference approximation, we can discretize Maxwell equation's by central-difference in both space and time. Based on Yee lattice (Fig. A.1, the electric filed

and magnetic field are separated in space. To completely decouple the electric and magnetic fields, a leapfrog scheme is proposed. The updates of the electric field $\mathbf{E}$ staggered half time step with magnetic field $\mathbf{H}$, so the value is always calculated in the midway of two successive magnetic field, achieving the separation also in time. Then A two-step algorithm can be applied to calculate the electric field and magnetic field separately. At the temporal step $t = n$, the magnetic field $\mathbf{H}^n$ can be calculated from the previous magnetic fields $\mathbf{H}^{n-1}$ and the electric field around forming a close loop. For example, $H^n_{y;(i+1/2,j,k+1/2)}$ can be derived from $H^{n-1}_{y;(i+1/2,j,k+1/2)}$ and $E^{n-1/2}_{x;(i+1/2,j,k)}$, $E^{n-1/2}_{x;(+i1/2,j,k+1)}$, $E^{n-1/2}_{z;(i+1,j,k+1/2)}$, $E^{n-1/2}_{z;(i,j,k+1/2)}$ using Eq. A.1. For the second step, the electric field $\mathbf{E}^{n+1/2}$ at $t = n + 1/2$ can be calculated in a similar way using Eq. A.2. Therefore, the electromagnetic fields in both space and time can be calculated by iteration of the two-step algorithm. When the time step is small enough (compared to the period of the electromagnetic wave circle), a good approximation of the continuous evolution of the electromagnetics.

There are a variety of advantages of FDTD compared to other methods for the computational electromagnetics. Compared to the finite element in frequency domain, FDTD directly illustrates the evolution of the electromagnetic waves in time, providing a clear picture to explore the physics hidden. For the simulations with broadband source, the FDTD method in time domain can provide the response in a single run, while the finite element methods need scan over the frequencies one by one. Using electric and magnetic fields directly, there is no need for the post process of conversion is required. Meanwhile, the huge computational resources limits the use of the FDTD method for the sophisticated models.

The equations and more details of the FDTD can be found in the text book by Taflove and Hagness [170]. All the FDTD simulations in the thesis is based on our home-made FDTD code called NANOCPP, running on the supercomputer SHAHEEN I in KAUST.

A.2 Prony method

Prony method, or Prony analysis, is an numerical method to decompose a time-varying signal $s(t)$ to damped complex sinusoids(or exponentials) [118]. In this desertion, it is used to extract the lifetime (or the resonance width) of the modes supported by a optical cavity from the signal in time domain.

Suppose the signal $s(t)$ can be decomposed into a series of decamped exponential functions:

$$s(t) = \sum_{i=1}^{N} \frac{1}{2} A_i e^{\pm j\phi_i} e^{\lambda_i t} \tag{A.3}$$

with $\lambda_i = \sigma_i \pm j\omega_i$ the complexed eigenvalues and ϕ_i the phases and $A_i$the amplitudes. Here σ_i corresponds to the damping factor and ω_i is the angular frequency. Sampling $s(t)$ at the timer interval Δ_t, s(t) can be discretized to

$$S_n = \hat{s}(\Delta_t n) = \sum_{m=1}^{M} B_m e^{\lambda_m \Delta_t n} \tag{A.4}$$

with n an integer number. A difference equation can be derived (more details in ref [118]):

$$\hat{s}(\Delta_t n) = -\sum_{m=1}^{M} \hat{s}[\Delta_t (n-m)] P_m \tag{A.5}$$

where the coefficient P_m obeys the following equation:

$$\sum_{m=1}^{M+1} P_m x^{m-1} = \prod_{m=1}^{M} \left(x - e^{\lambda_m}\right) \tag{A.6}$$

Using Eq. A.5, we can build a matrix equation:

$$\begin{bmatrix} S_M \\ \vdots \\ S_{N-1} \end{bmatrix} = - \begin{bmatrix} S_{M-1} & \dots & S_0 \\ \vdots & \ddots & \vdots \\ S_{N-2} & \dots & S_{N-M-1} \end{bmatrix} \begin{bmatrix} P_1 \\ \vdots \\ P_M \end{bmatrix} = \mathcal{S} \begin{bmatrix} P_1 \\ \vdots \\ P_M \end{bmatrix} \tag{A.7}$$

Then the coefficient P_m can be solved when the inverse matrix of $\mathcal{S}$ exists:

$$\begin{bmatrix} P_1 \\ \vdots \\ P_M \end{bmatrix} = \mathcal{S}^{-1} \begin{bmatrix} S_M \\ \vdots \\ S_{N-1} \end{bmatrix} \tag{A.8}$$

Applying the solution to Eq. A.6, the eigenvalue λ_m is the m-th root of the following equation:

$$x^M + \sum_{m=1}^{M} P_m x^{m-1} = 0 \tag{A.9}$$

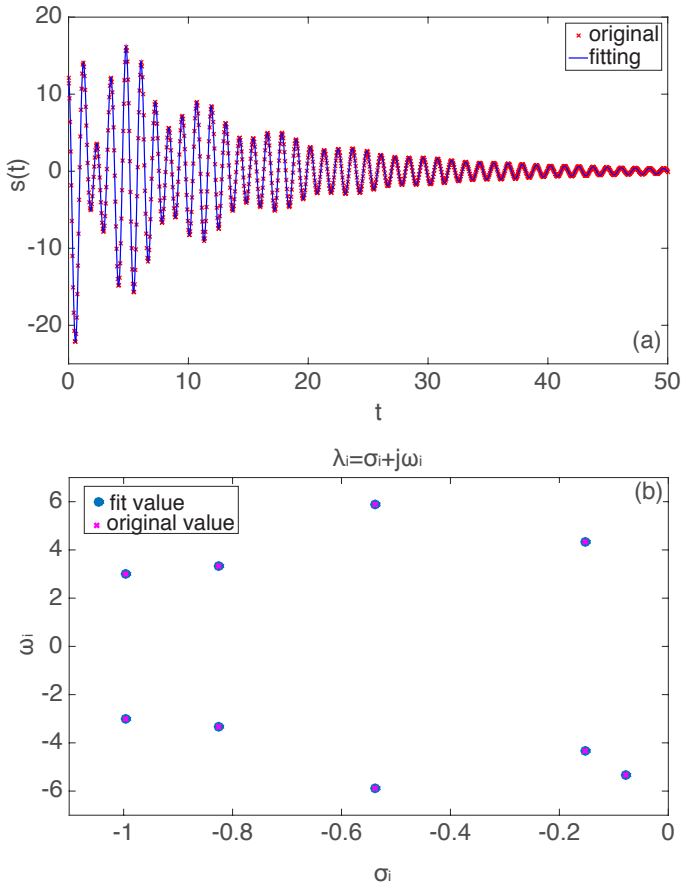

Figure A.2: An example of eigenmodes extraction based on Prony method with $M = 8$. (a) The comparison between the original and fitted signal. (b) Eigenvalues in the complex plane $\lambda_i = \sigma_i + j\omega_i$ for the original ones (red cross) and extracted ones(blue circle). A perfect fit is achieved.

Figure A.2 demonstrates an example of extracting the egienvalue λ_i from a time-varying signal $s(t)$. From Fig. A.2a, an excellent match is observed between the original and fitted $s(t)$. The eigenvalues can be perfectly extracted from the given signal, as shown in Fig. A.2b.

A.3 Lifetime extraction from spectrum based on Multi-scale analysis

Prony method explained in the previous section provides an way to extract the life-time of the eigenmodes from single in time domain. Here, a method in frequency domain is introduce for the life time extraction based on multi-scale analysis. The power density spectrum from an optical cavity can be well fitted from the multi-scale procedure, even in the case of strong eigenmodes overlapping [39].
The multiscale analysis consist of two steps, wavelet transforms and complex land-scapes topology. Applying the wavelet transformation, power density spectrum $P(\lambda)$ (shown in Fig. A.3a) will be converted to:

$$\mathcal{W}P = \int_{-\infty}^{\infty} \frac{\psi}{\sqrt{\chi}}\left(\frac{\lambda-\zeta}{\chi}\right)P(\lambda)\mathrm{d}\lambda \tag{A.10}$$

with χ the scaling parameter, ζ the translation parameter, and ψ the mother wavelet. Mother wavelet ψ is a compact function in $L^2(\mathbf{R})$ with zero mean and statisfies:

$$\int_{-\infty}^{\infty} \frac{\left|\tilde{\psi}(f)\right|^2}{|f|}\mathrm{d}f < \infty \tag{A.11}$$

with $\tilde{\psi}(f)$ the Fourier transform of ψ. The symmetric wavelet $\psi = (2-4t^2)e^{-t^2}$ is selected to fit the Lorentzian-liked spectrum [39]. Figure A.3b shows a wavelet transform from a typical experimental spectrum, visualization the hidden resonance

structures in the spectrum. The resonances join together along the treelike structure as the increment of the the scaling parameter χ. The surface topology provides all the informations related to the resonances, as illustrated in Fig. A.3b. The connection between the dense areas is the hallmark of clusters while the isolated resonances are featured by the mssing of the tree structure.

For the second step, an uphill landscape analysis [171] is applied to to deal with the isolation and clusters in $\mathcal{WP}$. Following the minimum curvature in surface, a series of runners are applied along the χ direction (solid red lines in Fig. A.3c). An adjacent matrix $\mathcal{A}$ can be define to illustrate the connections of different runners along the tree, with $A_{ij} = 1$ that runner i and j share the path and $A_{ij} = 0$ not. All the information of topological structures and the composition of the clusters is self-contained in the adjacent matrix $\mathcal{A}$. Combined with the wavelet transform $\mathcal{WP}$, both the position and the line-width of the eigenmodes in the optical cavity can be derived. In the case of isolated resonance ($\mathcal{A}_{ij} = 0$ when $i \neq j$), we can follow the path of the related runner to the first maximum point (χ, ζ) at the surface formed by wavelet transform. At that point, the resonance position λ is simply equal to χ while the Full Width at Half Maximum (FWHM) $\delta\lambda = \chi\sqrt{\log 2/2}$, i.e. $\sqrt{2\log 2}$ times the Gaussian part of the wavelet. In the case of clusters ($\mathcal{A}_{ij} = 1$ for some i, j), a nonlinear simplex optimization search in the subspace spanned by the corresponding runners is applied to get optimal paris and λ_0 and $\delta\lambda$. Finally, a global nonlinear least-square optimization is applied in the whole spectrum to further increase the accuracy. Figure A.3d compares the reconstructed ower Density Spectrum (Power Density Spectrum (PDS)) with the original experimental measurement. Despite the strong interactions between the resonances, an excellent matching is achieved through the analysis.

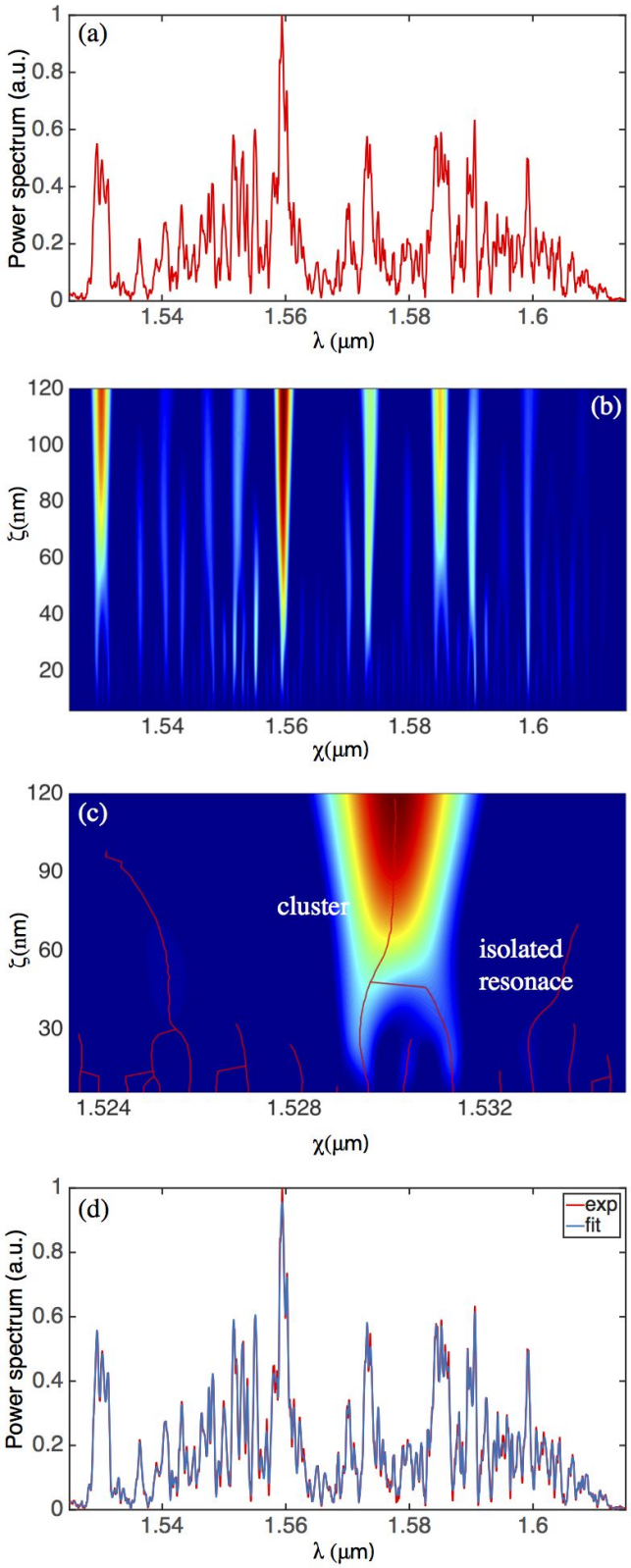

Figure A.3: An example of eigenmodes extraction based on mulitscale analysis. (a) A typical PDS $P(\lambda)$ from an optical cavity. (b) Continuous wavelet transform of $P(\lambda)$. (c) Uphil Landspace analysis, showing the clusters and isolated resonance formeb by the runner (red solid line). (d) Comparison between reconstructed spectrum and experimental measurement.

B Classical Quantum Chaos

B.1 classical chaos and quantum chaos

Chaos is a complicated dynamics with exceptional sensitivity to the initial conditions. Two systems with infinitesimal difference of the initial condition will diverge exponentially, as shown in Fig. B.1.

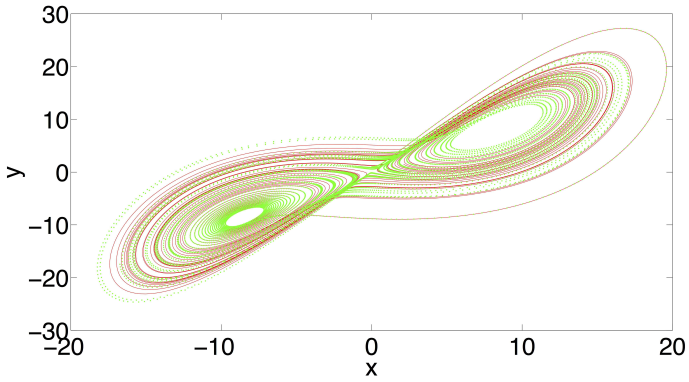

Figure B.1: A demonstration of the sensitive of a chaotic system, A system with initial point $[x_0, y_0]$ (red line) and $[x_0 + \delta, y_0]$ deviates dramatically with $\delta = 10^{-4}$;

The history of chaos can be dated back to 19th century, when Poincaré studied the orbits of three-body system [172]. Chaos is a ubiquitous phenomenon that exists in many natural systems. Probably, the most famous one among them is the butterfly effect discovered by Edward Lorenz in weather forecast in 1962: something as small as the flutter of a butterfly's wing can ultimately cause a typhoon halfway around the world [173]. Since then chaos has extensively studied in a variety of systems, including laser diodes [174], electronic circuits [175], fluids [176], chemical reactions

[177], brains [178] and beyond [179].

Quantum chaos is the counterpart of the classical chaos in the quantum regime. The Hallmark of quantum chaos is the fluctuations of the energy levels in the Hamiltonian [180]. These fluctuations were related the chaotic dynamics at the classical limit in phase space which sharesthe similar properties of chaotic systems in classical regime [181, 182]. The spectral fluctuations of a quantum system (the classical limit is chaotic) show a intense level-repulsion predicated by RMT [147]. Quantum chaos has been reported in many atomic systems, ranging from cold atoms to rotation nuclei [183, 184, 185, 186].

The isomorphisms between Schrödinger and Maxwell equations allow us to investigate different quantum phenomena that manifest in dielectric optical micro-resonators that forms mimic classically chaotic billiards and provide us a viable platform to study the transition of chaos in quantum regime [39, 187]. Light-matter interactions in a chaotic resonator are of particular interest.

C Papers Submitted and Under Preparation

• R. Bruck*, C. Liu*, O. Muskens, A. Di Falco and A. Fratalocchi, "Ultrafast order-to-chaos transition in quantum photonic chips", *Under review by Laser & Photonics Review*, 03.2016.

•H. Wang, F. Li, D. Kufer, W. Yu, E. Alarousu, C. Ma, Y. Li, Z. Liu, C. Liu, N. Wei, Y. Chen, F. Wang, L. Chen, O. Mohammed, A. Fratalocchi, G. Konstantato, T. Wu, , "Solution-processed ambipolar hybrid perovskite/carbon nanotube phototransistors with ultrahigh mobility and responsivity", *Under review by Advanced Materials*, 05. 2016.

• C. Liu*, J. Huang*, Y. Han, A. Fratalocchi, "High-performance large-scale solar steam generation with nanolayers of reusable biomimetic nanoparticles", *Under review by Nature Energy.*